UNIVERSITÀ
DEGLI STUDI
DI PADOVA

TESI DI DOTTORATO DI RICERCA IN SCIENZA E INGEGNERIA DEI MATERIALI

Università degli Studi di Padova

Dipartimento di Scienze Chimiche

SCUOLA DI DOTTORATO DI RICERCA IN SCIENZA E INGEGNERIA DEI MATERIALI
INDIRIZZO COMUNE
CICLO XXVIII

Plasmonic Au/Ag ordered nanoarrays for biosensing applications

Direttore della Scuola: Ch.mo Prof. Gaetano GRANOZZI
Supervisore: Ch.mo Prof. Giovanni MATTEI

Dottoranda: Valentina RUSSO

To Verena, my best friend.

E un adolescente disse: Parlaci dell'Amicizia. E lui rispose dicendo: Il vostro amico è il vostro bisogno saziato. E condividete i piaceri sorridendo nella dolcezza dell'amicizia. Poiché nella rugiada delle piccole cose il cuore ritrova il suo mattino e si ristora.

Kahlil Gibran (1923)

Abstract

The aim of the present work is the study and the nanofabrication of innovative plasmonic nanostructured materials to develop label-free optical biosensors. The motivation arises from the need to identify specific biological molecules at very low concentrations (below the picoMolar level) and with high specificity. This goal is of paramount importance for instance in diagnostics and prognostics through the early-stage detection of markers in biological fluids indicating possible altered biological processes. At the same time a fast and simple detection scheme is required, without the use of labelling strategies. The innovative plasmonic properties of noble metals (Au,Ag) nanomaterials have been investigated for biosensing applications since 1983. These plasmonic properties arise from the interaction of an electromagnetic wave with nanostructured metals, i.e., metallic structures with size in the order of or smaller than the incident field wavelength in the Vis-NIR range: their most celebrated effect is the onset of the surface plasmon resonances (SPR). Prims-coupled biosensing devices based on SPR of gold thin film (thickness lower than 100 nm) were commercialized since 1990. These systems allow to monitor biomolecular interactions and to quantify a wide range of chemical and biological species down to nanomolar concentrations. The scientific community is strongly active in the optimization of the performances of the SPR sensors in terms of sensitivity, specificity and limit of detection. The present work is based on the application of the SPR properties of ordered Au/Ag nanoarrays for biological detection, in order to investigate and optimize their sensing performances. The detection mechanism is based on the variation of the SPR for refractive index changes, which are due to analyte molecules immobilized on the nanoarray's surface. We have studied three classes of nanoarrays based on noble metals: (i) semi-nanoshell array, (ii) nanoprism array and (iii) nanohole array. Gold and silver are the best plasmonic metals for their intrinsic properties of interaction with an electromagnetic field in the Vis-NIR range. The nanoarrays were synthesized by Nanosphere Lithography, and they are based on hexagonal arrays of nanounits such as nanoprims, semi-nanoshells and nanoholes. The synthesis technique allows to finely control the morphology and the dimensions of the nanounits and, as a consequence, their optical properties. The samples based on nanoprims and semi-nanoshells support high electromagnetic field localization on their surface, which is due to the excitation of localized SPR; for this reason these systems could be very interesting sensors to detect thin analyte molecules layers with low molecular weight. The samples based on nanoholes arrays are characterized by the Extraordinary Optical Transmission (EOT), which is controlled by the excitation of extended SPR. The longer decay length of this kind of plasmons makes EOT particularly useful to detect also bigger molecules such as viruses or bacteria. All the samples were functionalized with the same protocol based on the biotin-streptavidin couple as the receptor-ligand scheme. The sensing performances were investigated by exposing the functionalized samples to different analyte concentrations. Moreover, the local and bulk sensitivity to refractive index changes was measured. The experimental results were also compared with numerical simulations and we found a

good level of agreement between the experimental and simulated data. Silver nanoprisms arrays were also studied as Surface Enhancement Raman Spectroscopy (SERS) substrates. They were oxidized with different treatments to investigate the silver oxide effect on the SERS performances. All the obtained results in the present work indicate performances of the three investigated nanostructures, which are at the state-of-the-art with respect to literature data.

Estratto

Il tema centrale del presente lavoro di dottorato è lo studio e la nanofabbricazione di materiali plasmonici inovativi nanostrutturati per lo sviluppo di biosensori ottici label-free. La motivazione risiede nell'esigenza di identificare determinate specie biologiche in concentrazioni sempre minori (inferiore al picomolare) e con una tecnologia di rilevazione altamente sensibile e specifica, al fine di rilevare la presenza di processi biologici normali o alterati. Nello stesso tempo si richiede una rilevazione veloce, semplice e che non necessiti di un marcatore ottico. Le innovative proprietà plasmoniche che caratterizzano i nanomateriali costituiti da metalli nobili (Au,Ag) sono state investigate per applicazioni biosensoristiche fin dal 1983. Queste proprietà plasmoniche derivano dall'interazione di una radiazione elettromagnetica con i metalli nanostrutturati; i.e. strutture metalliche con dimensioni dell'ordine o minore della lunghezza d'onda della radiazione incidente nel range del Vis-NIR, e si basano sulla risonanza plasmonica superficiale (SPR). Dispositivi biosensoristici basati sulla SPR di film sottili di oro (spessore inferiore a 100 nm) accoppiati con un prisma, sono in commercio dal 1990. Questi sistemi permettono di monitorare interazioni biomolecolari e di quantificare una vasta gamma di specie chimiche e biologiche, fino a concentrazioni dell'ordine del nanomolare. La comunità scientifica è fortemente attiva nel cercare di ottimizzare le prestazioni dei sensori SPR in termini di sensibilità, specificità e limite di rilevazione. Il presente lavoro si basa sull'applicazione delle proprietà SPR di nanoarray ordinati a base di Au e Ag per la rilevazione di molecole biologiche, al fine di investigarne ed ottimizzarne le prestazioni. Il meccanismo di sensing si basa sulla variazione della SPR per variazioni di indice di rifrazione, che sono dovuti all'immobilizzazione di molecole analita sulla superficie dei nanoarray. Sono state studiate tre classi di nanoarray costituiti da metalli nobili: (i) semi-nanoshell array, (ii) nanoprism array e (iii) nanohole array. Oro ed Argento sono i migliori candidati per applicazioni nel campo della plasmonica per le loro proprietà intrinseche di interazione con la radiazione elettromagnetica, in particolare nelle frequenze del visibile e del vicino infrarosso. I nanoarray sono stati sintetizzati mediante la tecnica di Litografia a Nanosfere, e sono costituiti da array esagonali di nanounità, cresciute in forma di nanoprismi, semi-nanoshells e nanoholes. La tecnica di sintesi utilizzata permette di controllare finemente la morfologia e le dimensioni delle nanounità e, di conseguenza, le rispettive proprietà ottiche. I sistemi costituiti da nanoprismi o semi-nanoshells sono caratterizzati da un'elevata amplificazione di campo elettromagnetico sulla loro superficie, la quale è dovuta all'eccitazione della SPR; per questo motivo questi sistemi potrebbero essere molto interessanti per la rilevazione di spessori molto piccoli di molecole analita con un basso peso molecolare. I campioni costituiti da nanoholes array sono caratterizzati dalla trasmissione ottica straordinaria (EOT), la quale è controllata dall'eccitazione di SPR propaganti. La maggiore lunghezza di decadimento di questo tipo di plasmoni rende la EOT particolarmente utile anche per la rilevazione di molecole più grandi come virus o batteri. Tutti i campioni

sono stati funzionalizzati con lo stesso protocollo di funzionalizzazione basato su una coppia modello di molecole biologiche recettore-analita (biotina-streptavidina). Le proprietà di sensing sono state investigate esponendo i campioni funzionalizzati con uno specifico recettore, a differenti concentrazioni della molecola analita. Inoltre è stata misurata la sensibilità locale e bulk in risposta alle variazioni di indice di rifrazione. I risultati sperimentali sono stati anche confrontati con dei modelli teorici ottenendo un buon accordo tra il dato sperimentale e quello simulato. I nanoprismi di argento sono stati anche studiati come possibili substrati per la spettroscopia SERS. I campioni sono stati ossidati con diversi trattamenti al fine di analizzare l'effetto dell'ossido sul segnale SERS. I risultati ottenuti nel prente lavoro hanno mostrato come le tre tipologie di nanostrutture studiate mostrino performance che sono allo stato dell'arte rispetto ai valori di letteratura.

Contents

List of Acronyms

AFM	Atomic Force Microscope
SPR	Surface Plasmon Resonance
MW	Molecular Weight
PEG	Polyethylene Glycol
SA	streptavidin
11-MUA	11-Mercaptoundecanoic Acid
EDC	1-Ethyl-3-[3-Dimethylaminopropyl]Carbodiimide hydrochloride
MES	2-(N-Morpholino)EthaneSulfonic acid sodium salt
PBS	Phosphate Buffered Saline
SAM	Self Assembled Monolayer
1-OCT	1-Octanethiol
SNSA	Semi-NanoShell Array
NHA	NanoHoles Array
NPA	NanoPrisms Array
PS	Polystyrene
LSPR	Localized Surface Plasmon Resonance
FWHM	Full Width Half Maximum
SNS	Semi-Nano Shell
RIE	Reactive Ion Etching
SLG	Soda Lime Glass
SEM	Scanning Electron Microscopy

NSL	Nanosphere Lithography
SERS	Surface Enhancement Raman Spectroscopy
LOD	Limit Of Detection
EDX	Energy Dispersive X-ray Spectroscopy
FFT	Fast Fourier Transform
EOT	Extraordinary Optical Transmission
EBL	Electron Beam Lithography
BSA	Bovine Serum Albumine
SPPE	Surface Plasmon Polaritons Excitation
E-SP	Extended Surface Plasmons
L-SP	Localized Surface Plasmons

List of Figures

List of Tables

Introduction

The interest in using the Surface Plasmon Resonance (SPR) of metal structures to realize sensing devices was started in the first years of 1980. [8] The SPR sensors are used in many fields including the analysis for the food quality [9], for the environmental monitoring [10] and for pharmaceutical or medical diagnostics. [11–14]
They are based on the excitation of surface plasmons (SP) at a metal/dielectric interface. SP can be subdivided in extended SP (E-SP) and localized SP (L-SP). The L-SP, in particular, are characterized by a strong field confinement, and this property can be exploited for biosensing. Indeed, in the last twenty years, a very intense research activity has been focused on the investigation and the use of noble metal nanoparticles with different shapes to realize devices for biological detection. [15–22] The sub-wavelength field localization and the consequent strong enhancement is used to boost the interaction between the incident light and the analytes in a limited region around the nanostructures to achieve improved optical sensing either by measuring the shift in the localized surface plasmon resonance (LSPR) or by using Surface Enhancement Raman Spectroscopy (SERS) enhanced signal. The principal aim of those studies was to design innovative nanostructures, whose plasmonic properties can be exploited to realize optical biosensors for the label-free and high-specificity detection of low concentrations (below the pM level) of biomolecules with low molecular weight. The specificity of the detection can be obtained by functionalizing the nanostructures with suitable receptors, which are able to selectively bind the corresponding analyte only. In this way, the desired analyte, and only that one, is confined in the localized field region, so that the enhanced interaction with light is experienced only by the desired analyte. The detection event is characterized by the change in the optical properties of the nanostructures, which, in turn, is due to the change of the refractive index around them as the analytes bind to the receptors. Compared to other types of biosensors, the high sensitivity of L-SP-based confined nanostructures allows avoiding the use of an optical marker, obtaining a label-free detection by measuring the change of the extinction

spectrum with a simple and inexpensive transmission technique. [14] Another advantage in the use of these systems is that their size is comparable to that of biological molecules, such as proteins or nucleic acids. As a consequence, in these cases, they can be exploited even at the single-molecule detection level. [23]

Generally, the L-SP sensors, are based on nanoparticles bound to a substrate rather than in solution, to avoid their intrinsic instability and the aggregation as a consequence of variations of the pH or temperature. [14, 24]. Many kinds of plasmonic nanosystems have been investigated, such as nano-disks, nano-rings [25], nano-holes [26], nano-prisms [27], nano-shells [28–30], nano-rods [31], [32], [18], nano-gaps [33], nano-dots [34], nano-crescent moon structures [20]. One of the most simple, inexpensive and used patterning technique to obtain nanoparticles organized in two-dimensional ordered arrays with high control on size, morphology and composition, is the Nanosphere Lithography (NSL). [27] In this thesis we investigated the use of extended and localized SP excitations of ordered nanoarrays to develop label-free biological sensors. The samples were based on noble metals (gold and silver) in mono-elemental form, multilayer or alloy. All the nanoarrays were based on a hexagonal lattice which was due to the hexagonal lithographic mask used for the synthesis. In particular, we exploited the extraordinary optical transmission (EOT), supported by extended SP excitations, of Ag-Au nanoholes arrays (NHA)for molecules detection. EOT and E-SP excitations are dependent by the refractive index of the medium surrounding NHA. This property was exploited for the use of NHA as very specific and sensitive biosensors. L-SP-based nanoarrays were also studied. In particular the LSPR properties of Ag NPA and Au:Ag alloy SNSA, which are expressed by the LSPR peak in the visible-NIR range, were investigated. The samples were functionalized with a biological couple receptor-analyte and the variation of the LSPR peak with the refractive index change was monitored. The present thesis is organized as follows:

Chapter 1 will describe the interaction properties of electromagnetic radiation and materials, in particular in the case of noble metals.

Chapter 2 will describe the commercial SPR-sensors and the strategies reported in literature to optimize the performances of biological sensors based on localized and propagating surface plasmons.

Chapter 3 will describe the techniques used to synthesize ordered nanoarrays, the effect of the synthesis parameters on the morphological properties of the samples and the Van Duyne's biofunctionalization protocol applied to functionalize the nanoarrays with bio-

logical molecules.

Chapter 4 will deal with the plasmonic biosensing performances of Semi-NanoShell Array and the comparison with the NanoPrisms Array.

Chapter 5 will deal with the Extraordinary Optical Transmission of NanoHoles Array and the investigation of this property for biosensing applications.

Chapter 6 will deal with the SERS performances obtained with NanoPrisms Array in function of the oxidation of Ag, by comparing experimental and theoretical results.

1 Electromagnetic radiation and metals: how do they interact?

The "core" of this thesis is the use of the optical properties at nanoscale of innovative materials to obtain ultra sensitive, label-free biosensors. These plasmonic properties involve mainly noble metals like gold and silver, and arise from the interaction of an electromagnetic wave with nanostructured metals, i.e. metallic structures with size in the order of or smaller than the incident field wavelength in the Vis-NIR range. Plasmonics is the part of the nanophotonics which studies how this confinement at the metal surfaces leads to a high local field amplification on scale lengths much smaller than the wavelength. In particular, this local field amplification opens the way to a great number of possible applications in the field of photonics. The two main categories describing the plasmonic properties of metals at the nano-scale are extended surface plasmons (E-SP) and localized surface plasmons (L-SP). In this thesis Au/Ag nanostructures which support E-SP or L-SP will be investigated as plasmonic transducers for biosensing.

1.1 Drude Model and its corrections for noble metals

Maxwell's equations are the fundamental theory used to describe the interaction between electromagnetic field and materials. Metals are characterized by different behavior in the regimes frequency from UV to infrared. For low frequencies (λ up to visible range) the electromagnetic field is strongly reflected and there is not propagation inside the metals. For higher frequencies (Near infrared-visible) the penetration of the radiation and, as a consequence, the dissipation increases. In the UV range metals show a dielectric behavior and the radiation propagates into them. The electronic band structure of different metals is responsible for the dielectric behavior leading to different properties; as an example alkali metals show an ultraviolet transparency while noble metals show an high absorption

of radiation in UV frequencies. This absorption, which characterize gold and silver in particular, is due to electrons transitions between electronic bands.
James Clerk Maxwell [1831-1879] unified in a set of 4 equations the interaction between a material and electric and magnetic fields, starting from Gauss's, Faraday's and Ampere's laws. These equations describe the relation between **D** (the dielectric displacement),**B** (the magnetic induction),**H** (the magnetic field) and **E** (the electric field) with ρ_{ext} (the external charge density) and $\mathbf{J}_{ext}$ (the current density) [1]:

$$\nabla \cdot \mathbf{D} = \rho_{ext} \tag{1.1}$$

$$\nabla \cdot \mathbf{B} = 0 \tag{1.2}$$

$$\nabla \times \mathbf{E} = -\frac{\partial \mathbf{B}}{\partial t} \tag{1.3}$$

$$\nabla \times \mathbf{H} = \frac{\partial \mathbf{D}}{\partial t} + \mathbf{J_{ext}} \tag{1.4}$$

The link between the polarization **P** and the magnetization **M** and the four macroscopic fields, **D**,**B**,**H**, and **E** is expressed by the following equations:

$$\mathbf{D} = \varepsilon_0 \mathbf{E} + \mathbf{P} \tag{1.5}$$

$$\mathbf{H} = \frac{1}{\mu_0}\mathbf{B} - \mathbf{M}. \tag{1.6}$$

where ε_0 is the electric permittivity in vacuum, $\varepsilon_0 \approx 8.854 \times 10^{-12}$ F/m, while μ_0 is the magnetic permeability in vacuum, $\mu_0 \approx 1.257 \times 10^{-6}$ H/m. Neglecting the magnetic response by considering not magnetic media, the effect of an electric field impinging on a material can be described by the polarization **P**, which is the average of microscopic dipoles orientations whit the incident field. **P** is a material property defined as the electric dipole moment per unit volume. The internal charge density ρ_{int} and **P** are related by $\nabla \cdot \mathbf{P} = -\rho_{int}$. Imposing the charge conservation ($\nabla \cdot \mathbf{J} = -\frac{\partial \rho}{\partial t}$) we arrive to the equation between the current densities (**J**) and the polarization:

$$\mathbf{J} = \frac{\partial \mathbf{P}}{\partial t}. \tag{1.7}$$

Combining the first Maxwell equation with equation 1.5 and taking into account that $\rho_{ext} + \rho = \rho_{tot}$, $\nabla \cdot \mathbf{E}$ results:

$$\nabla \cdot \mathbf{E} = \frac{\rho_{tot}}{\varepsilon_0}. \tag{1.8}$$

Considering linear, isotropic and non magnetic materials, the constitutive relations between the four macroscopic fields and the material properties in terms of ε and μ are:

$$\mathbf{D} = \varepsilon\varepsilon_0\mathbf{E} \tag{1.9}$$

$$\mathbf{B} = \mu\mu_0\mathbf{H}. \tag{1.10}$$

where ε is the relative dielectric constant and μ is the relative permeability ($\mu = 1$ for non magnetic media).
The material response, described by the polarization $\mathbf{P}$, and the incident field $\mathbf{E}$ are related by ε_0 and the dielectric susceptibility χ:

$$\mathbf{P} = \varepsilon_0\chi\mathbf{E}. \tag{1.11}$$

The important relation we have to consider is between the internal current density $\mathbf{J}$ and the electric field $\mathbf{E}$, which are related by the conductivity σ:

$$\mathbf{J} = \sigma\mathbf{E}. \tag{1.12}$$

The most important quantities to describe the material response to an impinging electromagnetic field are ε and σ. We have to take into account that the response of the material is strongly dependent by the radiation angular frequency ω and by the wave vector $\mathbf{K}$. This is expressed by the following equation:

$$\varepsilon(\mathbf{K},\omega) = 1 + \frac{i\sigma(\mathbf{K},\omega)}{\varepsilon_0,\omega}. \tag{1.13}$$

$\varepsilon(\mathbf{K},\omega)$ can be simplified into $\varepsilon(\mathbf{K}{=}0,\omega)$ and so $\varepsilon(\omega)$ in the approximation of spatially local response. This is correct when the λ in the medium is higher with respect to the size of unit cell or the electrons mean free path, i.e. this is verified in the ultraviolet region. The main property which describes how a material interacts with an electromagnetic field is

the dielectric function $\varepsilon(\omega)$, usually defined as:

$$\varepsilon(\omega) = \varepsilon_1(\omega) + i\varepsilon_2(\omega) \tag{1.14}$$

The dielectric function is related to refractive index ($\tilde{n}$) by these equations:

$$\tilde{n} = \sqrt{\varepsilon} \tag{1.15}$$

$$\varepsilon_1 = n^2 - k^2 \tag{1.16}$$

$$\varepsilon_2 = 2nk \tag{1.17}$$

$$n^2 = \frac{\varepsilon_1}{2} + \frac{1}{2}\sqrt{(\varepsilon_1)^2 + (\varepsilon_2)^2} \tag{1.18}$$

$$k = \frac{\varepsilon_2}{2n} \tag{1.19}$$

where k is the extinction coefficient and describes the absorption of the incident field by the medium. It is related to α (the absorption coefficient) by the Beer's law:

$$I(x) = I_0 e^{-\alpha x} \tag{1.20}$$

$$\alpha(\omega) = \frac{2k(\omega)\omega}{c} \tag{1.21}$$

The imaginary part of ε (ε_2) describes the radiation absorption by the propagation through the medium. In a wide range of frequencies of the incident field the metal behavior is approximated to a plasma model, based on a free electron gas. This is also known as Drude model. The Drude model is based on the following assumptions:

- the free electrons of a metal form a free electrons gas;
- the electrons oscillate in presence of an electromagnetic field in a positive ions lattice;
- the electron-electron interactions are neglected;
- the electrons motion is random for the collisions with positive ions;
- the ions are considered immovable for their large mass;
- the details of the positive lattice potential are not included.

The electron-ion collisions occur at frequency $\gamma = 1/\tau$ (where τ is the relaxation time, (10^{-13}-10^{-14} s at room T)). If these assumptions are satisfied, the dielectric function of a free electron gas can be calculated in an harmonic oscillator approximate model. The equation of motion for an electron in presence of an external electric field **E** in this approximation

is:

$$m\ddot{\mathbf{x}} + m\gamma\dot{\mathbf{x}} = -e\mathbf{E}. \tag{1.22}$$

We consider an harmonic time dependance of the external field, $\mathbf{E} = \mathbf{E_0}e^{-i\omega t}$. One solution of the equation which describe the electron oscillation is $\mathbf{x} = \mathbf{x_0}e^{-i\omega t}$. If we use this solution in the equation 1.22 we obtain:

$$\mathbf{x}(t) = \frac{e}{m(\omega^2 + i\gamma\omega)}\mathbf{E}(t). \tag{1.23}$$

The displaced electrons give a contribution to the polarization in terms of $\mathbf{P} = -ne\mathbf{x}$. With the appropriate substitutions in equation 1.5 the relation between the macroscopic fields $\mathbf{D}$ and $\mathbf{E}$ became:

$$\mathbf{D} = \varepsilon_0\left(1 - \frac{\omega_p^2}{\omega^2 + i\gamma\omega}\right)\mathbf{E}, \tag{1.24}$$

where ω_p is the plasma frequency of free electron gas ($(\omega_p)^2 = ne^2/\varepsilon_0 m$); m is the effective optical mass of each electron and n is the metal electron density. In this model m can be determined from bands curvature from the band structure of different metals. The plasma frequency is an intrinsic property of metals and it is usually in the ultraviolet frequency range. The dielectric function of a gas of free electrons which satisfies the Drude Model assumptions is:

$$\varepsilon(\omega) = 1 - \frac{(\omega_p)^2}{\omega^2 + i\gamma\omega} \tag{1.25}$$

$$\varepsilon_1(\omega) = 1 - \frac{(\omega_p)^2\tau^2}{1 + \omega^2\tau^2} \tag{1.26}$$

$$\varepsilon_2(\omega) = \frac{(\omega_p)^2\tau}{\omega(1 + \omega^2\tau^2)} \tag{1.27}$$

In the high frequency limit ($\omega \gg \tau$) the dielectric function is essentially real ($\varepsilon(\omega) = 1 - \omega_p^2/\omega^2$). This model can be applied in a wide range of frequencies, except for the region at which the interband transitions occur. In particular, for noble metals, such as gold and silver, the interband transitions occur in the visible and near Uv range. These transitions are due to the excitation of electrons from the filled band below the Fermi surface to higher energy bands. This phenomena leads to an increase of the imaginary part of the dielectric function, ε_2, and Drude Model can't be applied as is. In the case $\omega \ll \tau^{-1}$, i.e. in the regime of low frequencies, $|\varepsilon_2|$ exceeds on $|\varepsilon_1|$ and metals are very good

absorber for the radiation. The plasma model in the regime of $\omega \gg \omega_p$ ($\varepsilon \to 1$) can not be applied in particular for noble metals such as Ag, Au and Cu. For these metals, in the frequency region $\omega > \omega_p$, there is another contribution to the polarization. $\mathbf{P}$ is not due only to free s electrons but there is a contribution from the electron in d bands close to the Fermi surface, and a correction to the model is needed. The correction to $\mathbf{P}$ is done by adding $\mathbf{P}_\infty = \varepsilon_0 (\varepsilon_\infty - 1)\mathbf{E}$ to eq. 1.5. $\mathbf{P}$ now represents only the polarization due to free electrons. Using this correction the dielectric function for a free electron gas is:

$$\varepsilon(\omega) = \varepsilon_\infty - \frac{\omega_p^2}{\omega^2 + i\gamma\omega}. \tag{1.28}$$

The dielectric constant of these noble metals was experimental measured by Johnson and Christy (1972). Using the Drude Model described in equation 1.28, we can see in figure 1.1 that this model is a good representation of the experimental data only in the region of energies lower than the band transitions. To introduce the correction to this mismatch we

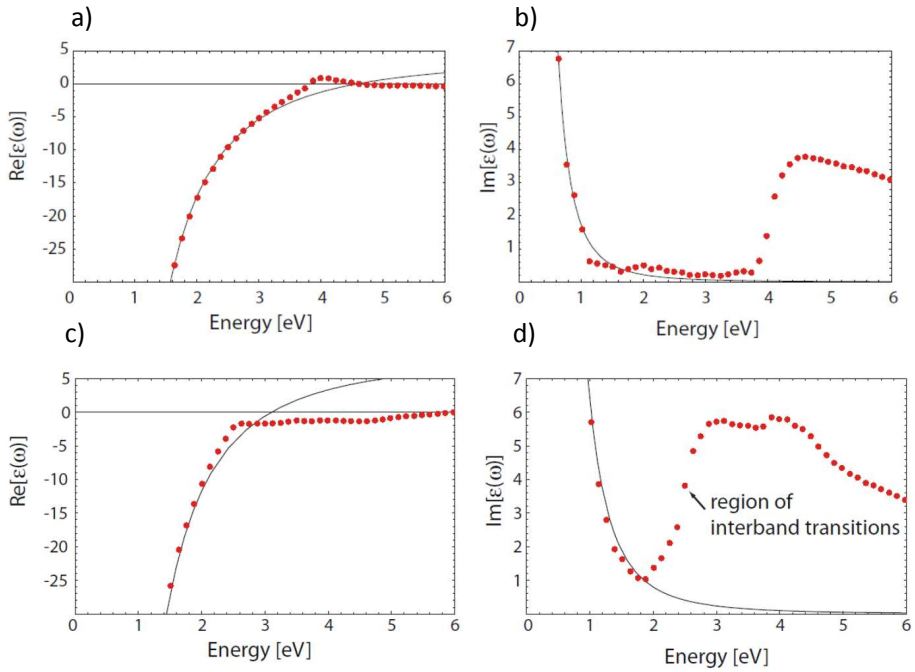

Figure 1.1: a),b) Real and imaginary part of the dielectric constant of Ag from the literature values of Johnson and Christy (red dots) and fit with the model described in equation 1.28 (black line); c),d) The case of gold. [1]

have to consider the bound electrons, which are responsible for the interband transitions. This is done by adding a term to the equation of motion 1.22 in which ω_j is the resonance

frequency of a bound electron. This correction takes into account the processes due to bound electrons with an additional Lorentz-oscillator function $F_j/(\omega_j^2\text{-}\omega^2\text{-}i\gamma_j\omega)$, where F_j is the oscillator strength of the dipolar transition. The Lorentz-oscillator function in the final dielectric constant is calculated for each transition j from 1 to N. A_j, B_j and C_j are the corresponding coefficients.

$$m\ddot{\mathbf{x}} + m\gamma\dot{\mathbf{x}} + m\omega_j^2\mathbf{x} = -e\mathbf{E}. \tag{1.29}$$

$$\varepsilon(\omega) = \varepsilon_\infty + \frac{i\sigma}{\varepsilon_0\omega} + \sum_{j=1}^{N} \frac{C_j}{\omega^2 + iA_j\omega + B_j}. \tag{1.30}$$

The fit of the Johnson and Christy data for gold and silver with the equation 1.30 is in a very good agreement.

1.2 Surface Plasmons (SP)

1.2.1 Extended Surface Plasmons (E-SP)

Extended Surface Plasmons (E-SP) are electromagnetic surface waves which propagate at a metal/dielectric interface. These electromagnetic excitations are evanescently confined in the perpendicular direction with respect to the interface plane. E-SP arise from the coupling between the electron plasma of a metal and an incident electromagnetic field.
The properties of these excitations can be studied using the Maxwell's equations. They are solved in the following simple case, taking into account these assumptions:

- there is a planar interface between two media, a metal(ε_1) and an insulator(ε_2);
- the insulator is a non-absorbing medium with $\mathrm{Re}[\varepsilon_2] > 0$;
- the metal is described by $\mathrm{Re}[\varepsilon_1(\omega)] < 0$;
- z direction defines the perpendicular direction to the interface;
- x,y are the coordinates of the interface plane;
- the direction of the traveling wave is x;
- ε changes only in the z direction ($\varepsilon = \varepsilon(z)$).

The initial point is to consider the wave equation:

$$\nabla^2\mathbf{E} - \frac{\varepsilon}{c^2}\frac{\partial^2\mathbf{E}}{\partial t^2} = 0. \tag{1.31}$$

The equation has to be solved for the two media (metal vs insulator). We consider an electric field with a harmonic time dependence described by $\mathbf{E}(\mathbf{r},t) = \mathbf{E}(\mathbf{r})\, e^{-i\omega t}$, to obtain the *Helmholtz equation*:

$$\nabla^2\mathbf{E} + k_0^2\varepsilon\mathbf{E} = 0, \tag{1.32}$$

where $k_0 = \omega/c$ is the wave vector of the propagating wave in vacuum. The electric field of the traveling wave in x direction is $\mathbf{E}(x,y,z) = \mathbf{E}(z)\, e^{i\beta x}$. β is called the propagation constant of the waves and it is the component of the wave vector in the propagation direction x ($\beta = k_x$). The important results obtained by solving the equation 1.32 is the dispersion relation:

$$\beta = k_0\sqrt{\frac{\varepsilon_1\varepsilon_2}{\varepsilon_1+\varepsilon_2}}. \tag{1.33}$$

This relation is also valid for conducting media with complex dielectric function, and so a possible attenuation of the field is included. The solution of Maxwell's equations for propagating waves confined to the interface (this means an evanescent decay in the perpendicular direction) with a p polarization requires that $\mathrm{Re}[\varepsilon_1] < 0$ if $\mathrm{Re}[\varepsilon_2] > 0$. Materials with opposite signs of the real part of their dielectric function can support SP, i.e. a metal vs insulator. The confinement of the wave can be expressed by $\hat{z} = 1/|k_z|$, where k_z is the component of the wave vector perpendicular to the interface. $\hat{z}$ is the evanescent decay length of the fields. As it can be seen in figure 1.2 a, the E-SP dispersion curve lies to the right of the light line in air, and direct excitation is thus hindered. To achieve E-SP excitations alternative phase-matching conditions are required. The most common techniques to overcome this requirement are based on charged particle impact, prism coupling (see figure 1.2 b), grating coupling, highly focused optical beams and near-field excitation.

The use of a periodic structure, such as a grating or a holes array with period a, is very interesting to overcome the difference between the k_x ($k\sin\theta$) of the incident radiation and β by this relation:

$$\beta = ksin\theta \pm \Delta k_x \tag{1.34}$$

$$\beta = ksin\theta \pm \nu 2\pi/a \tag{1.35}$$

where ν is an integer (1,2,3...) and $2\pi/a$ is the reciprocal vector of the periodic structure. The reverse of this phenomena is possible: E-SP on a grating structure can couple to light

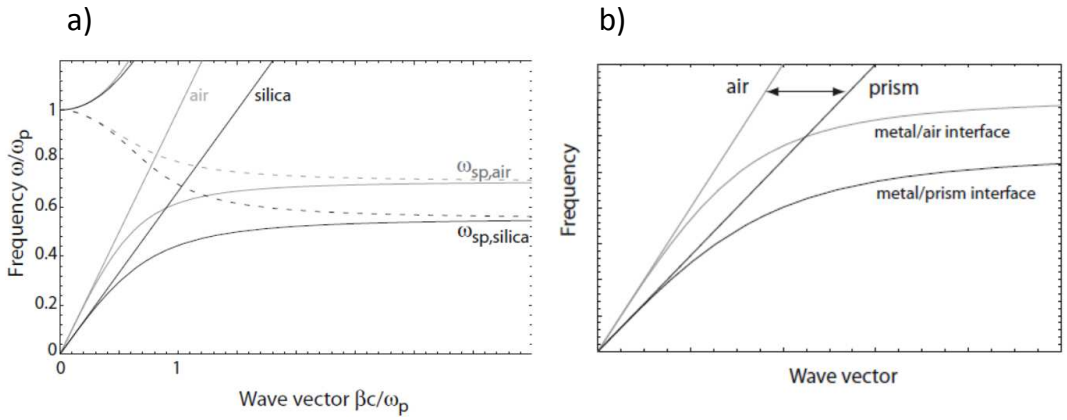

Figure 1.2: a) Dispersion relations of E-SP of a Drude metal/air or silica interface. b) Dispersion relations of E-SP in presence of the prism coupling. [1]

and radiate. The other most common strategy to achieve SP excitation is based on the prism coupling. This is based on a multilayer system: a thin metal film is in the middle of two insulators with different dielectric function. This is the strategy used in all commercial SPR sensors. One of the insulator is based on a prism with higher refractive index with respect to the other dielectric (usually is air ε=1). The impinging radiation is reflected at the interface between the prism and the metal ($k_x = k\sin\theta\sqrt{\varepsilon_{prism}}$). SP are excited and can propagate at the metal/air interface, with β is between the light line of air and the prism, as indicated in figure 1.2 b. The typical configurations of prism coupling are Krestchmann or Otto. In the first one a thin metal layer is deposited on the top surface of a prism, while in the second there is an air gap between the metal film and the prism. These methods are both based on total internal reflection. In Krestchmann configuration the radiation impinge on the glass prism with an angle higher than the critical angle for total internal reflection. The reflected beam excites E-SP waves at the second metal/air interface. In the Otto configuration the total internal reflection occurs at the prism/air interface, and by tunneling the E-SP are excited to the metal/air interface.

1.2.2 Localized Surface Plasmons (L-SP)

Localized surface plasmons (L-SP) are confined excitations with different properties with respect to the extended case. These excitations occur at the interface between a sub-wavelength noble metal particle and a dielectric medium, when interacting with an incident electromagnetic field. It is due to the coupling of the free electron plasma of the metal

with the field. The most simple case to describe this phenomena is a metallic spherical nanoparticle embedded in a dielectric medium. The incident field causes an oscillation of the free electrons. The curved surface of the particle is the responsible of a restoring force acting on the electrons. When particular conditions are satisfied, this phenomena results in a resonance which amplifies the field inside and in the near-field zone outside the nanoparticle. This resonance is named Localized Surface Plasmon Resonance (LSPR). The excitation of LSPR can be obtained by direct illumination, and this is an advantage for optical applications with respect to E-SP. Noble metals such as gold and silver are the best performer of plasmonic phenomena, for their intrinsic dielectric properties. The characteristic λ of a LSPR depends on the morphological and compositional properties of the nanoparticles involved and on the dielectric function of the medium at the interface. In the case of Ag/Au nanoparticles in a wide range of configurations, the LSPR can be excited by using radiation in the visible-near infrared region. The LSPR theory is fully explained by Mie Theory for spherical isolated sub-wavelength particles. When the geometry is more complicated or interaction effects between particles occur, numerical simulations based on the Maxwell's equations can be used to study the system.

Quasi-static approximation

We now consider an isolated spherical particle with diameter d and dielectric function $\varepsilon(\omega)$, embedded in a non-absorbing medium with dielectric constant ε_m . If the wavelength of the incident beam is much larger than d ($d \ll \lambda$), we can use the quasi-static approximation. The adjective "static" refers to the phase of the oscillating field which can be considered constant over the volume of the particle. The most simple case is based on these assumptions (see figure 1.3) and it is described by Mie Theory:

- the particle shape is a sphere of radius a;
- the sphere is homogeneous and isotropic with dielectric constant $\varepsilon(\omega)$;
- the dielectric medium at the interface is non-absorbing ($\varepsilon = \varepsilon_m$);
- an uniform and static field $\mathbf{E}$ illuminates the sphere $\mathbf{E} = E_0\hat{\mathbf{z}}$.

In the quasi-static approximation the sphere can be considered an ideal dipole under the effect of a static field. $\mathbf{E}$ induces a dipole moment $\mathbf{p}$ inside the sphere proportional to $|\mathbf{E}_0|$, expressed by this equation:

$$\mathbf{p} = 4\pi\varepsilon_0\varepsilon_m a^3 \frac{\varepsilon - \varepsilon_m}{\varepsilon + 2\varepsilon_m}\mathbf{E}_0 \tag{1.36}$$

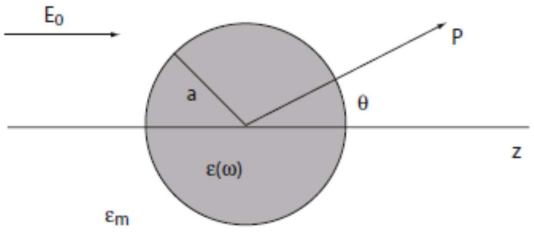

Figure 1.3: Homogeneous sphere in an electric media and illuminated with an electrostatic field with lines parallel to z axis.

Using the relation between $\mathbf{p}$ and the polarizability α ($\mathbf{p}$=$\varepsilon_0\varepsilon_m\alpha\mathbf{E}_0$) we obtain:

$$\alpha = 4\pi\varepsilon_0\varepsilon_m a^3 \frac{\varepsilon - \varepsilon_m}{\varepsilon + 2\varepsilon_m} \tag{1.37}$$

In this way we can note that α has a resonant enhancement for the minimum of $|\varepsilon + 2\varepsilon_m|$. If Im[$\varepsilon$] of the metal sphere is negligible the equation can be expressed by the Frölich condition:

$$Re\left[\varepsilon(\omega)\right] = -2\varepsilon_m \tag{1.38}$$

The Frölich condition shows the dependence of the Localized Surface Plasmon Resonance (LSPR) from the dielectric function of the medium which surrounds the nanoparticle: in particular for an increase of ε_m the resonance red-shifts. This is the principal optical feature of nanoparticles which are exploited as refractive-index sensors for many applications. Also the $\mathbf{E}$ inside and outside the particle is enhanced by this resonance, as reported in these equations ($\mathbf{n}$ is the unit vector):

$$\mathbf{E}_{in} = \frac{3\varepsilon_m}{\varepsilon + 2\varepsilon_m}\mathbf{E_0} \tag{1.39a}$$

$$\mathbf{E}_{out} = \mathbf{E_0} + \frac{3\mathbf{n}\left(\mathbf{n}\cdot\mathbf{p}\right) - \mathbf{p}}{4\pi r^3\varepsilon_0\varepsilon_m}, \tag{1.39b}$$

The field enhancement of a wide range of nanoparticles which differs in morphology, size and composition is exploited to amplify the detection signal of some techniques, such as the Surface Enhanced Raman Spectroscopy. Considering the scattering and absorption properties of nano-particles (with radius R), which are expressed in the respective cross-sections, we can note that for particles with radius R $\ll \lambda$ the absorption prevails on the

scattering:

$$\sigma_{sca} = \frac{k^4}{6\pi}|\alpha|^2 = \frac{8\pi}{3}k^4R^6\left|\frac{\varepsilon-\varepsilon_m}{\varepsilon+2\varepsilon_m}\right|^2 \tag{1.40a}$$

$$\sigma_{abs} = kIm\left[\alpha\right] = 4\pi kR^3 Im\left[\frac{\varepsilon-\varepsilon_m}{\varepsilon+2\varepsilon_m}\right]. \tag{1.40b}$$

Ellipsoidal particles

Bohren and Huffman in 1983 studied the polarizability of two particular cases of not spherical particles. These dipolar approximations are valid, as before, for particles smaller than the wavelength. The first case is that of ellipsoidal nanoparticles. For an ellipsoid with semiaxes $a_1 \leq a_2 \leq a_3$, the polarizability along the three axes α_i (i=1,2,3) results:

$$\alpha_i = 4\pi a_1 a_2 a_3 \frac{\varepsilon(\omega)-\varepsilon_m}{3\varepsilon_m + 3L_i(\varepsilon(\omega)) - \varepsilon_m} \tag{1.41}$$

where L_i are geometrical factors. In the case of prolate ($a_2 = a_3$) or oblate ($a_1 = a_2$) spheroids, two resonances are observed due to electron plasma oscillations along the minor or major axis. The resonance originates from the oscillation along the major axis of a spheroid is red-shifted with respect to a sphere of the same volume. This result shows that it is possible to control the LSPR frequency for example by changing the particles aspect-ratio. Another particular case they studied is that of core/shell particles. These are constituted by a dielectric inner core ($\varepsilon_1(\omega)$) and a thin metallic concentric coverage ($\varepsilon_2(\omega)$). The polarizability α is:

$$\alpha = 4\pi a_2^3 \frac{(\varepsilon_2-\varepsilon_m)(\varepsilon_1+2\varepsilon_2) + f(\varepsilon_1-\varepsilon_2)(\varepsilon_m+2\varepsilon_2)}{(\varepsilon_2+2\varepsilon_m)(\varepsilon_1+2\varepsilon_m) + f(2\varepsilon_2-2\varepsilon_m)(\varepsilon_1-\varepsilon_2)} \tag{1.42}$$

where $f = a_1^3/a_2^3$, a_1 and a_2 are the inner and outer radius respectively, ε_m is the surrounding medium.

Energy shift of LSPR for larger particles

If we consider larger particles, the quasi static approximation can not be applied because there is a phase change of the external field across the particle volume. In this case a more complex electrodynamic approach is used.

For a larger sphere of volume V the polarizability obtained by the Mie Theory is, at the

second order,

$$\alpha = \frac{1 - \frac{1}{10}(\varepsilon + \varepsilon_m)\, x^2 + O(x^4)}{\frac{1}{3} + \frac{\varepsilon_m}{\varepsilon - \varepsilon_m} - \frac{1}{30}(\varepsilon + 10\varepsilon_m)\, x^2 - i\frac{4\pi^2 \varepsilon_m^{3/2}}{3}\frac{V}{\lambda_0^3} + O(x^4)}, \tag{1.43}$$

where:

- $x = \frac{\pi R}{\lambda_0}$ is the *size parameter*;
- x^2 at numerator takes into account the retardation of the field over V (resonance is energy shifted);
- x^2 at denominator includes the retardation of the depolarization field into the particle (resonance is energy shifted);
- x^2 at denominator also reduces the influence of $\mathrm{Im}[\varepsilon(\omega)]$ increasing the polarization;
- the imaginary term at denominator is due to radiation damping (L-SP decay into photons.)

For larger particles the restoring force is lower because the opposite charges are at higher distance with respect to very small particles. The energy of the resonance is red-shifted with the increase of the particle's size. When increasing the size of particles which can not be treated with the quasi static approximation, the radiative decay into photons and the radiation absorption take to a damping of the LSPR. In particular for noble metals the absorption is due to intra/inter band transitions. The first occur in the conduction band, while the second are electron excitations from d to sp band.

Electromagnetic coupling in ordered particles arrays

In general in particles arrays additional shifts are expected for the interaction between the localized modes. The random or ordered configuration of the particle's ensemble can affect the type of interaction. In particular, for random structures the coupling effects can occur only for very close particles. In the case of ordered arrays of particles with size a and interparticle distance d, with $a \ll d$, particles can be treated as isolated dipoles. In the case of very close particles and $d \ll \lambda$, in the space between them there is an high field localization and a scattering suppression. The particles can be seen as interacting dipoles. This is a near field interaction which prevails with a d^{-3} distance dependence. These regions of high field amplification are called hot spots. The LSPR frequency is different from the case of isolated particles, and it is red or blue shifted depending by the polarization of the incident beam. This is due to the difference in the charge distribution of the particles, and

so to the electron plasma restoring force, with the polarization. For higher distance between the particles the far-field interaction dominates with a d^{-1} dependence. The frequency of LSPR and the spectral width are affected also by the far field coupling.

2 SPR-based Biosensors

2.1 Introduction

A sensitive, specific and fast detection of biological markers indicating normal or pathogenic biological processes is a very important purpose in biotechnology. To achieve an efficient detection, in particular for medical diagnostics, there is the necessity to detect very low concentrations (below the picomolar, pM level) of small molecules (with molecular weight, MW less than 8kDa) in real time and without the use of labelling strategies. Biological and chemical detection has been strongly improved by innovative optical sensors based on Surface Plasmon Resonance (SPR). SPR detection can be applied to any kind of biological or chemical analyte such as proteins, oligonucleotides, virus, bacteria, toxines, DNA chains, cancer markers, allergy markers, antibodies, drugs and hormones. The first experimental works on the use of SPR for gas and biological sensing are dated 1982. The world's first SPR-based detection device for biological applications was commercialized in the end of 1990, from BIAcore®. Nowadays, SPR biosensors are commercialized by several companies and they are used to quantify and characterize the interactions between biomolecules in real time and without labeling. Moreover, there is a very active and intense research in the academic laboratories and in the research centers of companies to optimize the performances of SPR sensors in terms of sensitivity, resolution and limit of detection. To better understand the strategies used to improve the performances of SPR sensors a brief analysis of the physical mechanism which allows the sensing detection will be presented. SPR biosensors are a class of optical sensors based on the E-SPR of noble metals (Au,Ag) at the nanoscale. As explained in chapter 1 these electromagnetic excitations occur at the interface between two media characterized by the real part of the dielectric function $\varepsilon(\omega)$ of opposite sign such as a metal ($\mathrm{Re}(\varepsilon(\omega)) < 0$) and a dielectric ($\mathrm{Re}(\varepsilon(\omega)) > 0$)). The detection mechanism is based on the measure of a refractive index change occurring at the interface between the metal and the surrounding dielectric medium. The propagation

constant (β) of E-SP at the interface between a semi-infinite dielectric and a metal is expressed by [7]:

$$\beta = k\sqrt{\frac{\varepsilon_m n_s^2}{\varepsilon_m + n_s^2}} \tag{2.1}$$

where k is the free space wave number, ε_m is the metal dielectric function ($\varepsilon_m = \varepsilon_{mr} + i\varepsilon_{mi}$), and n_s is the dielectric refractive index. Since E-SP occur at the interface between two media with dielectric function of opposite signs ($\varepsilon_{mr} < - n_s^2$), β will be always higher than the propagation constant of electromagnetic (e.m.) wave into the dielectric. This means that the excitation of E-SPR can not be achieved directly by illuminating a planar interface metal/dielectric. The momentum of the incident radiation has to be increased to match that of the E-SP. This additional momentum can be obtained by three main strategies: (i) the use of attenuated total reflection (ATR) in prism couplers; (ii) the use of ATR in optical waveguides; (iii) the use of diffraction at the surface of grating or periodic structures [35, 36]. All these strategies are sketched in figure 2.1.

2.2 SPR sensors

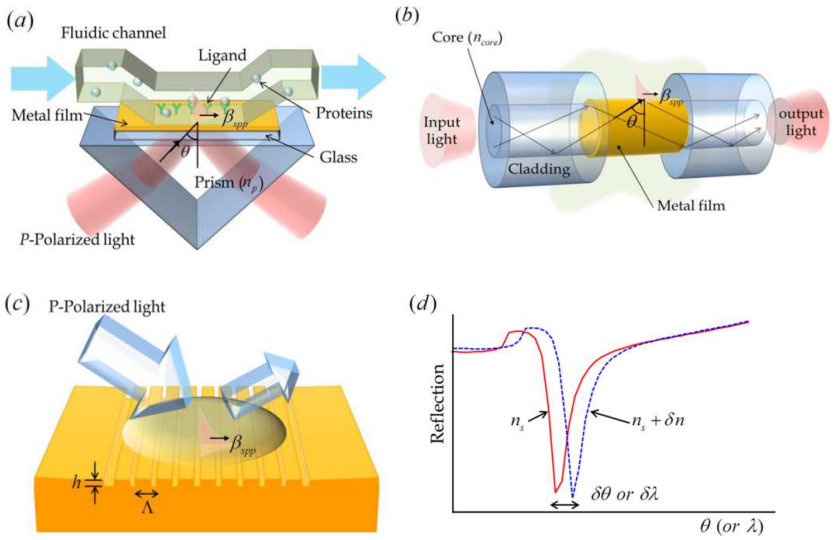

Figure 2.1: Basic schemes for SPR sensors with (a) Kretschmann configuration based coupling; (b) waveguide based coupling; (c) and grating coupling; (d) Reflection ratio of light due to SPR with angular modulation or wavelength modulation. [2]

Concerning equation 2.1, we can observe that E-SP may be supported by materials which

satisfy $\varepsilon_{mr} <$ - n_s^2. Noble metals like gold and silver are the best materials which fulfill this condition in the VIS-NIR range, with reasonably small losses. The more interesting characteristics of the E-SP which propagate at the interface between a thin metal layer (Au or Ag) and the water are reported in table 2.1. We can observe that the E-SP penetration depth is highly asymmetric, by comparing the corresponding values into the metal and into the dielectric, and that there is a higher confinement of the wave into the dielectric. In this feature lies the sensing mechanism of SPR sensors. Silver is the best plasmonic performer for its higher field localization into the dielectric with respect to gold, in particular for wavelengths in the visible range. Because of this high field localization into the dielectric, β of the E-SP and, as a consequence, the resonance condition, is strongly sensitive to the properties of the dielectric at the interface with the metal. The thin metal layer constitutes basically the transducing medium of the SPR sensors. The variations of the refractive index of the dielectric produce a change of the resonance condition to excite E-SP: this phenomenon can be detected by analyzing the properties of the excited optical wave. The detection approach of SPR-based sensors can be subdivided in four categories:

1. angular interrogation: the coupling between the incident monochromatic light and surface plasmon results in a dip in the angular spectrum of the reflected light (see figure 2.1 d);
2. wavelength interrogation: the polychromatic light-SPR coupling is observed as a dip in the wavelength of the reflected light (see figure 2.1 d);
3. intensity interrogation: the intensity of the output signal is measured at a single incidence wavelength and angle;
4. phase interrogation: the shift in phase of the detected wave is measured at a single incidence wavelength and angle.

The main properties that characterize the performances of SPR-based sensors are the *sensitivity* and the *resolution*. The sensitivity is the derivative of the SPR parameter with respect to the refractive index change. The sensitivity is expressed in deg RIU^{-1}, in nm RIU^{-1} or in % RIU^{-1} for angular, wavelength and intensity interrogation, respectively (RIU is the refractive index unit). The resolution is defined the minimum change in the monitored parameter to be resolved by the sensor, and it depends on the accuracy of the SPR parameter's measurements. The resolution is calculated by dividing the accuracy on the measure by the bulk refractive index sensitivity; it is quantified in Refractive Index

Metal layer λ	Ag λ= 630 nm	Ag λ= 850nm	Au λ= 630nm	Au λ= 850nm
Propagation length (μm)	19	57	3	24
Penetration depth into metal (nm)	24	23	29	25
Penetration depth into dielectric (nm)	219	443	162	400
Concentration of field in dielectric (%)	90	95	85	94

Table 2.1: Characteristics of surface plasmon polaritons waves at the metal-water interface. [7]

Unit (RIU). The transducing medium and the optical system define the sensitivity, the stability and the resolution of SPR sensor. To obtain an efficient biological sensing, e.g. in the field of medical diagnostics, the SPR affinity biosensors were developed; these systems are able to detect only a specific analyte in a solution containing multiple species. In SPR affinity biosensors a specific target molecule is immobilized on the transducing medium (the thin metallic film) and then the sensor is exposed to a liquid containing the corresponding ligand and other species. These sensors take advantage of the high affinity between some couples of target-ligand molecules. The *selectivity* of the biorecognition event depends on the choice of the appropriate target and on the immobilization method; these parameters have direct impact also on the sensitivity and on the *limit of detection* (LOD) of the SPR sensor. [8] The LOD is usually defined as the concentration of analyte that produces an output signal corresponding to 3 standard deviations of the signal measured for a sample with zero analyte concentration. [8]

2.2.1 Prism-coupled SPR sensors

The most commonly used geometry in SPR sensors is the Krestchmann configuration (see figure 2.1 a): an incident wave passes through a prism with high refractive index and it is totally reflected at the interface between the prism and a thin metal layer (thickness around 50 nm). This phenomenon generates an evanescent wave which penetrates into the metal. The condition reported in equation 2.1 for the propagating constant of the E-SP can be fulfilled by controlling the angle of incidence (θ) of the electromagnetic field. For

prism-coupled SPR sensors the matching condition is expressed by:

$$\frac{2\pi}{\lambda} n_p sin(\theta) = Re\{\beta\} \tag{2.2}$$

where n_p is the prism's refractive index. The matching of the resonant condition results in the coupling of the evanescent wave with the surface plasmon polaritons excitations at the metal/ air interface.

2.2.2 Gratings-coupled SPR sensors

The other common strategy to excite E-SP is the use of a metal grating, as reported in figure 2.1 c. An electromagnetic field arrives from the dielectric medium and impinges on the metal grating; the diffracted waves can be coupled to a surface plasmon if their total component of momentum parallel to the interface is equal to the propagation constant of the surface plasmon. This matching condition is expressed by:

$$\frac{2\pi}{\lambda} n_d sin(\theta) + m\frac{2\pi}{\Lambda} = \pm Re\{\beta\} \tag{2.3}$$

where n_d is the refractive index of the dielectric medium, θ is the angle of incidence, m is an integer which denotes the diffraction order and Λ is the pitch of the grating.

2.2.3 Biological detection by SPR-based sensors

Prism-coupled SPR-sensor and intensity interrogation

Many strategies were used to enhance the sensitivity of SPR sensors based on the intensity modulation. One innovative approach was based on the combination of magneto-optic activity of magnetic materials with surface plasmon excitations. Using this strategy, Sepúlveda and co-workers demonstrated an enhanced sensitivity by a factor of 3 with respect to common SPR techniques based on prism-coupler. Using a protein as analyte test (Bovine Serum Albumine) they obtained a resolution of 5×10^{-6} RIU. [37] One of the most widely approach used to achieve better performances in terms of sensitivity was based on SPR imaging, in particular for biological sensing. [38–40] SPR imaging is usually based on a prism-coupled SPR configuration. The detection signal is the intensity of the reflected light which is correlated to the distribution of the refractive index at the surface of the

metal thin film. Nelson and co-authors [41] used SPR imaging to detect small molecules such as ologonucleotides. SPR sensors based on nearinfrared SPR imaging were used to detect (18-base) unlabeled RNA and DNA oligonucleotides at concentrations as low as 10 nM, which corresponds to about 10^{-5} RIU. [41] SPR imaging technique was also studied with a controllable angle of incidence system. Protein-DNA interactions were measured and protein in concentration lower than 1 pg was measured. [42] An innovative approach based on SPR imaging was reported by Zybin and collaborators. [43] They exploited a dual-wavelength SPR imaging system and by using a sucrose solutions they attained an absolute resolution of 5×10^{-6} RIU. [43] They applied this technique to the detection of biological systems, such as the biotin-streptavidin couple, and they reported that a $\Delta n = 2 \times 10^{-6}$ RIU could be measured. Piliarik, Homola and co-authors [44] reported a new approach of SPR imaging based on polarization contrast and excitation of surface plasmons on spatially patterned multilayers. They obtained a limit of detection for oligonucleotides (23-base) lower than 100 pM. [44]

Prism-coupled SPR-sensor and angular or wavelength interrogation

In 1990 a SPR sensor based on angular interrogation was developed and commercialized by the company Biacore. The resolution of these systems is down 10^{-7} RIU. Homola and collaborators exploited many strategies to obtain higher performances by SPR sensors. [45, 46] They developed a wavelength division multiplexing SPR sensor (WDMSPR). Two configurations of WDMSPR sensors were exploited to obtain multiple plasmon excitations in different area of the trandsucing medium and, as a consequence, multiple dips of the signal output. With this strategy they obtained a resolution around 10^{-6} RIU. [45, 46] An ultra-high sensitive SPR sensor based on excitation of a long range surface plasmon was developed and reported in the works of Homola and Nenninger. [47] They obtained good agreement between theoretical and experimental results and a very high sensitivity of the sensors of 5.7×10^4 nm RIU^{-1} and a resolution of 2.5×10^{-8} RIU. [48]

2.2.4 SPR-affinity biosensors and biorecognition elements

SPR affinity biosensors are devices which are able to detect only a specific analyte in a solution of multiple species. To obtain this, a specific biorecognition element is immobilized on the surface of the transducing medium of a SPR sensor. The most widely strategy is

to use a flow cell in which the analyte in a liquid solution is in contact with the biorecognition element immobilized on the SPR transducing medium. Many kind of chemical or biological species can be bound to a gold surface by functionalization strategies. Biacore company provides a set of functionalized SPR gold surfaces for different kinds of applications. The ligands usually attached to the sensor surface are able to detect biotinylated proteins, peptides, nucleic acids, carbohydrates, lipids, lipid vesicles and liposomes. The performances of SPR sensors (sensitivity, specificity and LOD) are strongly affected by the choice of the appropriate biorecognition element and the strategy used to bind it on the surface. Antibodies are the most commonly used biorecognition elements, in particular for their high affinity against target molecules. Peptides are an alternative to antibodies for their easy manipulation, low cost and higher stability; they are used for the detection of antibodies or heavy metals. Oligonucleotide sequences, DNA or RNA based, are the last type of biorecognition element exploited to detect targets such as proteins, nucleic acids, cells and tissues. [49]

Strategy to immobilize the biorecognition elements on SPR surfaces

To obtain an efficient sensing strategy it is important to immobilize a sufficient number of biorecognition elements and in the same time to minimize the nonspecific binding. Moreover, the sensing element have to be immobilized on the substrate without altering its biological property. The strategy commonly used is based on the immobilization of a carboxymethylated dextran matrix or alkanethiolates self assembled monolayers (SAM) based on a mix of thiols with different chains (from n = 12 to higher). One of the great advantages in using SAM is due to the covalent bond between sulphur and gold and, as a consequence, the high stability of the biorecognition layer on the SPR substrate. Usually, two different thiols are immobilized, one is the spacer and it is shorter than the other. The spacer avoids the aspecific binding and it is commonly based on a oligo(ethylene glycol)-terminated alkanethiolate; this kind of molecules constitutes a nonfouling background on the sensor surface. The other thiol is longer than the spacer and it provides a functional group to attach the biorecognition element.

2.3 Biosensing performances of Localized SPR

As explained in chapter 1 surface plasmons can be divided in two categories: extended and localized. LSPR (localized surface plasmon resonance) is a nonpropagating surface plasmon excitation, which is supported by noble metals nanoparticles (NPs). This excitation can be observed by direct interaction between an electromagnetic field, usually in the visible-NIR range, ad nanoparticles. LSPR is observed as a peak in the extinction spectrum and can be measured with a simply, not expensive, fast and miniaturisable transmission technique. As the extended case, LSPR is very sensitive to refractive index changes at the interface between the nanoparticles and the dielectric surrounding medium. As previously described, all the commercialized sensor are based on the E-SP, but there is a great interest and activity in the scientific community in exploiting the L-SP to realize more specific and sensitive LSPR sensors due to the expected better sensitivity of L-SP with respect to E-SP, to small variations of the refractive index of tiny layers at their surface. This is due to the shorter decay length of L-SP in the dielectric with respect to E-SP (roughly an order of magnitude). In the last years, plasmonic biosensors based on LSPR have been demonstrated to have huge sensitivity to extremely small changes in the refractive index of the surrounding medium , as well as to very thin layers of biomolecules. [50] Very recently, plasmonic biosensors based on random distributions of non-interacting triangular nanoprisms were used for the first time for the detection of miRNAs in human plasma from pancreatic cancer patients, revealing sub-pMolar sensitivity and specificity, without the need of RNA extraction. [51] The shape and the position of the extinction spectrum, in particular the λ_{max}, depends on the particles shape, size, aspect ratio, composition and dielectric environment. These characteristics can be easily controlled by the chemical or lithographic synthesis techniques. NPs can be chemically synthesized and then immobilized on a substrate; this is a common strategy to obtain random distributions of nanoparticles. [51] Gold nanoparticles were usually bound to silanized silica or glass substrates. Otherwise, nanoparticles arrangements can be synthesized by lithographic techniques to obtain ordered arrays. The most common technique to obtain ordered arrays of nanoparticles is the Nanosphere Lithography, which will be described in the following chapters. [52] The transduction mechanism of LSPR sensors is the same used in the case of the extended SPR-sensors. Nanoparticles can be functionalized with biorecognition elements and then can be exposed to the analyte solution. The binding between the biorecognition element

and its corresponding target results in a variation of the refractive index at the metallic nanoparticle/dielectric medium interface. This refractive index variation can be detected as a red-shift of the LSPR extinction spectrum with a simply transmission technique, in real time, and without labelling strategies. The λ_{max} variation ($\Delta\lambda_{max}$) of LSPR peak in response to refractive index changes, can be described by the following equation:

$$\Delta\lambda \equiv m(n_{adsorbate} - n_{medium})(1 - e^{(-2d/l_d)}) \tag{2.4}$$

where m is the sensitivity factor in nm per RIU, $n_{adsorbate}$ and n_{medium} in RIU are the refractive indices of the adsorbed molecules on the NPs's surface and the dielectric surrounding them, d is the thickness of the adsorbed layer in nm and l_d is the field decay length in nm. [50] In order to achieve higher sensing performances, the sensitivity factor has to be maximized and the field decay length minimized.

2.3.1 Techniques used to enhance the sensitivity of LSPR sensors

Higher performance of LSPR sensors were obtained by Dahlin and co-authors. [53] They used an LSPR substrate based on nanoholes arrays to measure biotin-neutravidin binding with High resolution LSPR spectroscopy (HR-LSPR). [53] With this technique they obtained a detection limit lower than 0.1 ng cm^{-2}. HR-LSPR is based on the collection of more light by photodiode arrays and on the use of algorithms to calculate the maximum wavelength of the extinction spectrum in real time. Using a detection based on a large number of photons, they obtained a precision level comparable to that of commercial SPR sensors. Better performances in terms of sensitivity can be achieved also acting on the NPs morphological, compositional and dimensional features. These properties of nanoparticles affect the line width, the extinction intensity and the field decay length of LSPR. Increasing the aspect ratio (width/height) of NPs synthesized by NSL, higher sensitivity factor and field decay length can be obtained. Moreover, increasing the aspect ratio LSPR spectrum is red-shifted. Nanoparticles with sharp edges or tips are characterized by hot-spots with a strong electromagnetic field localization. The effect of these hot-spots is the increase of the sensitivity to local refractive index variations. A very high sensitivity was obtained by Hicks and collaborators [54] by using a silver film deposited on nanowells array. These LSPR substrates are characterized by a sensitivity factor of 538 nm RIU^{-1}, and by a plasmonic peak with a very narrow Full Width Half Maximum (FWHM). The figure of merit

(FOM) is calculated by the ratio m/FWHM; for Ag film over nanowells array the FOM is 14.5. [54] This value is much higher than those obtained with typical LSPR platforms: the silver nanoprisms arrays. This high FOM is due to the very narrow width of the plasmonic peak. The FWHM of the plasmonic peak is controlled by the imaginary part of the dielectric function of the noble metal which constitute NPs. $\mathrm{Im}(\varepsilon(\omega))$ takes into account the absorption properties of the metals. The FWHM is controlled also by the size and shape polydispersity of NPs. LSPR samples with a high size dispersion have broader and less sensitive plasmonic peaks. Nano-lithographic synthesis techniques such as Electron Beam Lithography (EBL) and Nanosphere Lithography (NSL) allow to overcome this effect and to obtain better performances of LSPR sensors with respect to those obtained by wet chemistry. [52, 55] Triangular Ag nanoparticle ordered arrays with in-plane width of 100 nm and out-of-plane height of 50 nm, synthesized by NSL, are characterized by a bulk refractive index sensitivity of $\approx$ 200 nm/RIU. [56] The strategic improvement of working with ordered arrays stems from the possibility to control the lateral electrodynamic coupling between the plasmonic nanostructures, thus producing intense electromagnetic hot-spots where field amplifications of 2-3 orders of magnitude can be attained, with a consequent increase in sensitivity with respect to the non-interacting case. [57] LSPR sensors are based on a large number of nanoparticles, but each of them can be treated as a single sensor provided that they are not e.m. coupled. Van Duyne and co-authors reported single nanoparticle sensing using dark-field microscopy. They obtained a red-shift of 40 nm in the LSPR spectrum induced from less than 60.000 small-molecule adsorbates from a single Ag nanoparticle. [58] Single Ag nanoparticles were also used to detect the protein Streptavidin; the LSPR red-shift obtained was $\approx$ 13 nm from the detection of less than 700 streptavidin molecules. All these results suggest that LSPR-based sensors can be exploited and optimized to achieve high sensitivity and selective detection of small molecules in extremely dilute conditions, in particular for applications in medical diagnostics.

3 Synthesis of Au/Ag nanoarray and biofunctionalization strategy

3.1 Synthesis of Au/Ag nanoarray by Nanosphere Lithography

3.1.1 Nanosphere Lithography (NSL)

The synthesis technique used in this work is based on the Nanosphere Lithography (NSL). [52] This is one of the most common, fast, simply and not expensive techniques to produce two-dimensional patterns at the nanoscale and on a large area (of the order of cm^2). By using NSL it is possible to synthesize ordered arrays of nanoparticles of different size, geometry and composition. The plasmonic properties of the nanoarrays are strongly affected by these structural features. The great advantage of NSL is the possibility to easily control the morphological and structural properties of the nanoarrays and as a consequence their optical properties. NSL was born from the concept of Natural Lithography by the works of Deckman and his collaborators in 1982. [59] They were inspired by the previous works of Fischer and Zingsheim [60] about the capability of colloidal Polystyrene (PS) nanoparticles to self-organize on a substrate by solvent evaporation. Following Deckman and co-workers suggested the idea of using these self-organized structures as lithographic masks. They investigated many parameters and applications about the self-organization of particles in a size range from hundreds nanometers up to few microns. [59] The evolution of Natural Lithography into Nanosphere Lithography was done later by the Van Duyne's group. [61] Van Duyne and co-workers were the first to use a monolayer of hexagonal close-packed nanospheres to synthesize silver nanoprisms arrays (NPA). [62] NSL can be considered a nanofabrication technique which is an hybrid between a bottom-up and top-down approach. It is essentially based on three main steps: (i) the self-assembling of

a two-dimensional monolayer (ML) of nanospheres on a substrate, (ii) the deposition of the material that constitutes the nanoarray through the nanosphere's interstices; (iii) the removal of the ML to obtain the nanopattern. This is the most common scheme to obtain NPA, as sketched in figure 3.1. The lateral size of nanoprisms a can be obtained by this equation, where D is the nanospheres diameter [63]:

$$a = \frac{3}{2}\left(\sqrt{3} - 1 - \frac{1}{\sqrt{3}}\right) D = 0.466R = 0.233D$$

The center-to-center interparticle distance between nanoprisms (d) is also dependent on D as:

$$d = \frac{1}{\sqrt{3}} D$$

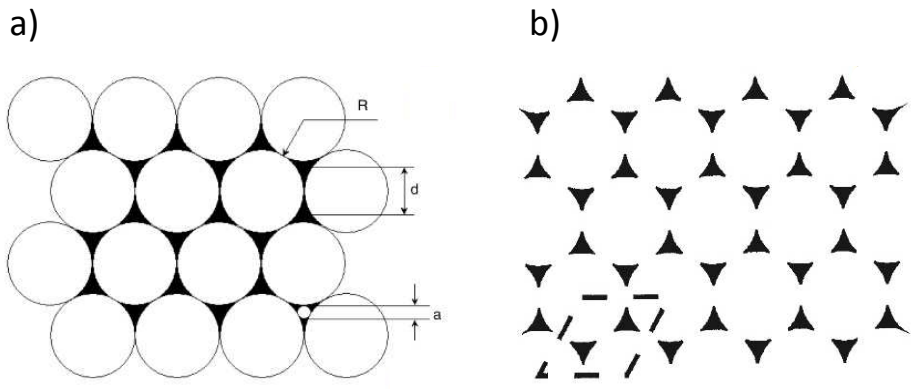

Figure 3.1: a) Representation of an hexagonal monolayer of spheres of radius R; b) Hexagonal array of prisms with a triangular base.

This is the common strategy to obtain NPA, but starting by a two-dimensional ML it is possibile to synthesize a wide range of nanoparticles arrays (which have dimensions in the range 20-1000 nm) such as opening semi nanoshells [64], nanopillars [65], nanowires [66], nanoholes [67]. In this thesis we synthesize three different nanoarrays by NSL. All the samples are based on noble metals, which are in form of mono elemental metal, alloy or multilayer.

The samples can be subdivided in three categories:

- **Au:Ag alloy Semi-NanoShell Array (SNSA)**;
- **Ag NanoPrism Array (NPA)**;
- **Ti-Ag-Au NanoHole Array (NHA)**.

In this chapter the synthesis techniques used are briefly described and in particular the morphological properties of the samples are discussed.

Characterization techniques

The morphological properties of the samples were investigated with Field-Emission Scanning Electron Microscopy (FE-SEM) and Atomic Force Microscopy (AFM). The FE-SEM microscope utilized is a Zeiss SIGMA HD that can operate in the $0.2 \div 30$ kV range, with a spatial resolution of about 1.2 nm at 30 kV. It is equipped with a detector for energy dispersive X-ray analysis (EDX by Oxford Instrument) used for compositional analysis. Measurements were performed at 5 kV for imaging in in-lens mode and at 10 kV for micro-analysis. AFM measurements were performed using a NT-MDT Solver PRO-M microscope with a 100 x 100 μm scanner. UV-VIS optical absorption characterizations were done by a JASCO V670 spectrophotometer in the 300-2500 nm wavelength range.

3.1.2 Self-assembling of Polystyrene nanoparticles

The first step of any synthesis process based on Nanosphere Lithography (NSL) is the self-assembling of monodisperse Polystyrene nanospheres (PS) on a substrate in a close packed single layer. The nanospheres, with diameter usually ranging from 100 nm up to 1 μm, are able to auto-organize in an hexagonal close packed symmetry in which each sphere has six nearest neighbors. Through this colloidal two-dimensional mask it is possible to obtain many different kind on nanoparticles arrays. The common techniques used to deposit the monolayer on a substrate are based on drop coating or spin coating [68] processes, starting from nanoparticles as a 5 or 10 wt.% water solution. The parameters used during the coating, such as the hydrophilicity and the cleaning of the substrate, the concentration of the nanoparticle's solution, the presence of surfactants, the temperature and the humidity can strongly influence the quality of the monolayer obtained, which can have structural defects like dislocations or vacancies. The process used in this thesis is based on a PS self-assembly at the interface between two liquids phases which allows to produce monolayers up to few cm^2 quite ordered on a solid substrate. [69] This is a modified version of a dip coater method. The monolayer formation is based on the following steps:

1. 20 μL of a solution PS suspension:isopropyl alcohol (50:50 % in volume) is spread on a Soda Lime Glass (SLG) substrate 2 x 2 cm^2 previously cleaned with an acid piranha

solution;

2. this substrate, inclined with a certain angle, is immersed into a glass vessel filled with Milli-Q water (18.2MΩ/cm resistivity) using a motorized system which assures an uniform velocity during the immersion;
3. PS nanoparticles form a monolayer on the water surface thanks to the capillary forces at the meniscus between the alcoholic suspension and the water;
4. the first substrate is automatically moved up outside the vessel and another cleaned substrate is manually immersed into the vessel to collect the resulting compact monolayer which floats on the water surface;
5. the samples is dried at room temperature.

In this study we used PS nanoparticles of 248 ± 9 nm (wt. 5%), 315 ± 9 nm (wt. 10%), 470 ± 12 nm (wt. 10%), 522 ± 12 nm (wt. 5%), 1030 ± 30 nm (wt. 10%) purchased from Microparticles GmbH (Germany). Isopropyl alcohol with purity ≥ 99.7 % was purchased from Sigma-Aldrich. The monolayers quality was investigated by morphological measurements (AFM and SEM) and by optical transmission spectra. The PS diameter was checked by FFT analysis on AFM and SEM images of the monolayer deposited on a silicon substrate. By FFT we have obtained a diameter of 241 ± 10 nm for nanospheres with certified diameter ($D_{cert.}$) 248 ± 9 nm and 514 ± 10 nm for $D_{cert.}$ 522 ± 12 nm. The substrates used were based on SLG, highly-pure HSQ 300 silica (SiO_2) or monocristalline silicon (Si).

PS nanospheres with diameter around 500 nm allow to obtain two-dimensional masks

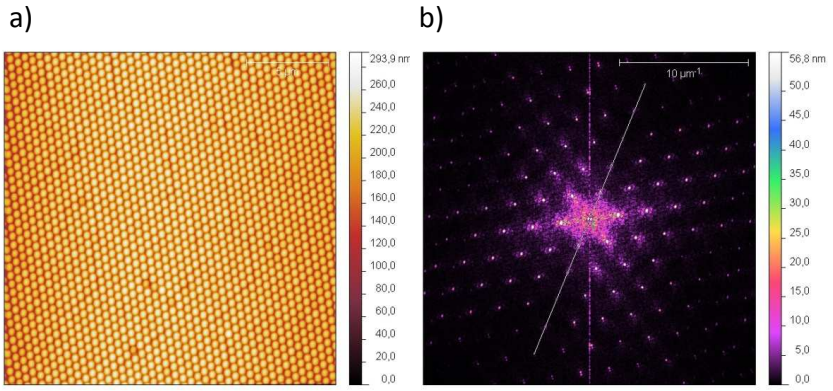

Figure 3.2: a) AFM image 20 x 20 μm^2 of a PS monolayer with certified Diameter (D) 522 ± 12 nm. b) Fast Fourier Transform of the AFM image in figure a, the white line was used to measure the distance between 10 spots and to extract the real diameter of the nanospheres.

of high quality, as can be seen in AFM image in figure 3.2. The hexagonal periodicity of

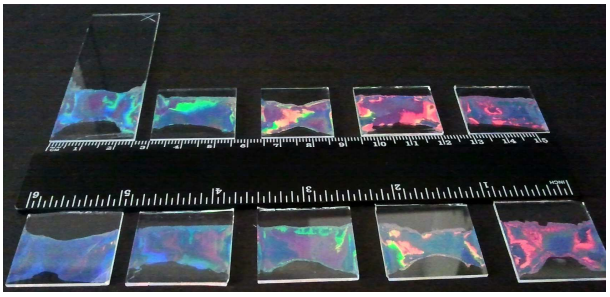

Figure 3.3: Photograph of 10 PS monolayers ($D_{cert.}$ = 522 ± 12 nm) deposited on SLG substrates.

nanospheres with diameter 522 nm arises in a fascinating iridescence of the samples, as can be seen in figure 3.3.

3.1.3 Substrate pre-cleaning

Before the synthesis of the monolayer the substrate was cleaned in a piranha solution (3:1 by volume of 30% H_2O_2 and 98% H_2SO_4) for 1 hour at 90 °C and then washed with ultra-pure milli-Q water. Sulfuric Acid and Hydrogen Peroxide were purchased from Sigma-Aldrich. The cleaning process of the substrates is very important and piranha solution is the best candidate for two reasons: (i) it is a strong oxidizer mixture and it efficiently removes organic matter from the substrates; (ii) the process hydroxylates the surfaces making them extremely hydrophilic. An hydrophilic substrate is necessary for the self-assembling process, because the PS nanospheres are in aqueous solution.

3.1.4 Optical characterization of the PS monolayer (ML)

Absorbance spectra of the PS monolayers self-assembled on transparent substrates were acquired by a Jasco V-670 double-beam spectrophotometer in the wavelength range 300-1500 nm. In our group we are able to synthesize PS monolayers using nanospheres with diameter in the range 248-1030 nm. As shown in figure 3.4 the absorbance peaks appears at lower wavelengths with the decrease of the nanospheres diameter. The peak width, in particular for diameter from 522 to 1030 nm, can be associated to the order degree of the monolayer. A narrow peak indicates an high hexagonal order. The relation between the maximum of the major peak in the absorbance spectrum and the nanosphere's diameter is linear, as presented in the graph in figure 3.5 (a) and in table (b). The error associated to λ_{mask} is the standard deviation of 10 measurements of samples with the same diameter.

The slope obtained is 1.19 ± 0.02 while the intercept is 20 ± 12 nm. This optical property is very useful also to characterize the monolayers after reactive ion etching treatment. In particular we use it to verify the homogeneity of one etching treatment on many samples which are positioned in different zones of the sample holder.

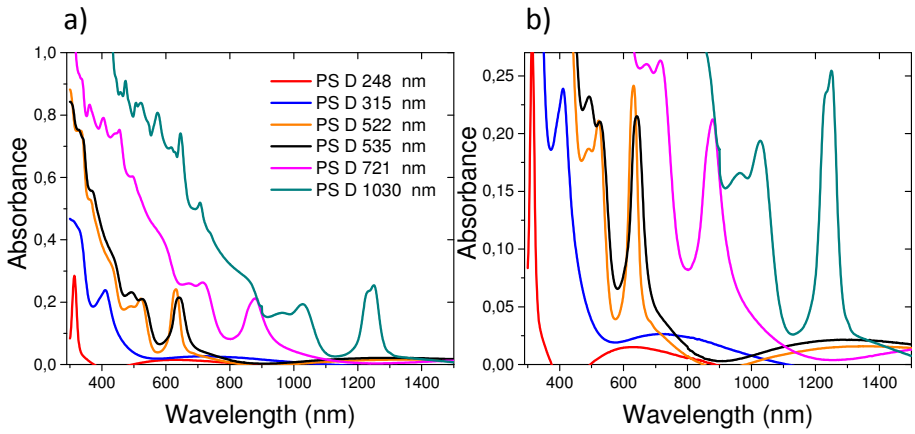

Figure 3.4: a) Absorbance spectra of the PS masks obtained with nanospheres of different diameter (D); b) zoom of graph in figure a.

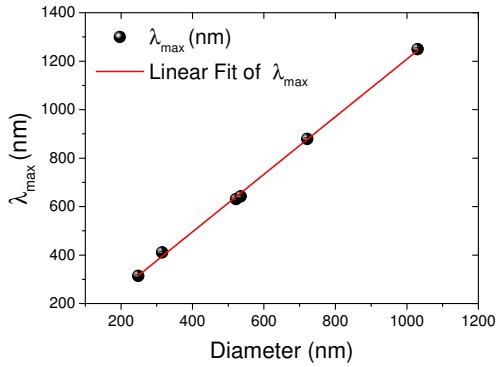

(a)

DIAMETER (D) (nm)	λ_{max} (nm)	σ (nm)
248	314	5
315	411	5
522	631	5
535	642	5
721	879	5
1030	1250	5

(b)

Figure 3.5: λ_{max} of the absorbance spectra of PS monolayer as a function of the diameter (D). Linear fit of λ_{max}.

3.1.5 Reactive Ion Etching (RIE) of PS monolayers

When the nanoarray synthesis aims to obtaining structures like SNSA or NHA an additional step is needed before metal deposition. This is a Reactive Ion Etching (RIE) treatment. It was used to dry etch the polystyrene before the metal deposition. In this way we reduced the diameter of the PS nanospheres preserving the hexagonal periodicity of the

monolayer. [70] By using RIE we have realized nanoarrays different from the standard NanoPrisms Array (NPA) obtained by NSL. Altering the nanospheres dimensions we obtained a non-close packed array and starting from it we synthesized Semi-NanoShell Array (SNSA) or NanoHoles Array (NHA).

3.1.6 RIE technique

An etching process is used to remove matter from a substrate in micro- and nano-fabrication, and can be divided in two main categories: wet etching and dry etching. The wet etching uses liquid etchants and it is based on chemical processes, while dry etching uses a high energy plasma and it is based on a combination of chemical and physical processes. Chemical etching is more selective and isotropic, while physical etching is less selective and more anisotropic. We use a Reactive Ion Etching which is a ion-assisted dry etching based on a combination of chemical and physical processes. The apparatus is usually a parallel plate system based on a cylindrical vacuum chamber with a wafer platter at the bottom of it. The chamber is grounded while the wafer platter is electrically isolated. On the top of the chamber there are small inlets for the gas entering. Volatile by-products are removed by a vacuum pump. The high-energy ions, which constitute the plasma, are generated by a radio-frequency electromagnetic field, which ionizes the gas molecules. Because of the large voltage difference, positive ions tend to drift toward the wafer platter, where they collide with the samples to be etched. In our case we used a gas mixture based

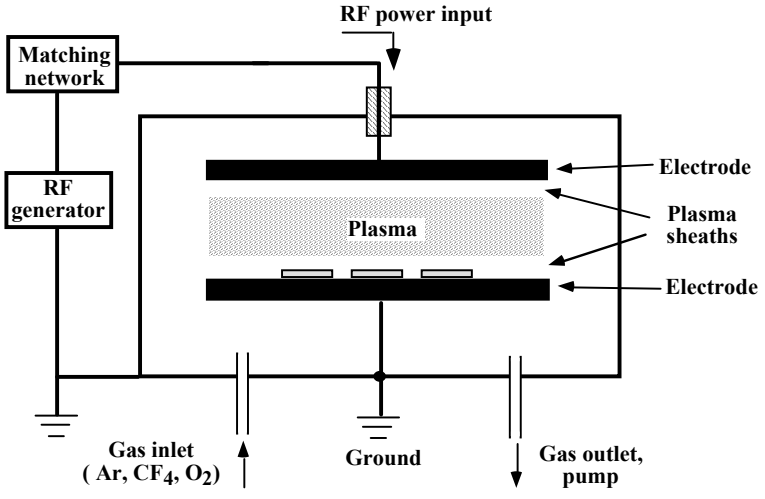

Figure 3.6: Representation of the RIE apparatus.

on Argon (Ar) and Oxygen (O_2) to generate the plasma. The chemical etching of PS is due to oxygen ions, while Ar^+ ions remove the polymer transferring part of their kinetic energy, as a sputtering process. For this reason the etching type and the final morphology of the PS nano-particles depend not only on the gas type, but also on their ratio and on the total pressure in chamber. So, we have exploited some effects of these parameters on the morphological properties of our samples.

3.1.7 RIE calibration curve

In order to finely control the morphology and the nanometric dimensions of our samples we have to investigate in details the effects of each process. In the case of RIE we know that it is strongly affected by the gas mixture, the gas flow, the total pressure in chamber and the power of the radio frequency electromagnetic field. In this work we have used a gas flow in the range 1-6.5 sccm for Ar and 1-13 sccm for O_2; the base pressure in chamber is in a range of 4-10 $\times$ 10^{-6} mbar and the radio-frequency field is applied at a power of 12-40 W. For a defined set of parameters, the etching rate depends also on the initial diameter of the PS nanospheres. This is partially due to the anisotropy of the RIE process, which slightly changes the shape of the nanoparticles form spheres to lens-like nanoparticles. So, we have measured the etching rate for each specific D (315, 522, 1030 nm), by changing only the etching time (t_{RIE}).
The final projected diameter of the nanospheres for each t_{RIE} was measured with SEM. To this aim, the PS monolayers were self-assembled on silicon substrates and not on SLG or silica, to avoid charge accumulation during SEM analysis. The program used for the analysis of SEM images is ImageJ.
By increasing the etching time we reduce the PS diameter (see figure 3.7) and in the same time we alter the shape and the roughness of the PS particles. The increased roughness is more evident for t_{RIE} from 12' to 15' in the case of initial diameter 522 nm.. The typical etching parameters used to etch monolayers of PS 522 nm are reported in table 3.1.

The etching rate can be obtained by the calibration curves, which are represented by ΔD as a function of t_{RIE}. The error bar reported is the standard deviation obtained from the measure of 50 final diameters. The curve fitting used is a parabolic function $y(x) = bx+cx^2$ and the parameters obtained are presented in table 3.2. The etching rate measured are used to have a good control on the structural properties of our samples, in order to finely

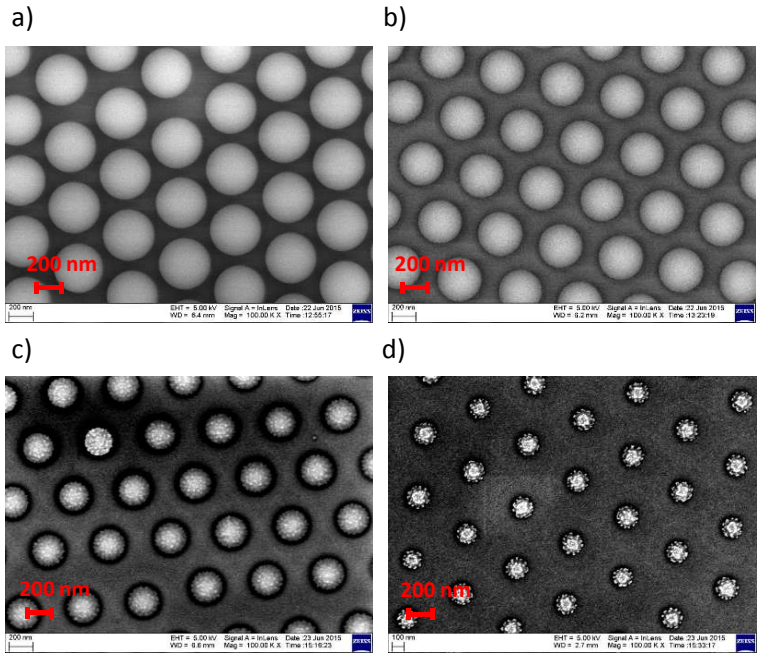

Figure 3.7: SEM analysis at magnification 100.00 KX of PS monolayers 522 nm after RIE treatment: a) 6'; b) 9'; c) 12'd) 15'.

D1 (nm)	D2 (nm)	Flow Ar (sccm)	Flow O_2 (sccm)	P (mbar)	Time (min.)
522	417	1.2	3.7	0.009	6
522	349	1.2	3.7	0.009	9
522	252	1.2	3.7	0.009	12

Table 3.1: Parameters used for RIE treatments on PS monolayers of 522 nm.

tune the optical properties in the range vis-NIR.

PS D (nm)	b $\pm$ σ (nm/min)	c $\pm$ σ (nm/min^2)
315	8.2 $\pm$ 1.7	0.8 $\pm$ 0.2
522	11.6 $\pm$ 1.6	0.9 $\pm$ 0.1
1030	22.6 $\pm$ 1.4	1.3 $\pm$ 0.1

Table 3.2: The parameters obtained from the parabolic fit of ΔD in function of the etching time, for monolayer with different diameter.

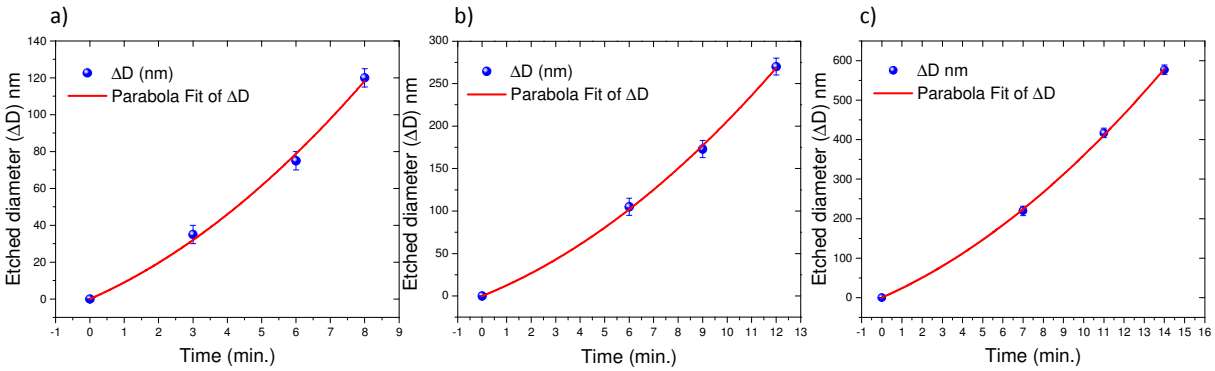

Figure 3.8: Diameter variation (ΔD) in function of the etching time (minutes) for monolayers of PS 315 nm (figure a),PS 522 nm (figure b) and PS 1030 nm (figure c) fitted with a parabolic function.

3.1.8 Effect of the total pressure on the etched PS shape

Dry etching is usually anisotropic with respect to the wet etching. It is preferentially directed along the normal to the sample's surface; in our case each PS sphere is etched from the top to the bottom, resulting in a final lens-like shape. We have verified that this effect is more pronounced in the case of a total low pressure of Argon and Oxygen (85 $\times$ 10^{-4} mbar). We have exploited for the same etching time and gas ratio, two different conditions of total pressure, low pressure (85 $\times$ 10^{-4} mbar) and high pressure (3706 $\times$ 10^{-4} mbar). The results of this test are presented in figure 3.9, in which we report the SEM analysis in cross section of a PS monolayer with initial diameter 248 nm, etched for 3 minutes at high pressure 3706$\times 10^{-4}$ mbar (figure a) and low pressure 85$\times 10^{-4}$ mbar (figure b). For the synthesis of nano-holes arrays the low pressure condition is preferred to obtain a more defined geometry of the nano holes.

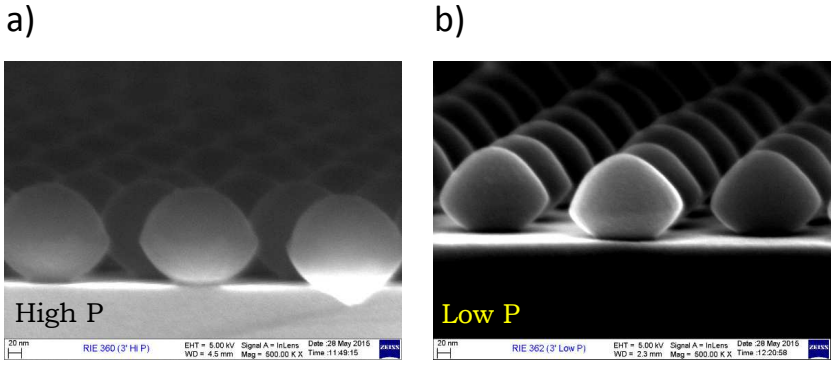

Figure 3.9: SEM image at 500.00 KX in cross-view of etched Polystyrene monolayers deposited on a silicon substrate (initial diameter 248 nm): a) 3' of etching at high pressure (3706·10^{-4} mbar) b) 3' of etching at high pressure (85·10^{-4} mbar).

3.1.9 Metals deposition: Magnetron Sputtering and Thermal Evaporation

To synthesize Au/Ag nano arrays we used two different techniques to deposit metal thin films on the etched or not etched PS monolayers. For the synthesis of Au:Ag SNSA and Ti-Ag-Au NHA we used the magnetron sputtering process, while for the synthesis of Ag NPA we used thermal evaporation. The magnetron sputtering and thermal evaporation belong to the family of physical vapor depositions (PVD). These techniques are based on physical processes which allow to deposit films of 10-100 nm with a very fine control on the thickness. We can deposit gold, silver, titanium and silica with magnetron sputtering in multilayer or alloy composition, while with thermal evaporation we deposit gold or silver in mono-elemental layer. The metal depositions to obtain nanoprisms arrays were performed by thermal evaporation for the higher collimation of the atoms flux. This allow to obtain a well defined geometry of the prisms with respect to the magnetron sputtering. In the case of SNSA and NHA the alloy or multilayer deposition is more difficult with thermal evaporation because different materials have different melting temperature and vaporization rates. So, to synthesize these classes of samples we used the magnetron sputtering. Titanium and chromium are usually used as adhesion layers because their affinity for silica and silicon is higher than that of gold and silver. The presence of titanium is particularly important for the samples which will be exposed to solution of biological molecules.

3.1.10 Magnetron Sputtering

Sputtering is a physical process in which a plasma of positive ions is used to remove atoms from a target (a metal or insulator) and deposit them on a substrate. The typical DC sputtering system is based on a target, which acts as the cathode of a diode while the substrate acts as the anode. The target and the substrate are in a vacuum chamber, and a voltage is applied between them. The sputtering chamber, in which there are the target and the substrate, is in vacuum conditions with a base pressure of 2×10^{-6} mbar. In these conditions is injected an inert and heavy gas, usually Argon, to reach a pressure of 5×10^{-3} mbar. The gas has to be inert to avoid chemical reactions and sample's contamination. To create the plasma a voltage is applied between the cathode and anode. Positive ions of the inert gas (Ar^+) are accelerated on the target bombarding it. Atoms from the target are sputtered off and deposited on the substrate. The magnetron sputtering was developed

to increase the efficiency of the DC sputtering using a series of magnets mounted below the target. The magnetic field increase the plasma density confining the electrons in a region near the target. A representation of the magnetron sputtering process is reported in graph a in figure 3.10. To sputter metals like gold, silver ,titanium a DC power source can be used, while for insulators (e.g. SiO_2, Al_2O_3, ZnO) it is necessary the use of a radio-frequency (RF) power source.

3.1.11 Thermal Evaporation

Thermal evaporation is based on the heating of a material (target) to be deposited until its evaporation. The target is in a heated container called crucible and the heating is done by the flow of electric current through it by Joule effect. Low pressure is necessary because the atoms mean free path has to be longer than the distance between the target and the substrate. In our depositions we use a pressure of 5×10^{-5} mbar. When the target reaches its evaporation temperature the atoms leave the surface and travel until they reach the substrate. The substrate is at lower temperature and the atoms transfer their energy and condense on its surface. Metals with low melting temperature can be easily deposited, such as pure gold (T_{fusion} 1063°), pure silver (T_{fusion} 961°) or alluminium (T_{fusion} 660°). To measure the deposited metal thickness we use a Quartz Crystal Microbalance (QCM), previously calibrated. QCM is a piezoelectric device, which has a precise oscillation frequency; as the metal thin layer is deposited on the QCM the mass changes producing a variation of the oscillation frequency.

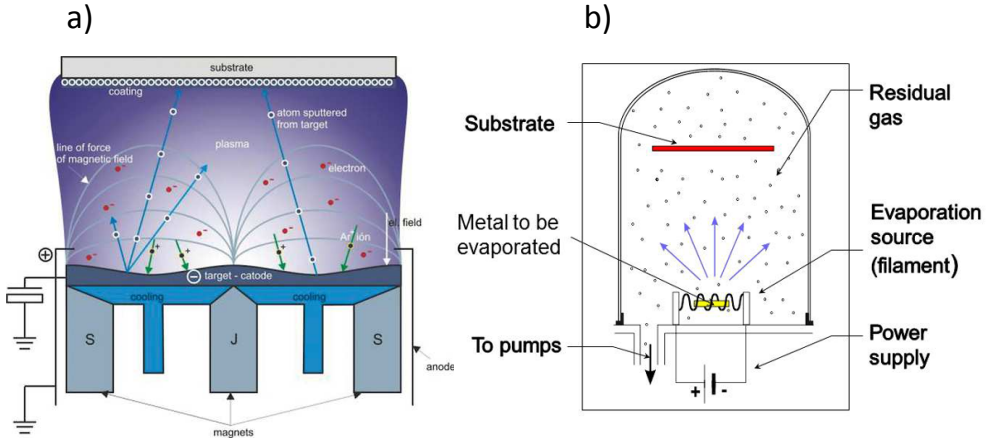

Figure 3.10: Schematic representation of the metal deposition techniques: a) The magnetron sputtering process; b) vacuum thermal evaporation apparatus.

3.1.12 Removal of the PS monolayer

To produce NPA and NHA we finally need to remove the polystyrene monolayer after the metals deposition. In the case of Ti-Ag-Au NHA we used a treatment in toluene for 3 minutes in an ultrasound bath, while for Ag NPA, which haven't the adhesion layer, we used an adhesive tape.

3.2 Au/Ag ordered nanoarrays

The previously described techniques are used for the NSL-based synthesis of the following nanoarrays:

- **Au:Ag alloy Semi-NanoShell Array (SNSA)**;
- **Ag NanoPrism Array (NPA)**;
- **Ti-Ag-Au NanoHole Array (NHA)**.

3.2.1 Semi-nanoshell array (SNSA)

The synthesis process of SNSA can be summarized in three main steps. A schematic representation is reported in figure 3.11.

1. Self-assembling of a PS ML (D = 315 ± 9 nm) on a transparent substrate;
2. Reactive ion etching to reduce the diameter of the PS nanospheres;
3. Magnetron sputtering co-deposition of a thin Au:Ag alloy over the etched nanospheres.

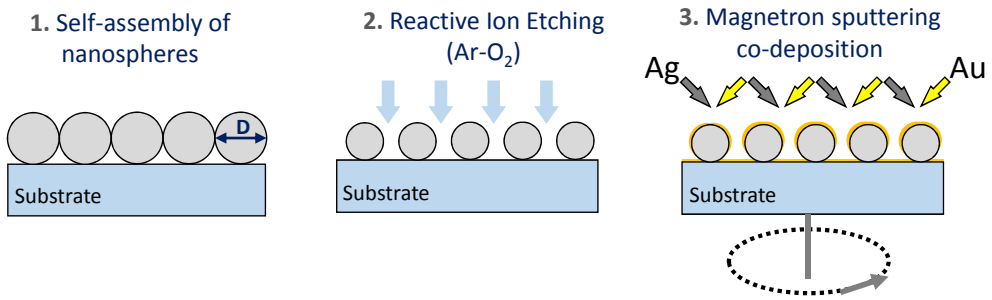

Figure 3.11: Schematic diagram of the synthesis process of Au:Ag SNSs arrays: 1) self-assembly of a PS nanospheres mask on a soda-lime glass (SLG) substrate, 2) reduction of PS nanospheres diameter by reactive ion etching, 3) co-deposition of Ag and Au by magnetron co-sputtering.

SNSA morphology and composition

The final structure of the synthesized samples is an hexagonal array of SNS nanounits. Each nanounit, the semi-nanoshell, is made by a coverage of Au:Ag alloy on top of a RIE-etched polystyrene nanosphere. For the SNSA synthesis we used commercial PS nanospheres (micro-Particles GmbH) with diameter D = 315 ± 9 nm, in aqueous solution at 5%. After the monolayer formation, we used a RIE process to reduce the diameter of the nanospheres without altering the array periodicity. RIE treatments were done in an Ar-O_2 atmosphere (60 % Ar and 40 % O_2) at a total pressure of 4 x 10^{-2} mbar. The RIE was done for different time intervals to control the gap size between adjacent SNSs. The RIE process of PS nanospheres is anisotropic because the etching is directed along the normal to the nanospheres plane.
Therefore, their final shape is not a sphere but is more similar to a lens, as showed in SEM images in figure 3.13.
The bimetallic film was then deposited on the etched mask by a magnetron co-sputtering. Au and Ag depositions were performed at the same time by using two sources, with the same inclination (15 degrees) with respect to normal direction of the samples surface, using a rotating sample-holder.
A typical morphology of the SNSA is presented before and after the metals deposition in the SEM analysis in figure 3.12.

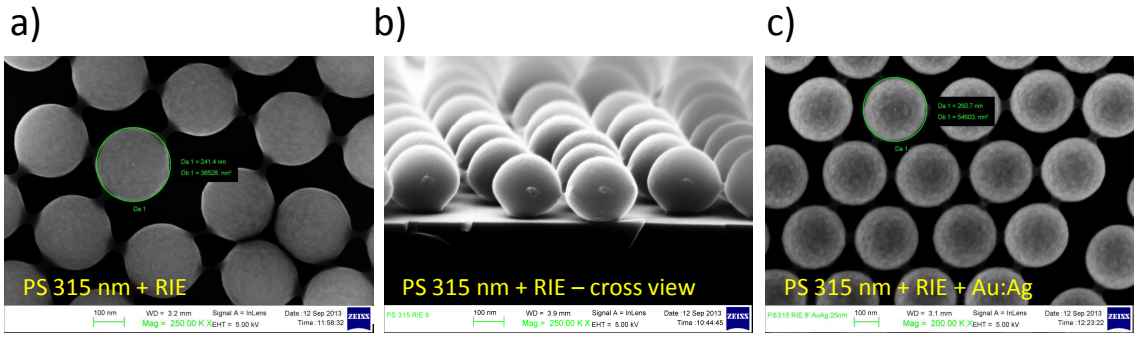

Figure 3.12: a)SEM image 250.00 KX of etched PS nanospheres (top view); b) SEM image at 250.00 KX of etched PS (cross view); c) SEM image 200.00 KX of etched PS nanospheres covered by an Au:Ag nanometric layer (thickness about 30 nm).

The composition of the metal coverage was checked by EDX spectroscopy, which resulted in atomic concentrations of 47% of Ag and 53% of Au respectively, as reported in figure 3.14.

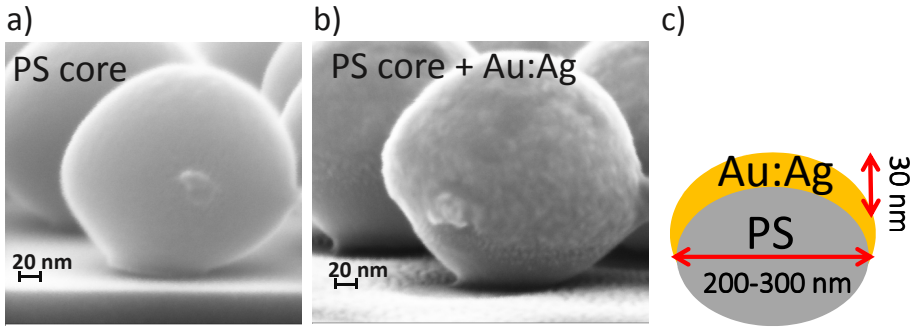

Figure 3.13: a) SEM image at 750.00 KX magnification of etched PS nanoparticles; b) SEM image at 750.00 KX magnification of etched PS nanoparticles covered by an Au:Ag nanometric layer (thickness about 30 nm).

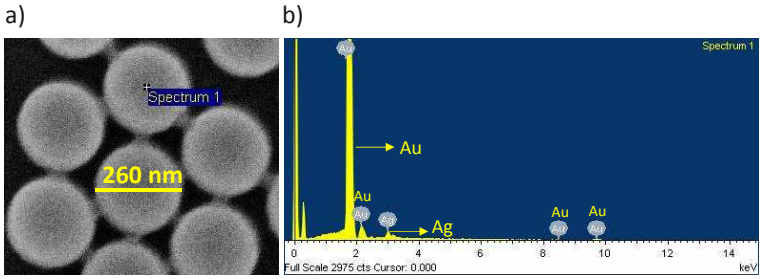

Figure 3.14: a) SEM image of SNSA (HI-SNSA) b) EDX analysis which refers to a central point of the SNS (indicated by the cursor "'Spectrum 1"') and shows an atomic concentration of 53 % of Ag and 47 % of Au.

The EDX analysis confirmed the homogeneity of the Au:Ag alloy composition on the SNS surface. The advantage of working with a bimetallic alloy with respect to the monoelemental case is due to the better chemical stability of Au and to the enhanced plasmonic properties of Ag.

3.2.2 Nanoprisms array (NPA)

The synthesis of Ag NPA can be subdivided in the following steps as sketched in figure 3.15.

1. Self-assembling of a PS ML on a transparent substrate (D 470/496/522 ± 12 nm);
2. Vacuum thermal evaporation of Ag (film thickness 50-100 nm);
3. Removal of the PS ML by an adhesive tape.

In this case we used PS nanoparticles from 470 to 522 nm in diameter and we deposited a silver layer by thermal evaporation on the PS masks. The metal was deposited on the substrate only in the interstices among the nanospheres; after the removal of the mask the

Ag NPA was obtained. In this nanoarray the functional nanounit is a silver triangular nanoprism with a lateral size that depends on the polystyrene diameter (0.233·D). The height of the nanoprisms is controlled by the height of the deposited metal film. The morphology of a typical Ag NPA is shown in the SEM e AFM images in figure 3.16. In this case the lateral size of the nanoprism is 122 ± 5 nm and the height is 50 ± 5 nm.

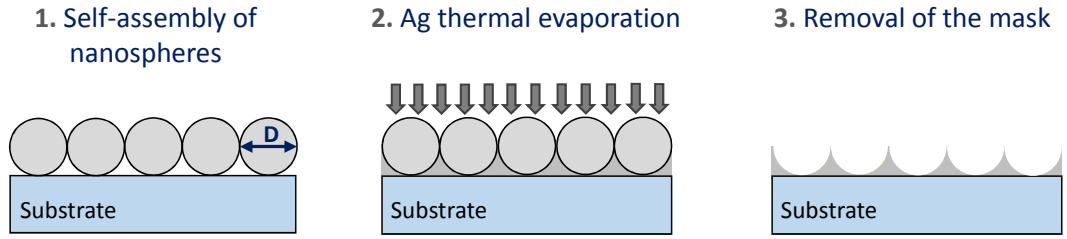

Figure 3.15: Schematic diagram of the synthesis process of Ag NPA: 1) self-assembly of a PS nanospheres mask on a soda-lime glass (SLG) substrate, 2) Ag thermal evaporation; 3) removal of the PS mask by a tape.

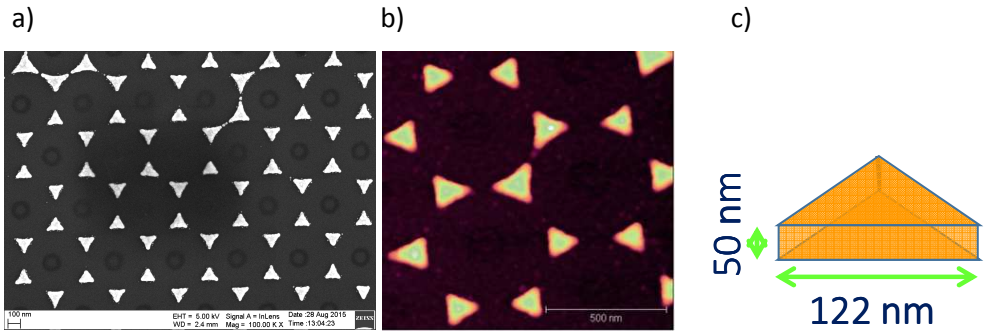

Figure 3.16: a) SEM image at 100.00 KX of Ag NPA; b) AFM images 1.3 x 1.3 μm^2 of Ag NPA; c) representation of the typical nanoprism dimensions (D = 522 nm).

3.2.3 Nanoholes array (NHA)

The synthesis of nanoholes array was based on the following steps:

1. Self-assembling of a PS mask on a transparent substrate (D = 522 ± 12 nm);
2. Reactive Ion Etching to reduce the nanosphere's diameter;
3. Multilayer deposition of Ti, Ag and Au by magnetron sputtering;
4. Removal of the mask by treatment in toluene in ultrasound bath.

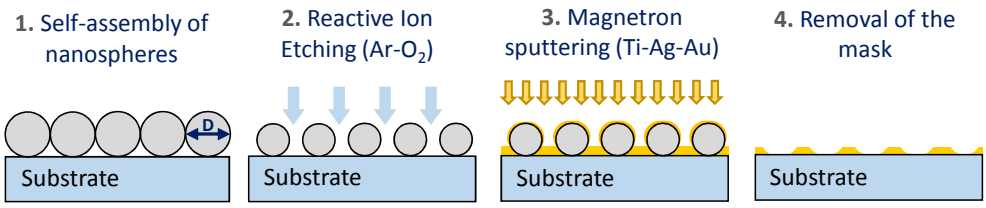

Figure 3.17: Schematic diagram of the synthesis process of Ti-Ag-Au NHA: 1) self-assembly of a PS nanospheres mask on a transparent substrate; 2) reactive ion etching to reduce the PS diameter; 3) multilayer deposition of Ti, Ag and Au; 4) removal of the PS mask by toluene in ultrasounds.

Nano-holes arrays were synthesized starting by the self assembling of Polystyrene nanospheres of 522 ± 12 nm in diameter on a silica (SiO_2) substrate, previously cleaned and hydroxylated with a piranha solution. The reactive ion etching treatment in Ar and O_2 was done for 10 minutes with a total pressure of 9×10^{-3} mbar. The etched masks, with a diameter of 300 ± 10 nm, were covered by a multilayer of titanium, silver and gold. The multilayer deposition of titanium (Ti) 5 nm, silver (Ag) 45 nm and gold (Au) 10 nm was performed with magnetron sputtering, to obtain a total metal thickness of 60 nm. The multilayer thickness was measured with Atomic Force Microscopy and Scanning Electron Microscopy. Titanium was used as an adhesion layer, the silver for its intrinsic best plasmonic performances with respect to gold, and gold was used to have a surface structure chemically more stable. The typical morphology of a Ti-Ag-Au nanoholes array can be seen in SEM images in figure3.18, which is reports a side view (figure a) and a top view (figure b,c) of a typical sample.

3.2.4 Nanoarrays: optical properties and applications

Au:Ag SNSA and Ag NPA are characterized by a LSPR peak in the visible-near infrared region of the electromagnetic spectrum. The plasmonic properties of Ti-Ag-Au NHA are

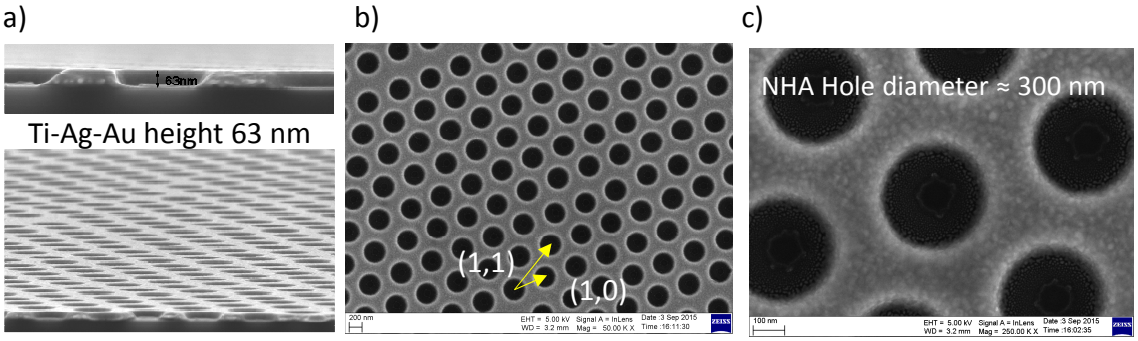

Figure 3.18: SEM analysis of a NHA with an hole diameter of 300 nm and a total metal height of 63 nm: a) side view; b) top view at 50.00 KX; c) top view at 250.00 KX.

exploited in the Extraordinary Optical Transmission (EOT) peak in the NIR region. The plasmonic optical properties of these nano arrays will be extensively discussed in the following chapters. SNSA, NPA and NHA were functionalized with biological molecules to investigate their plasmonic biosensing performances. The samples were functionalized using the same biofunctionalization strategy in order to compare their sensitivity and to study the advantages and disadvantages in the use of one system with respect to another, for a typical couple of receptor-ligand molecules. Ag NPA are also studied as Surface Enhancement Raman Spectroscopy (SERS) substrates in function of Ag oxidation, as discussed in the last chapter.

3.3 Van Duyne's biofunctionalization protocol

To test the efficiency of the proposed system as a biosensor, we used an established protocol for the detection of tiny biomolecules, based on the receptor-ligand approach and using biotin-streptavidin model system. This couple of biological molecules is composed by biotin, which is the receptor (or also called the biorecognition element), and streptavidin (SA) which is the analyte. Biotin and streptavidin are able to bind with a very strong and specific interaction due to their intrinsic structural properties. [71, 72] This feature makes them the best candidates to study the biomolecular recognition events on the substrates. To immobilize these molecules on the nanoarrays we have followed the Van Duyne's protocol. [73] This protocol is based on three main steps: (i) at first a Self Assembled Monolayer (SAM) of two different thiols is immobilized on the sample's surface (one is the spacer, the other provides the functional group to bind biotin); (ii) then the biotin is bound on this

SAM by a crosslinking reaction (iii) at last, the sensor is exposed to different streptavidin concentrations to test the specificity and the sensitivity of the nanostructures.
This biofunctionalization strategy is sketched in figure 3.19.

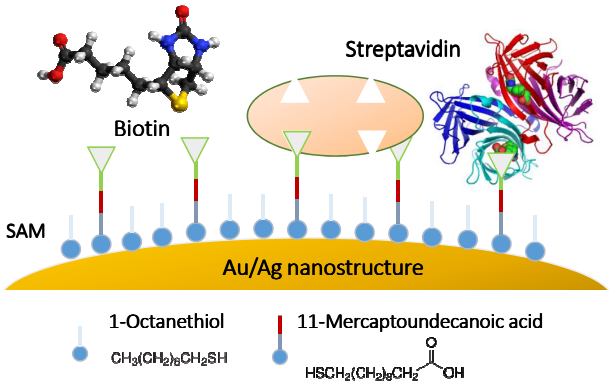

Figure 3.19: Schematic illustration of the Au/Ag nanostructure's bio-functionalization protocol (not to scale).

3.3.1 Self assembled monolayers of thiols

The most common and successful strategy to immobilize molecules on Au/Ag substrates is the use of alkanethiols ($HS(CH_2)_nX$). The alkanethiols are characterized by an "anchoring group", the sulphur atom (S), and by a head group, which is indicated in the linear formula as X. These molecules are able to spontaneously adsorb from solution onto the substrate by the covalent bond between S-Ag or S-Au. The result of this spontaneous binding is the formation of a very ordered monolayer in which the "anchoring group" is strongly bound to the substrate. The $-CH_2-$ chains interact by Van der Waals forces, and the head group is exposed at the interface with the air or with a liquid. The reaction between this functional group (-X) and other molecules allows to bind them to the metal surface. The rate of the self assembling process is strongly affected by the solvent, the thiol's concentration and length, the temperature and the presence of impurities onto the substrate. The best solvent for the thiol's solution is ethanol for its low tendency to be incorporated into the monolayer. Moreover, it can be bought with high purity and it is not so much expensive. Following the Van Duyne's protocol the SAM of thiols is formed by 1-Octanethiol (1-OCT) and 11-Mercaptoundecanoic Acid (11-MUA) in total concentration 1 mM and in a 3:1 ratio in ethanol solution. [73] These two thiols differ in the length of the alkyl-chain and for the

presence of a functional group in 11-MUA. The most concentrated, 1-OCT (linear formula CH_3-(CH_2)7-SH), is only a spacer and for this reason it is shorter with respect to 11-MUA. 11-MUA (linear formula HS-$(CH_2)_{10}$-CO_2H) has the carboxylic group necessary to bind the receptor to the nanostructure's surface.

3.3.2 Biotin and Streptavidin

The biotin-streptavidin system is a couple of biological molecules which is characterized by a very high binding affinity. This is one of the strongest non covalent interactions found in nature. The biotin is a small vitamin (vitamin H) presents in all living cells with a Molecular Weight (MW) of 244,3 g/mol. This molecule can bind to streptavidin, a bacterial tetrameric protein with a MW of about 60.000 g/mol (4 x 15.000 g/mol) isolated from the actinobacterium Streptomyces avidinii, without altering its biological activity. [74] The streptavidin (SA) has dimensions of about 4,5 x 4,5 x 5,8 nm and a projected area of 25 nm^2. [74, 75] Four equivalent sites situated on opposite sides of the SA can bind to biotin, as sketched in figure 3.21. The strong affinity between biotin and streptavidin is expressed by the value of the affinity constant K_a which is in solution 10^{13} M^{-1} [76]. If the recognition event happens at a solid/liquid interface the K_a will be different from this value. [75] The high affinity is due to hydrogen bonds, van der Waals/hydrofobic forces, and the intrinsic advantageous conformation of the SA when the biotin binds to its side. [77] There is an-

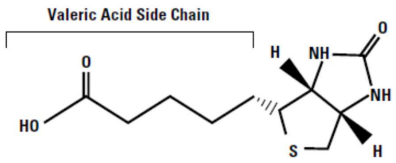

Figure 3.20: The Biotin molecule, MW 244.3 g/mol [3].

other protein, the avidin, which has the same high binding affinity for the biotin, but for its basic isoelectric point 10-10.5 and the presence of carbohydrates in its structure, the avidin has higher non-specific binding properties; this is the advantage in the use of the streptavidin. [3]

The streptavidin-avidin/biotin bond stands to many conditions of temperature, pH or organic solvents. [3] This property makes the binding of these molecules very interesting in biotechnology, such as to study the specific biorecognition events on the substrates, in par-

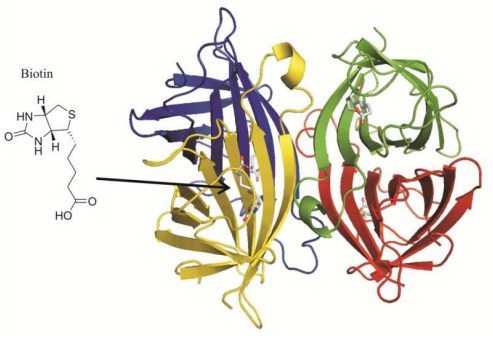

Figure 3.21: Three-dimensional model of the tetrameric structure of the Streptavidin. Each monomer is represented by a different color.

ticular to develop specific biosensors. Effectively, for the realization of biosensing devices it's necessary to study the recognition events between the ligand and the analyte when the first is forced on a substrate, because of the interaction differs from that in solution. [75] In particular, when the ligand is immobilized on a surface its orientation, concentration, the steric hyndrance of the ligand-analyte couple and the nonspecific analyte-analyte or analyte-substrate interactions can strongly influence the binding. [75] In the case of surfaces covered with the 100 % of biotinylated-molecules the binding efficiency with SA decreases, and this is probably due to the exposure of other parts of the biotin which interact non-specifically with SA. [78]

Moreover, the chemical and physical properties of the surface on which the ligand is immobilized can affect the interaction.

The principal strategy to immobilize the biotin-SA system on the substrates, is to bind biotin-alkylthiolate monolayers on gold or silver surfaces exploiting the covalent S-Au or S-Ag bond. The biotin can be linked to alkylthiolate molecules, Polyethylene Glycol (PEG), PEG-Amine, proteins, antibodies and other many kind of molecules through its valeric acid chain which can be derivatized with other groups.

Following the Van Duyne's strategy we use the Amine-PEG_2-Biotin, which is a water soluble amine-derivatized biotin molecule that can react with the carboxyl groups of the 11-MUA by a cross linking agent, the 1-Ethyl-3-[3-Dimethylaminopropyl]Carbodiimide hydrochloride (EDC).

The biotin molecules is represented in figure 3.20, while the Amine-PEG_2-Biotin in figure 3.22.

When the binding is forced on a substrate, only two sites of the protein are available

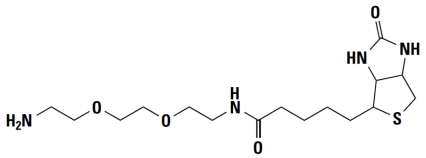

Figure 3.22: The Biotin-PEG_2-Amine molecule, MW 374.5 g/mol [3].

for the biotin. Many works reported that a complete monolayer of biotin exposed to a streptavidin solution, it's less able to bind the protein for the steric hindrance, in fact, the common strategy is to use a monolayer in which the biotin is diluited with smaller molecules. [76, 79, 80] This is an important aspect because the quantity of the adsorbed streptavidin is strongly dependent by the biotin concentration.
The Van Duyne's protocol suggests a ratio of 1:3 11-MUA:1-OCT.

3.3.3 EDC and the cross-linking reaction

The binding of the receptor (biotin) to the nanostructure's surface takes place by a cross-linking reaction between the -COOH group of the 11-MUA and the $-NH_2$ group of the Biotin-PEG_2-Amine as described above. The crosslinking reaction is used to form a covalent bond between two or more molecules, by the use of an intermediate agent (the crosslinker) that reacts with the functional groups of these molecules. To catalyze the formation of an amide bond between a carboxyl group and a primary amine we used an heterobifunctional crosslinker called carbodiimide, the EDC. In the firs step of the reaction, as represented in figure 3.24, the activation of the -COOH group by EDC forms an intermediate molecule, the O-acylisourea. This molecule is displaced by the primary amino group of the biotin by nucleophilic attack. The biotin is so bound to the 11-MUA by an amide bond, and the EDC by-product is released as a soluble isourea. The EDC is a 0Ålength spacer arm and this means that it does not become part of the final product.

EDC and the solvent effect

The presence of salts and so of the ionic molecules make the complex more stable. [77] The important thing when using the EDC is the choice of the buffer. In particular, the suitable buffer for EDC cross-linking reactions is the 2-(N-Morpholino)EthaneSulfonic acid sodium salt (MES) at acid pH 4.5-5. [3] In these conditions the reaction ends in few minutes. If

primary amines or carboxyls groups are present in the buffer, the efficiency of the reaction will be lower. In this work we used a phosphate buffer at a neutral pH, as indicated in the Van Duyne's protocol. This buffer is recommended only for the use of very high EDC concentration; in our case we use 10 mM of EDC which is higher with respect to the concentrations of molecules which have to react. [4] For lower concentration of EDC the MES is preferred. [4]

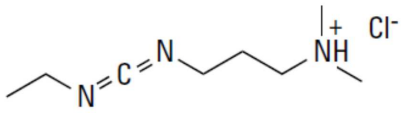

Figure 3.23: EDC, MW 191.70 g/mol Spacer arm 0Å.

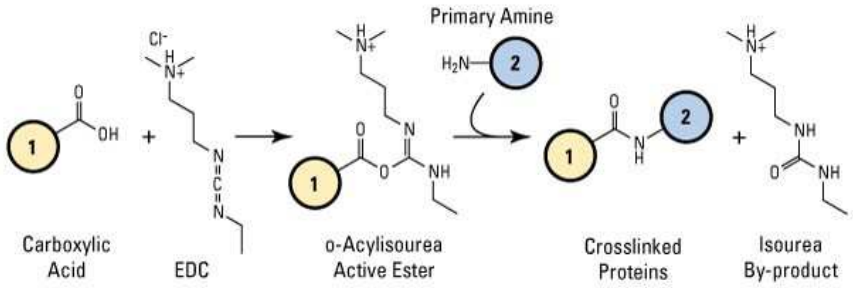

Figure 3.24: EDC crosslinking reaction scheme. Carboxyl-to-amine crosslinking with the EDC. Molecule (1) in our case is the 11-MUA and Molecule (2) is the Amine-PEG_2-Biotin. [4]

4 Semi-NanoShell Arrays as biological sensors

4.1 Introduction

The main approach to biosensing using NSL over past years has been based on the fabrication of nanoprism arrays (NPA) as optical transducers. [27] In recent years a new kind of nano-array based on gold semi-nanoshells (SNS), still obtained using NSL, was investigated as SERS substrate. [28,81]. Calculations have shown that the gaps between SNSs are very important hot spots of local field enhancement. In this work, we present a modified fabrication method of SNS arrays, in order to obtain nanostructures made by an alloy of two metals (Au-Ag in the present case). The optical properties of Au:Ag alloy SNS arrays obtained by NSL are studied and, in particular, the effect of the electromagnetic coupling between them on the LSPR response for proteins detection is investigated. The advantage of working with a bimetallic alloy with respect to the monoelemental case is twofold: (i) Au has a better chemical stability; (ii) Ag has better plasmonic properties. [17,82] The attractive characteristics of the SNS arrays are the high sensitivity to refractive index changes (in particular, in close proximity of their surface), the possibility to have a good control on the structure and as a consequence on the LSPR spectral position, which can be tuned from UV to NIR region, and the stability for device applications.

4.2 Experimental section

4.2.1 Synthesis of Au:Ag SNSA

Au-Ag alloy SNS arrays (SNSA) were synthesized by Nanosphere Lithography (NSL) [27] as described in chapter 3. The process can be divided into three main steps. In the

first step, a mask of polystyrene (PS) nanospheres is self-assembled on a soda-lime glass substrate. Before the synthesis of the mask, the substrate is cleaned in a piranha solution (3:1 by volume of 30% H_2O_2 and 98% H_2SO_4) for 1 hour at 90 °C and then washed in ultra-pure milliQ water. Commercial polystyrene nanospheres (micro-Particles GmbH) with diameter D = 315 ± 9 nm were used. The second step is a Reactive Ion Etching (RIE) process performed to reduce the initial diameter of the nanospheres and thus opening gaps between them, without altering the array periodicity. RIE treatments were done in an Ar-O_2 atmosphere (60 % Ar and 40 % O_2) at a total pressure of 4×10^{-2} mbar for different time intervals to control the degree of lateral coupling. In the third step a thin bimetallic layer (equivalent to a 30 nm-thick film) is deposited on the etched nanospheres by magnetron co-sputtering. This co-deposition results in a homogeneous Au:Ag alloy layer covering the upper part of the etched PS nanosphere to form the plasmonic SNS, which constitutes the functional building block of the array, as described in chapter 3. As an example, in fig.4.1 we have reported the Scanning Electron Microscopy (SEM) images of a typical sample at different magnification. This method allows to obtain Au:Ag SNS arrays with a high degree of order up to 1 cm^2 size scale.

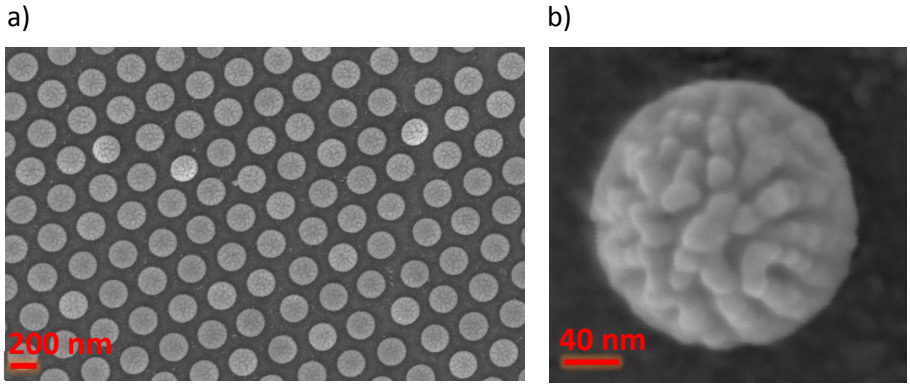

Figure 4.1: SEM image of a typical Au:Ag SNS arrays at different magnification.

Morphology of SNSA

The final structure of the synthesized samples is an hexagonal array of SNS nanounits. Each nanounit, the semi-nanoshell, is made by a coverage of Au:Ag alloy on top of a RIE-etched polystyrene nanosphere. Structural parameters of the array as shell-thickness, curvature, spacings between adjacent units and size of units, can be controlled by metal

deposition and template preparation conditions during RIE (total pressure of gas mixture, etching time and diameter of PS nanospheres).
A typical morphology of the array is illustrated in Fig. 4.1(b): in this case, SNSA were obtained with PS nanospheres with D of 315 nm, a RIE etching time of 8 minutes and a total metal thickness of about 30 nm. The resulting final gap between the SNS is about 120 nm. The RIE process of PS nanospheres is anisotropic because the etching is directed along the normal to the nanospheres plane. Therefore, their final shape is not a sphere but is more similar to a lens. The surface of SNSs presents a very interesting roughness as shown in FE-SEM image in fig.4.1(a). This morphology can be controlled by varying the Ar:O_2 ratio during the RIE process and it is a combined effect of the roughness induced on the etched nanospheres during the RIE process and of the sputtering deposition of the metals. The roughness can have beneficial effects on the development of field hot spots and on the local field enhancements at the sample surface.

Localized Surface Plasmon Resonance (LSPR) of SNSA

The optical properties of the samples can be easily tuned by changing the RIE etching time, which control the lateral coupling between the SNSs. An example of this effect is shown in fig. 4.2, which reports the far-field absorbance spectrum of the SNSA with a gap of 120 nm (blue line, RIE 8 min) and of 35 nm (black line, RIE 3 min). The wavelength of the maximum LSPR peak is $\lambda = 1212$ nm for the RIE 3' sample (black line, higher-interaction or HI sample) and it is red-shifted with respect to the one of the RIE 8' sample ($\lambda = 920$ nm, blue line, lower-interaction or LI sample), due to larger lateral coupling between neighboring SNSs. In the gap regions between adjacent nanoparticles there is a high field localization. This is due to the near-field coupling which suppresses drastically the scattering into the far field. [1] This near-field coupling between neighboring SNSs causes a red-shift of the LSPR peak. The morphological characterization of lower-interaction and higher-interaction samples is presented in SEM images in fig. 4.3.

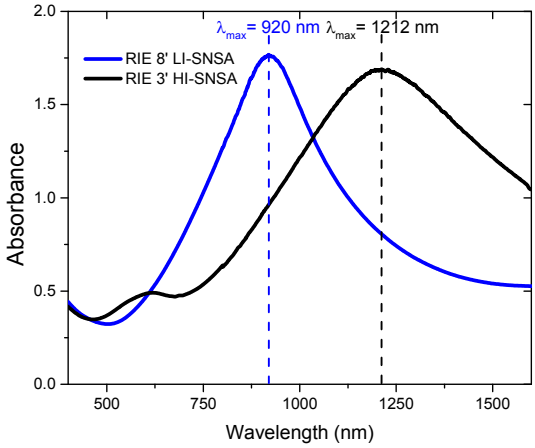

Figure 4.2: LSPR spectra for low-interaction, LI, and high-interaction, HI, Au-Ag SNS arrays: absorbance measurements of samples obtained with a RIE etching time of 8 min (blue line, LI) and 3 minutes (black line, HI),respectively.

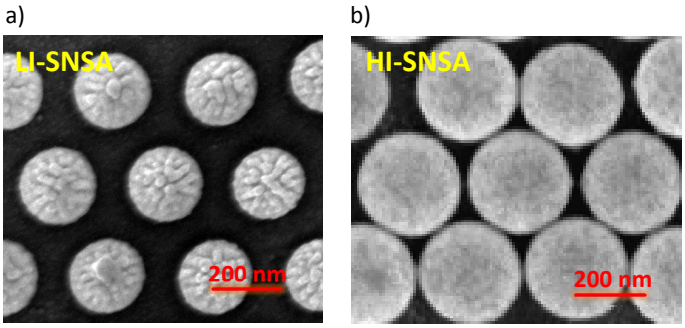

Figure 4.3: a) SEM image of a Au-Ag LI-SNSA (8' RIE); b) SEM image of a Au-Ag HI-SNSA (3' RIE)

4.2.2 Bio-functionalization protocol

As previously discussed in chapter 3 the biofunctionalization protocol was developed by Van Duyne's group for the functionalization of the NPA. [73] At first, the samples are incubated for 15 h in a thiols solution, 1 mM, of 1-Octanethiol (1-OCT):11-Mercaptoundecanoic acid (11-MUA) in 3:1 ratio in ethanol. This forms a protective self-assembled monolayer (SAM) over the SNSs. Then, samples are washed with pure ethanol and dried in vacuum for about 30 minutes. The second step is the coupling of the biomolecular receptor (Biotin-PEO_2-Amine) to the SNSs using a 1-Ethyl-3-[3-dimethylaminopropyl]carbodiimide hydrochloride (EDC) cross-linking agent. The EDC activates the carboxyl groups (-COOH) of 11-MUA to bind to the NH_2 groups of the Biotin-PEO_2-Amine, forming an amide bond between the receptor and the thiols layer. [83] For this functionalization, the samples are incubated in a solution 1 mM of Biotin-PEO_2-Amine with 10 mM of EDC in phosphate-buffered saline

(10 mM phosphate, 150 mM NaCl, pH 7.4 - PBS) for 3 h. Then, they are washed with PBS 10 mM and ultra-pure water to remove unbound molecules and dried in vacuum. Finally, for the recognition event between receptor and analyte, the samples are incubated in a solution of Streptavidin (SA) at different concentrations (10^{-13} M $\leq$ [SA] $\leq 10^{-6}$ M) in PBS 10 mM for 5 h to ensure achieving of binding equilibrium, washed with PBS and pure water and dried in a N_2 flux.
1-Octanethiol, 11-Mercaptoundecanoic acid, ethanol, PBS, EDC, Streptavidin and BSA (Albumin from bovine serum) were purchased from Sigma Aldrich while, Biotin-PEO_2-Amine, was purchased from Thermo Scientific. All reagents were used without further purification.

4.3 Results and discussion

4.3.1 Bio-functionalization and LSPR response

To study the application of the SNSA as plasmonic biosensors, the samples were functionalized with a typical receptor-ligand couple of biomolecules such as biotin-streptavidin. Streptavidin (SA) is a bacterial tetrameric protein from Streptomyces avidinii, with a molecular weight of 60 kDa. Biotin (vitamin H) is a small water soluble molecule with a molecular weight of 244.2 Da. The interaction between biotin and streptavidin is characterized in solution by a very high affinity constant ($K_a \cong 10^{13}$ M^{-1}), in particular four molecules of Biotin can bind to one molecule of streptavidin in equivalent sites, which are situated on opposite sides of the streptavidin. [71, 72] The high affinity stems from hydrophobic interactions, shape complementarity, hydrogen bonds and structural rearrangement of the protein. [72] Van Duyne's protocol is characterized by three steps of functionalization and at each step a different layer of molecules is immobilized on the surface of the samples, as described in chapter 3. The SAM of 1-OCT:11-MUA (in 3:1 ratio) forms a protective layer from non-specific interactions, and it allows to bind biotin on SNSs by a cross-linking reaction with EDC. The receptor layer is not uniform because the biotin can bind only to the 11-MUA. This is an important aspect because the interaction is influenced by the steric hindrance and by the concentration of biotinylated molecules.
At each functionalization step, additional layers of molecules are deposited on the surface,

producing a red-shift of the LSPR peak. Since upon functionalization the modification of the absorption curve is not simply a rigid shift but involves both a shift and a deformation, a simple evaluation of the maximum position can be unsatisfactory to follow the dynamic of the biorecognition. Therefore, for the analysis of the LSPR peak shift we monitored the evolution of its centroid, performing at each step an averaged weight over the absorbance of the peak abscissas above a given threshold A_{th} using the following equation:

$$\lambda_{centroid} = \frac{\sum_i \lambda_i \cdot (A_i - A_{th})}{\sum_i (A_i - A_{th})} \tag{4.1}$$

where A_i is the absorbance value at wavelength λ_i. A schematic representation of this analysis is reported in fig. 4.4, in which the threshold (dashed horizontal line) is the FWHM of the peak height. The peak height is calculated as the difference in absorbance at λ_{max} and λ_{min}.

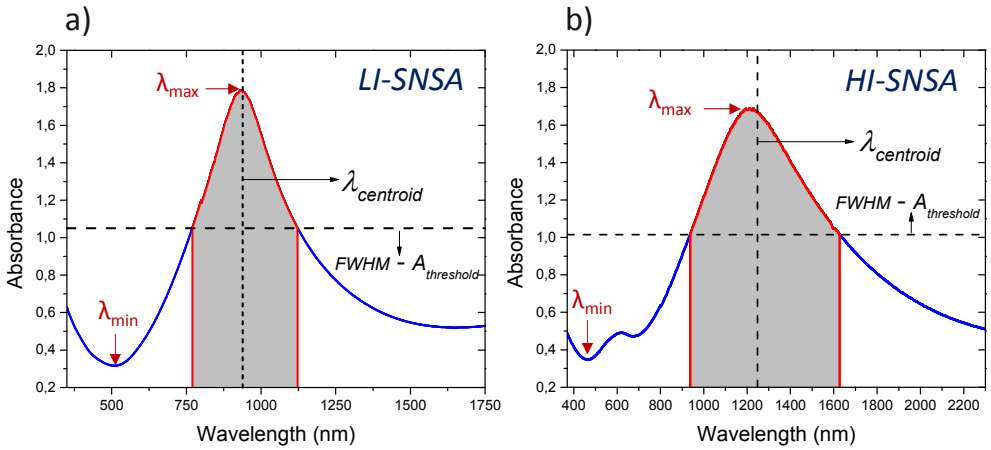

Figure 4.4: Schematic illustration of the analysis used for LSPR peaks: $\lambda_{centroid}$ (λ_c) is the centroid of the peak calculated for the part of the spectrum above the threshold A_{th}, according to Eq. 4.1; a) LSPR peak for low-interaction, LI-SNSA (RIE 8'); b) LSPR peak for high-interaction, LI-SNSA (RIE 3')

The error on the shifts has been evaluated as 3σ (σ being the standard deviation of the centroid in a set of repeated measurements), to take into account both the statistical errors and the errors due to intra-sample inhomogeneities.

The response of the LSPR sensors is controlled by the morphological and compositional characteristics of the nanoparticles used, as they define the spectral width, the decay length of the electromagnetic field and the intensity extinction of the spectrum. In this study we have investigated two sets of samples, which differ in size and gap distance

between the SNSs therefore providing a different level of interaction: in one case the SNSs exhibit a larger gap (about 120 nm) with a lower degree of interaction (sample LI): each SNS can be considered as an individual sensor to a good level of approximation. [84] In the other case, the SNSs exhibit an average gap of about 35 nm so they can be considered electromagnetically coupled with a higher degree of interaction (sample HI). The two sets of samples were functionalized with biological molecules and the LSPR response was monitored. For each step of bio-molecules incubation an incremental red-shift ($\Delta\lambda_c$) of the LSPR peak centroid was observed, as shown in fig. 4.5 for the low-interaction SNSA (LI-SNSA) and in fig. 4.6 for the high-interaction (HI-SNSA) sample.

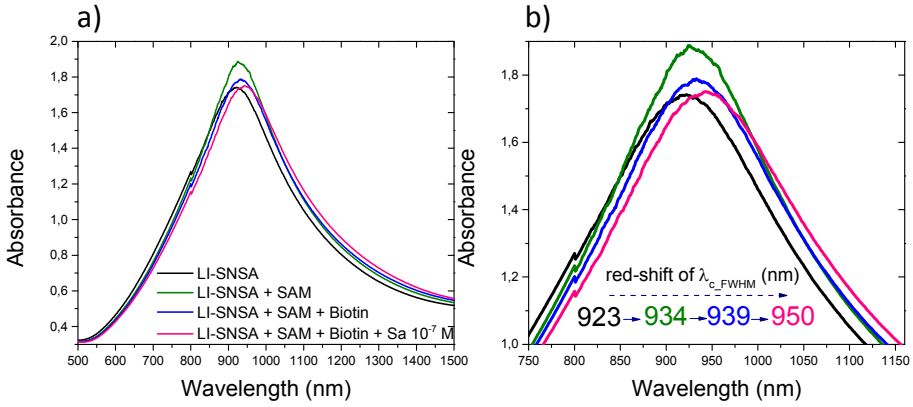

Figure 4.5: a) LSPR spectra for a sample of LI Au-Ag SNS arrays before and after functionalization with bio-molecules (the $\lambda_c$values were calculated choosing a threshold at the value of absorbance (Ath) at the 50% of the peak height): λ_c of the sample as deposited (black line) is 923 nm; λ_c after functionalization with SAM is 934 nm (green line); λ_c after functionalization with Biotin is 939 nm (blue line); λ_c after exposition of 100 nM of Streptavidin is 950 nm (pink line). b) Zoom of the LSPR spectra of figure a.

In the case of LI-SNSA at the first step of functionalization, with SAM, samples exhibit a $\Delta\lambda_c$ of +11 nm, considering a threshold at 50% of the peak height (see fig. 4.5(b)). Following the functionalization with biotin, the samples exhibited an additional red-shift of +5 nm, indicating the successful binding of the receptor. Exposure of the SNSA to 100 nM of streptavidin results in a maximum $\Delta\lambda_c$ of about +11 nm, corresponding to a saturation of SA for this density of receptors. In the case of HI-SNSA samples exhibit a $\Delta\lambda_c$ of +26 nm with SAM, an additional red-shift of +9 nm with Biotin and the exposure of the HI-SNSA to 100 nM of streptavidin results in a maximum $\Delta\lambda_c$ of about +38 nm (see figure 4.6). All of these LSPR centroid variations were measured considering a threshold at 50% of the peak height. Fig. 4.7 presents the LSPR spectra of LI-SNSA samples

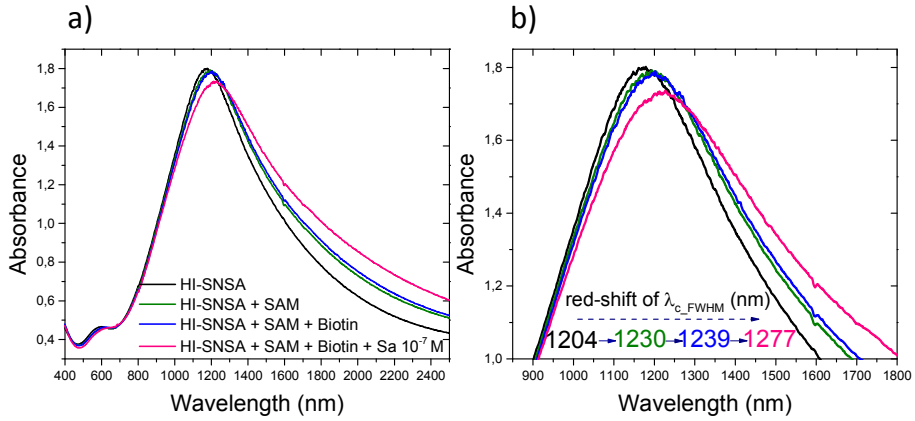

Figure 4.6: a) LSPR spectra for a sample of HI Au-Ag SNS arrays before and after functionalization with bio-molecules (the $\lambda_c$values were calculated choosing a threshold at the value of absorbance (Ath) at the 50% of the peak height): λ_c of the sample as deposited (black line) is 1204 nm; λ_c after functionalization with SAM is 1230nm (green line); λ_c after functionalization with Biotin is 1239 nm (blue line); λ_c after exposition of 100 nM of Streptavidin is 1277 nm (pink line). b) Zoom of the LSPR spectra of figure a.

before and after the biorecognition event (biotin-streptavidin) for different streptavidin concentrations.

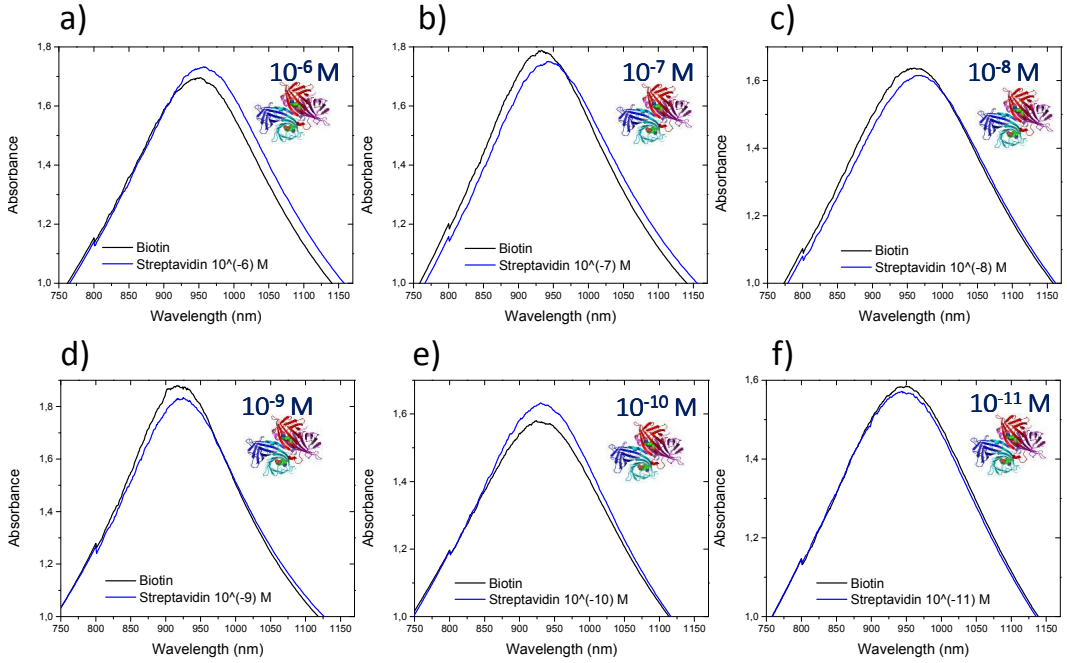

Figure 4.7: LSPR spectra of LI-SNSA samples after the functionalization with biotin and different concentrations of Streptavidin: a) [SA] 10^{-6}M; b) [SA] 10^{-7}M; c) [SA] 10^{-8}M; d) [SA] 10^{-9}M; e) [SA] 10^{-10}M ; e) [SA]n 10^{-11}M.

The LSPR response curve, defined as $\Delta\lambda_c$ as a function of the streptavidin concentration, [SA], was measured in the range 10^{-13} M $\leq$ [SA] $\leq 10^{-6}$ M and the results are shown in fig. 4.8. The data have been fitted with the model of Langmuir isotherm [19], according to Eq. 4.2:

$$\Delta\lambda_c = \Delta\lambda_{c,sat}\frac{K_{a,eff}\cdot[SA]}{1+K_{a,eff}\cdot[SA]} \tag{4.2}$$

where $\Delta\lambda_{c,sat}$ is the saturation value of $\Delta\lambda_c$ and $K_{a,eff}$ is the "effective affinity constant" at the interface. The $K_{a,eff}$ and the limit of detection (LOD) of the system under study can be measured from the response curve. Van Duyne underlines the relevance of these aspects to apply the Langmuir Isotherm [73]:

1. the analyte in solution has multiple equivalent sites with the same affinity for the receptor immobilized on a surface, but only one receptor molecule binds to the analyte (1:1 Biotin-Streptavidin binding);
2. the transduction mechanism by the nanostructure is based only on the refractive index change due to the binding receptor-analyte;
3. the change in the LSPR resonance condition is due only to refractive index and the thickness of the analyte layer.

The first assumption is satisfied by the use of a ratio 1:3 of 11-MUA:1-OCT, thus the receptor is very diluted on the nanostructure's surface since it can bind only to the 11-MUA molecules by a cross linking reaction. The second assumption is satisfied by the intrinsic plasmonic properties of the nanoarray, while the third one, was verified by measuring a biotin functionalized sample exposed to a blank solution without the analyte (only PBS): no shift of the LSPR peak was measured after the exposure to Phosphate Buffered Saline (PBS). For these reasons the Langmuir Isotherm model can be used to explain the experimental results. The LOD is estimated as the abscissa of the intersection point between the confidence interval associated with the non-response point and the sensing curve, as shown in Figure 4.8. For the LI-SNSA the experimental results have shown $K_{a,eff}$ = (1.0 $\pm$ 0.5)$\times 10^9$ M^{-1}, a saturation value $\Delta\lambda_{csat}$ = 10 $\pm$ 1 nm and a LOD = 2×10^{-10} M, whereas for the interacting case (HI-SNSA) the results are: $K_{a,eff}$=(3.3 $\pm$ 0.5)$\times 10^9$ M^{-1}, $\Delta\lambda_{c,sat}$ = 36 $\pm$ 1 nm and a LOD = 3×10^{-11}M.

The similar values of $K_{a,eff}$ obtained for HI- or LI-SNSA indicate that the biotin-streptavidin interaction is not largely affected by the degree of coupling among SNSs but is almost controlled by the SNS morphology. As expected, the measured $K_{a,eff.}$ is lower than the K_a

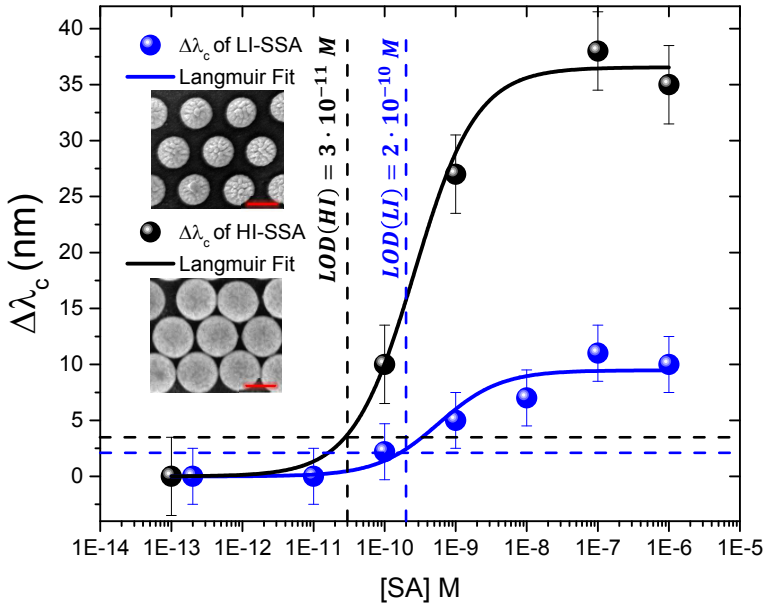

Figure 4.8: Measured response curves of $\Delta\lambda_c$ versus [SA] for the binding of SA to a biotinylated SNSs surface for the LI and HI samples. The solid line is the calculated value of $\Delta\lambda_c$ using Langmuir Isotherm described in eq. 4.2. Inset: SEM image of LI- and HI-SNSA samples.

referred to binding events in solution, and this be ascribed to the different constraints imposed by the solid-liquid interface. In fact, in this configuration the binding is influenced by the concentration and orientation of the ligand and by its interaction with the surface [71]. The LOD obtained with SNSA for Streptavidin is comparable to the value obtained in other works using Au nanoparticles-enhanced SPR sensors [85], confirming the high sensitivity of these systems which can be further improved by optimizing the functionalization protocol and the structural parameters of the nanoarray.

4.3.2 Aspecific test

Another important feature investigated for the development of sensing devices is the sensor sensitivity to an aspecific signal. In order to study the specificity of the SNSA's LSPR response and to confirm the protective effect of the thiols layer and of the PEGylated biotin, the SNSA were functionalized with SAM and biotin and exposed to a very high concentration of BSA (albumin from bovine serum). BSA is a protein with a molecular weight similar to that of streptavidin, and it is usually used to simulate the effect of an interfering species in a biological solution of analyte, such as proteins. [73, 86] The typical

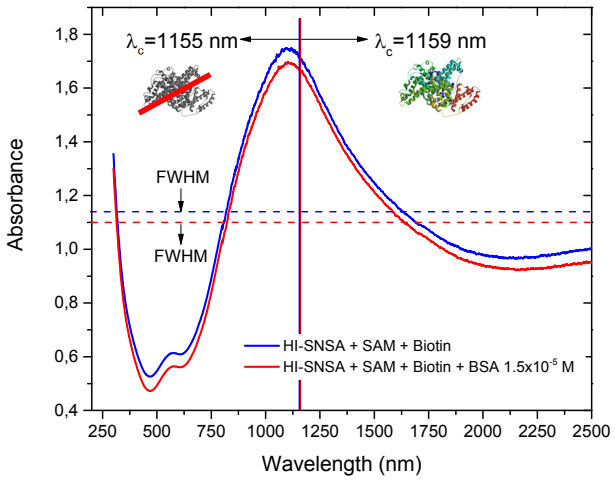

Figure 4.9: LSPR spectra for a sample of HI Au-Ag SNS arrays functionalized with bio-molecules: the λ_c at the FWHM of the peak is 1155 nm after functionalization with biotin (blue line); λ_c at the FWHM after incubation with BSA (1mg/ml)(red line) is 1159 nm.

concentration of BSA used is 1 mg/ml corresponding to a concentration of 1.5×10^{-5} M. In the present case a sample of HI-SNSA was tested and the results obtained are showed in fig. 4.9. The $\Delta\lambda_c$ measured is +4 nm (i.e., about 10 % of the $\Delta\lambda_{c,sat}$), using a concentration two orders of magnitude higher than the saturation value for streptavidin, and this shows that there is not a dramatic effect of aspecific response, in agreement with the results of BSA exposure in Ag nano-prism arrays [73]. Moreover, the SNS arrays are stable after all the chemical treatments and this is confirmed by the morphological analysis of functionalized samples. The stability of these systems is very important for the realization of devices, because it is necessary to avoid changes of the LSPR spectra that could be due to alterations of the structure.

4.3.3 Intensity-interrogation approach

So far, the approach that we used is based on a wavelength-interrogation mode, i.e., we measured the absorbance at normal incidence by scanning the wavelength of light. We have explored also the possibility of using SNSA as an intensity-interrogated biosensor. Therefore, instead of monitoring the LSPR peak centroid shift, we measured the difference in absorbance after exposure to the analyte at a fixed λ. This method is based on the difference between the absorbance values (A) before and after the streptavidin detection,

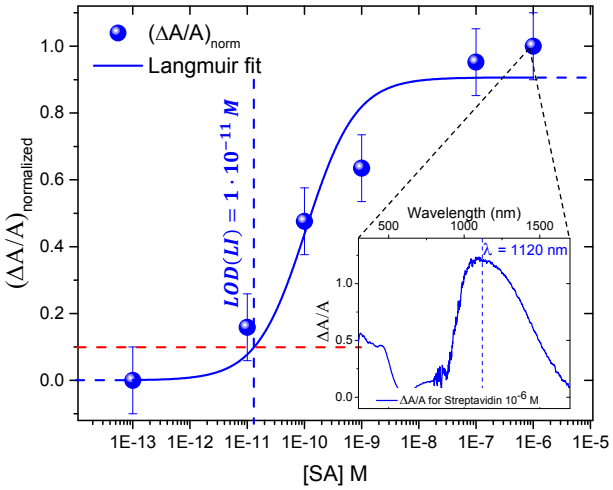

Figure 4.10: The normalized ratio $\Delta A/A$ in a LI-SNSA versus the streptavidin molar concentration, [SA], at a fixed wavelength of 1120 nm. The solid line is the calculated value of the normalized $\Delta A/A$ using the Langmuir Isotherm. Inset: normalized $\Delta A/A$ for the streptavidin detection at the highest concentration (10^{-6} M) as a function of the wavelength.

which can be expressed as in Eq.4.3:

$$\left(\frac{\Delta A}{A}\right) = \frac{A_{analyte} - A_{receptor}}{A_{receptor}} \tag{4.3}$$

The major point here is to select the λ at which the sensor is designed to operate. As a possible criterion, we used a λ which is about at the maximum point of the $\Delta A/A$ for the highest explored streptavidin concentration (10^{-6} M), where the curve exhibits also the largest stability (i.e., smallest local derivative) as it can be seen in the inset of fig. 4.10. Moreover, this λ corresponds approximately to the inflection point of the LSPR spectra after the maximum, which demonstrated to be very sensitive to dielectric environment changes. For the data in fig. 4.10 (LI-SNSA) the wavelength used is 1120 nm and the normalized absorbance ratios were calculated for all the analyte concentrations.

$$\left(\frac{\Delta A}{A}\right)_{norm} = \left(\frac{\Delta A}{A}\right)_{norm,sat} \frac{K_{a,eff} \cdot [SA]}{1 + K_{a,eff} \cdot [SA]} \tag{4.4}$$

where $(\Delta A/A)_{norm,sat}$ is the saturation value of the $(\Delta A/A)_{norm}$. The fit of these data with the Langmuir Isotherm, described in equation 4.4, results in a $K_{a,eff}$=$(8 \pm 5) \times 10^9$ M^{-1} with a limit of detection of about $1{\times}10^{-11}$ M. These results are consistent to those obtained with the centroid analysis and for the LI-SNSA indicate that an enhanced LOD

can be attained, showing that the SNSA are promising systems also for a fixed wavelength detection scheme.

4.3.4 Sensitivity comparison with nano-prism arrays (NPA)

We have compared the LSPR sensing performances of the bimetallic SNSA with the typical ordered nanostructures that can be synthesized by Nanosphere Lithography, the nano-prism arrays (NPA) [73]. In this system the functional nanounit is a silver triangular nanoprism obtained by a NSL patterning followed by thermal evaporation of metal [57, 73, 87]. In our case, the nanoprisms have a lateral size of 116 ± 5 nm and a height of 50 ± 5 nm. The typical morphology of Ag NPA obtained by silver thermal evaporation is shown in fig. 4.11 (a). The LSPR peak is around 700 nm, as showed in Figure 4.11 b. The

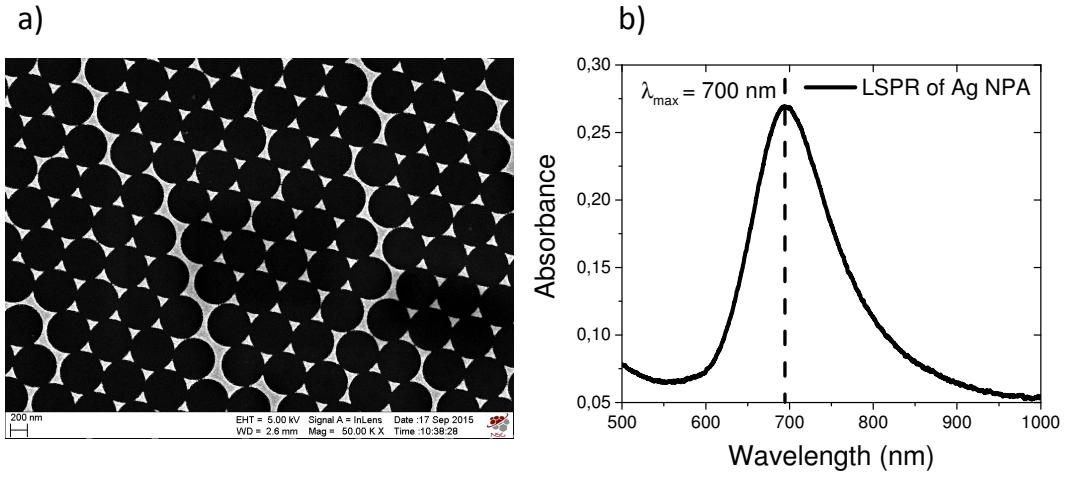

Figure 4.11: a) SEM image at magnification 50.00 KX of a Ag NPA; b) LSPR spectrum of the sample.

bio-functionalization strategy is the same as the one used in the case of SNSA.
The bio-sensing performances of Ag NPA were explored only for a high concentration of streptavidin (10^{-7} M).
The LSPR peak is red-shifted after each step of the functionalization protocol as a result of the successful binding of the molecules (see figure 4.12). The LSPR spectra evolution after the bio-functionalization of Ag NPA is shown in fig. 4.12 and the λ_c values obtained are in table 4.1. Using the centroid method at FWHM, previously described, we have obtained the λ_c at each step: after functionalization with SAM λ_c is shifted of +5 ± 1 nm, after biotin of +8 ± 1 nm and after exposure to 100 nM of streptavidin of +8 ±

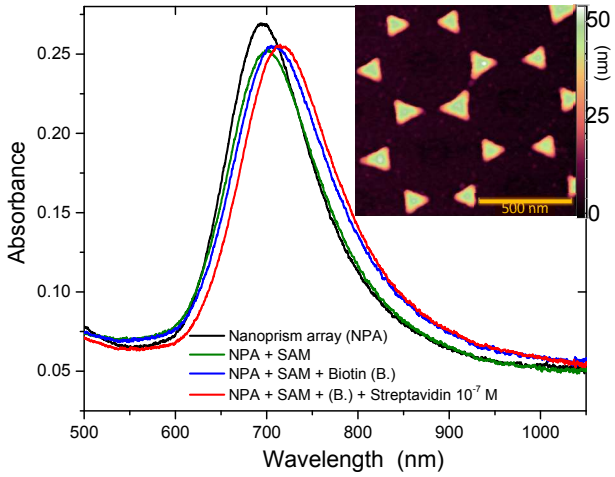

Figure 4.12: LSPR spectra for a sample of Ag triangular nanoprisms arrays (NPA) with lateral size L = 116 nm, and height h = 50 nm functionalized with bio-molecules: λ_c of the sample as-deposited (black line) is 695 nm; λ_c after functionalization with SAM is 700 nm (green line); λ_c after functionalization with Biotin is 708 nm (blue line); λ_c after exposition of 100 nM of Streptavidin is 716 nm (red line). Inset: AFM image of a typical sample of Ag triangular NPA.

AS	**SAM**	**Biotin**	**[SA] 10^{-7} M**
λ_c **(nm)**	λ_c **(nm)**	λ_c **(nm)**	λ_c **(nm)**
695	700	708	716

Table 4.1: λ_c of LSPR spectrum of Ag NPA after each step of the bio-functionalization.

1nm. LI-SNSA gave comparable results as NPA, even if NPA nanoprisms were made of Ag whereas SNSA are a Au-Ag alloy. Moreover, HI-SNSA provided better performances in terms of a higher saturation shift, thus demonstrating that SNSA constitute a very interesting nanoarchitecture for LSPR-based bio-sensing of thin molecules layers.

4.3.5 Local and bulk sensitivity of NPA and SNSA

We tried to interpret these results by comparing the bulk sensitivity $S_{bulk} = \partial\lambda_c/\partial n$ of SNSA and NPA. To estimate the bulk sensitivity of Ag NPA we exposed the samples to a solution of pure ethanol with a refractive index of 1.358 at λ of 750 nm. For the symmetric form of the LSPR spectrum we considered the λ_c at FWHM as a good parameter to represent also the maximum of the peak. Exposing the samples to ethanol we measured a red-shift of 77 nm for Δn=0.358 with respect to air (n=1). The LSPR red-shift of Ag NPA

can be seen in figure 4.13, in which we report the measure of a sample in dry condition (air) and in ethanol solution. The experimental bulk sensitivity of Ag NPA is $S_{bulk}^{(NPA)} = 215 \pm 10$ nm/RIU which is comparable with the values ranging from 200 nm/RIU to 260 nm/RIU reported in literature [56, 57]. In the case of SNSA to measure the bulk sensitivity we used a solution of Norland Optical Adhesive 61 (NOA 61) (n=1.542 at λ 1303 nm) for a Δn=0.542 RIU with respect to air. The NOA 61 is liquid photopolymer that cures when exposed to ultraviolet light, so after the exposure to UV the film is solidified on SNSA. In the case of SNSA we have obtained a bulk sensitivity of $S_{bulk}^{(SNSA)} = 405 \pm 10$ nm/RIU, as can be seen in figure 4.14. These performances are a consequence of the higher bulk sensitivity, with respect to NPA. We have obtained also comparable results from Finite Elements Simulations on SNSA and NPA systems. From the simulations, we also calculated the average effective decay length of the fields λ_{eff}, obtaining a value of 55 $\pm$ 5 nm for LI-SNSA and 20 $\pm$ 3 nm for HI-SNSA. Using the decay length, it has been possible [57] to obtain an estimate for the local sensitivity $S_0 \sim S_{bulk}/\lambda_{eff}$, which resulted 7 RIU^{-1} for LI-SNSA and 20 RIU^{-1} for HI-SNSA. Using the decay lengths of NPA which are present in literature [57], the same estimate of local sensitivity for silver NPA is 15 RIU^{-1}. These figures demonstrate that the HI-SNSA system can be more sensitive than Ag NPA, even taking into account the fact that SNSA are not made of pure Ag but of an Au-Ag alloy, which has enhanced chemical stability with respect to the pure silver case. [88]

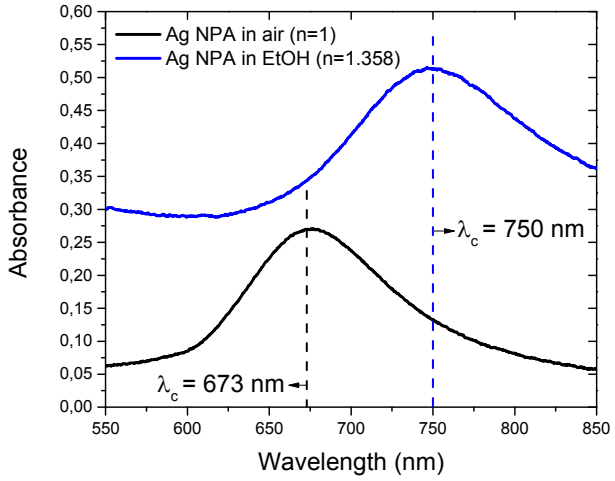

Figure 4.13: LSPR spectra of Ag NPA in air (black curve) and in Ethanol (blue curve)

.

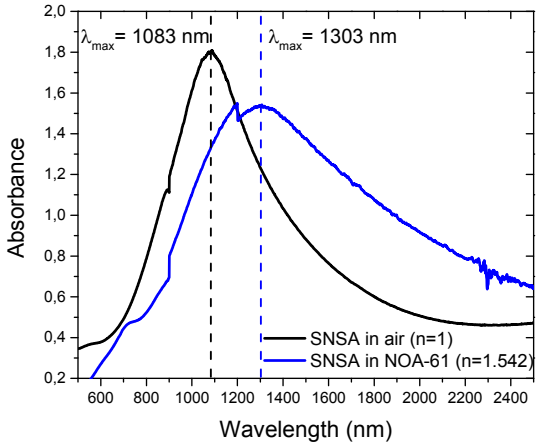

Figure 4.14: LSPR spectra of an Au:Ag SNSA sample in air (black curve) and in NOA-61 (blue curve).

4.4 Conclusions

We have synthesized ordered arrays of Au:Ag alloy semi-nanoshells (SNS) with tunable plasmonic properties in the NIR range by combining nanosphere lithography and reactive-ion etching. By controlling the gap distance between the SNSs, we have compared the label-free biosensing properties of low-interacting (LI) and highly-interacting (HI) arrays of SNS using a model system of probe-analyte couple, like biotin-streptavidin. The LOD obtained for the streptavidin molecule is of the order of 10^{-11}M and 10^{-10}M for the high interaction and low interaction SNSA, respectively, demonstrating the high sensitivity of these systems, which could be further improved by increasing the level of SNS interaction. The SNSA biosensors exhibited a remarkable immunity against aspecific interaction upon exposure to very high concentrations of BSA. An analysis of the performances of the SNSA also in an intensity-interrogation scheme was demonstrated, indicating that the LOD obtained with the low interacting SNS can be improved with the alternativ approach based on the analysis of the absorbance variation measured at a fixed wavelength. Finally, we have compared the biosensing bulk and surface sensitivity of Au:Ag alloy SNSA and Ag NPA, which are more commonly used as plasmonic sensors. The saturation response of the LI-SNSA is comparable with the results obtained with NPA, while the interacting SNSA showed a higher signal in agreement with their amplified bulk and local sensitivity.

The experimental bulk sensitivity of the Au:Ag SNSA is much higher with respect to Ag NPA and in a good agreement with FEM calculations. This demonstrates that a label-free biosensing scheme based on bimetallic SNSA improves under many aspects, and in

particular in terms of bulk and surface sensing performances, with respect to the currently established NPA-based techniques.

5 EOT for biosensing applications

5.1 Introduction

In this chapter we will describe a class of biosensors based on E-SPR phenomena and in particular on the EOT, which occurs for ordered arrays of sub-wavelength holes drilled in an optically opaque plasmonic film.

5.1.1 Extraordinary Optical Transmission of Nanohole Arrays

A NHA is a periodic array of nanometric holes in a metal thin film (with typical thickness of about 100 nm). Usually the hole diameter and the pitch of the lattice are few hundred nanometers.

EOT is a fascinating optical property of NHA discovered in 1998 by Ebbesen and his collaborators. [89] They investigated the transmission of light through NHA made of noble metal thin films. Ebbesen and co-workers demonstrated that the light transmitted through the NHA was higher than the incident one normalized to the total holes area and, for certain wavelengths, the amount of transmitted light was much higher than estimated by the classical aperture theory. [90] NHA with sub-wavelength holes of diameter d are indeed able to overcome the standard diffraction limit and to effectively transmit light with $\lambda > 2d$. These properties are due to the coupling between the E-SP and the incident electromagnetic field on the NHA. As explained in chapter 1 and 2 the periodicity of the lattice gives the extra momentum necessary to excite E-SP. The transmission process for a single aperture surrounded by periodic grooves was studied by Degiron and Ebbesen. [91] Their study indicated that the extraordinary transmission is based on three main steps: (i) the incident light with an appropriate λ excites the E-SPs on the incident surface, (ii) the excitation is transmitted through the holes and (iii) there is a re-emission of the radiation from the second surface in terms of transmitted light. [5,91] This theory can also be applied

to the case of sub-wavelength holes arrays. EOT has been demonstrated and interpreted mainly in NHAs made of Au or Ag. [92] Indeed, to enhance the E-SP and, to reduce the losses, the metal film should have a high absolute value of the real part of the dielectric constant and a small imaginary part. Therefore, Au and Ag are the best candidates for their intrinsic properties.

Due to the ordered nature of the array, EOT can occur at different wavelengths, whose position is related to the periodicity of the lattice. The λ_{EOT} of EOT for a sub-wavelength holes arrays with square symmetry and lattice constant a is expressed by [93]:

$$\lambda_{EOT}(n,m) = \frac{a}{\sqrt{(n^2+m^2)}}\sqrt{\frac{\varepsilon_m \varepsilon_d}{\varepsilon_m + \varepsilon_d}}. \tag{5.1}$$

where the integer n and m are the scattering orders of the array and ε_m, ε_d are the real part of the dielectric constant of the metal and the dielectric medium surrounding it. This equation is valid in the limit of vanishing hole size. The pitch of the lattice a can be controlled by the synthesis lithographic techniques such as NSL or EBL. [67,94] In this way it is possible to finely tune the position of the EOT transmission peaks in the visible-near infrared region of the electromagnetic spectrum. This property can be used to realize filters for specific wavelengths by simply changing the pitch of the array. [5] Other features strongly affect the transmission properties, such as the aspect ratio of the holes, the shape, the symmetry of the array and the surface roughness. These features affect the electromagnetic surface waves properties and their coupling with the incident light. [5] The thickness of the metal film (or the hole depth) can strongly affect the transmission, in particular it should be several times the penetration depth at which the light intensity is reduced by $1/e$. For instance, in the visible range, the metal penetration depth is about 20 nm; therefore, film thicknesses in the range 60-200 nm are a good compromise to obtain opaque films. The experimental results for sub-wavelength holes arrays show an EOT peak generally slightly red-shifted with respect to the theoretical prevision by equation 5.1 (see graph a in figure 5.1). [5,92] This disagreement was studied and interpreted quantum-mechanically with the model of Fano Resonance by Genet and his collaborators. [6] This red shift is explained taking into account two interfering contributions to the transmission: one is due to the direct light transmission through the holes and the other is the transmission mediated by the surface plasmon polaritons excitations at the two interfaces. The first phenomenon is a non-resonant contribution while the SPP-mediated is a resonant process. The coupling

between these two transmission processes cause a red-shift of the EOT peak as experimentally observed [6, 92] and a characteristic asymmetrical spectral shape in agreement with the Fano one in atomic physics. [95] Thus, Fano Resonance analysis demonstrated to be a good model for representing the optical properties of two dimensional sub-wavelength holes arrays, as it can be seen in figure 5.1b. The grating nature of the holes array provide a

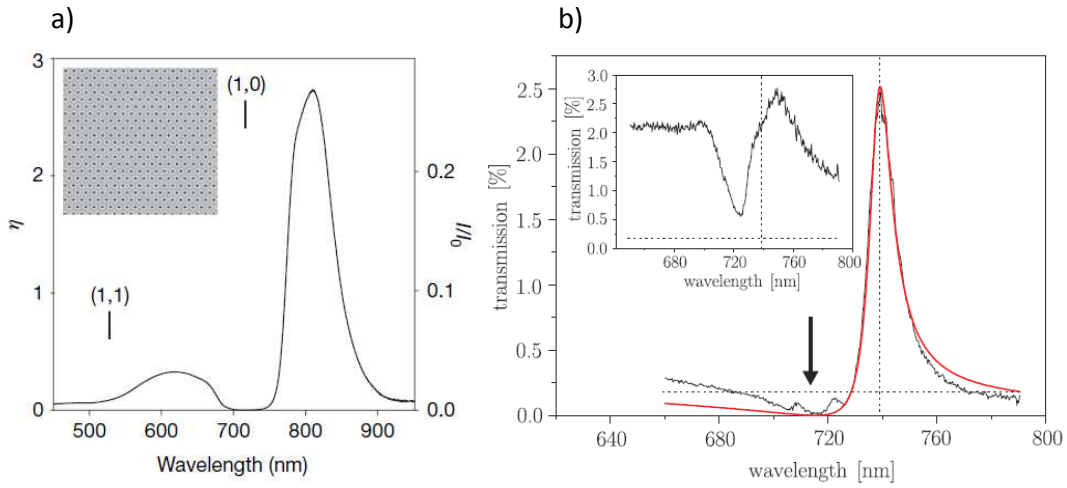

Figure 5.1: a) Transmission spectrum of triangular hole arrays (period 520 nm, hole diameter 170 nm, 225 nm thickness Au Film on a glass substrate see Inset). The transmission is measured at normal incidence using collimated white light. I/I_0 is the absolute transmission of the array and η is the transmission normalized to the hole's area [5]. b) Experimental transmission spectrum of the air-metal (1,0) SP resonance, obtained with an Au film of thickness 200 nm with a_0 = 700 nm and r = 70 nm. The smooth curve shows the fitted Fano profile [6].

different transmission orders; in particular for $\lambda > a$ (a is the period of the array) only the 0^{th} order is formed as represented by the (1,0) peak in figure 5.1a. For lower wavelengths ($\lambda < a$) the higher diffraction orders appear, such as the (1,1) peak.
The dielectric medium surrounding the holes arrays affects the position of the (1,0) EOT resonance wavelength, and this property can be exploited for sensing applications, as demonstrated for label-free optical sensors. [96–100]

5.1.2 EOT-based sensors

As it can be seen in equation 5.1 the resonance wavelength of EOT depends on the dielectric constant of the medium around the NHA and this property is exploited to realize sensing devices. The detection of chemical or biological species is based on the variation of

EOT resonance position after the receptor-analyte binding on or in proximity of the NHA's surface. [101] NHA belong to a class of plasmonic sensors based on propagating E-SP such as the typical commercial Surface Plasmon Resonance (SPR) sensors, which are based on Kreschmann configuration. However, by using NHA the sensing signal can be measured with a simple transmission technique at normal incidence, and this is very advantageous also for miniaturizing the sensing devices like in the new lab-on-a-chip technologies. Square NHAs (d = 200 nm, a = 510-618 nm, Au film thickness = 100 nm) were investigated for chemical and biological detection and the sensitivity obtained was 400 nm/RIU. [101] In other works it is reported that the surface sensitivity (which is referred to one monolayer coverage) of Au NHA synthesized by Electron Beam Lithography (EBL), can be enhanced by 2.5-3 times with thermal annealing. In that work NHA were fabricated on glass substrates with diameter 150 and 209 nm in a gold film of thickness 100 nm and with a period of 500 nm. Then, they were thermal annealed in argon atmosphere at 600°C for 1 h. With the annealing the roughness of the metal film decreases for the reduction of small islands providing a more uniform metal surface, which reduces the surface wave scattering and propagation losses. [101] The surface sensitivity for a monolayer of 2.2 nm increases from 6 nm/RIU to 16.9 and from 6.7 to 17.9 for holes diameter of 209 and 150 respectively. [102] In literature random arranged gold nanoholes on a glass slides (d = 60 nm, Au film thickness = 20 nm) were also exploited to realize specific SPR-sensors. [93] The detection was based on the red-shift of the LSPR peak after the biomolecules binding. These systems were able to detect in a sensing area of 0.1 mm^2 analyte molecules such as tumor markers in concentration less than 1 pg. [93] The measured bulk sensitivity of random gold nanoholes was 110 nm/RIU [93], suggesting that ordered arrays have to be preferred

The actual synthesis techniques such as Focused Ion Beam, EBL or NSL allow to easily change the size parameters and the morphology of these systems. [94, 103] This opens the possibility to investigate and optimize the optical properties of NHA for the development of EOT sensors characterized by high sensitivity and specificity.

5.2 NanoHole Array (NHA) fabrication and characterization

In the present work, hexagonal NHA with hole diameter in the range d=270-330 nm and period a=522 nm were synthesized by NSL. The metal film was composed by a multilayer of titanium, gold and silver, 60 nm in thickness. (1,0) EOT peak was measured by a transmittance spectrum in the near-infrared region. The local and bulk EOT sensitivities were experimentally measured. Then, the biosensing performances were investigated by functionalizing NHA with a typical couple of biological molecules, biotin-streptavidin, based on a receptor-ligand scheme. These molecules are the same used for the sensing tests of SNSA and NPA nanostructures. EOT was monitored with a transmission technique before and after the biorecognition event between the biomolecules. Moreover, numerical simulations were performed to compare the experimental results with theoretical ones.

5.2.1 Synthesis and characterization of NHA

The synthesis of NHA was based on NSL as described in chapter 3.
The process can be divided in the following steps:

1. Self-assembling of a PS nanospheres monolayer on a transparent substrate (PS Diameter D= 522 ± 12 nm);
2. reactive ion etching to reduce D;
3. multilayer metal deposition of Ti, Ag and Au by magnetron sputtering technique (total thickness 60 nm);
4. dissolution of the PS monolayer by a toluene treatment in ultrasonic bath.

The NHA were synthesized on silica substrates previously cleaned with acid piranha solution as described in chapter 3. The silica substrates were cut as rectangles with side 2 cm x 1 cm. The samples were based on holes arrays with period a=522 nm and a hole diameter in the range 270-330 nm, in a thin opaque multilayer of Ti-Ag-Au with a total thickness of 60 nm (Ti(5 nm)-Ag(45nm)-Au(10nm)). We used this particular size for the PS nanosphere of 522 nm to have the (1,0) EOT resonance in the NIR range, i.e., far enough from the interband absorption thresholds of the deposited metals in order to reduce losses and to improve the sharpness of the resonances.

The multilayer of Ti-Ag-Au was deposited in sequence by magnetron sputtering technique using two RF and one DC sources. The RF sources were used for titanium and gold, while the DC for silver. To obtain a multilayer with a fine control on the thickness of each metal layer, we performed three different deposition-rate calibrations. Starting from those calibrations we calculated the deposition rate in nm/s for Ti, Ag and Au. In our sputtering machine the three sources were positioned in the same vacuum chamber with an angle of 120° among them. The samples could be positioned in front of each source in order to obtain a good collimation of the atoms flux and, to deposit three layers in sequence in the same vacuum conditions (5×10^{-3} mbar.) This procedure avoided the formation of oxidized species in the metallic multilayer. The sample holder was set in rotation during each metal deposition to assure an uniform coverage on the total area occupied by the samples. At first, we deposited 5 nm of titanium on the etched polystyrene masks. Titanium serves as an adhesion layer because the low affinity between noble metals and silica or silicon, therefore making the Ag-Au overlayers more stable on the silica substrate for the functionalization process. A complete morphological characterization of the nanoarrays was obtained by SEM and AFM. The typical morphology of the NHA is reported in figure 5.2. The period of the lattice a is controlled by the PS diameter. The hole diameter is controlled by RIE. The width and wavelength position of EOT depend on the structural, morphological and compositional parameters of NHA. In particular on:

- period of the array a;
- holes diameter d;
- composition, roughness and height of the metal opaque film;
- aspect ratio (d/h);
- area occupied by the holes on the total area σ;
- dielectric medium surrounding the NHA.

The transmission measurements were performed by using a JASCO V-670 spectrophotometer in the range 300-2600 nm, at normal incidence and with unpolarized light. EOT spectrum of a NHA with a= 522 nm, d= 295 nm and a metal height of 60 nm presents the (1,1) peak at λ_{max} in the visible at 540 nm, while the (1,0) peak at 970 nm, as reported in figure 5.3. The Ti-Ag-Au multilayer thickness of 60 nm is sufficient for the approximation of film opacity since the corresponding continuous film exhibits a negligible transmission in the visible-infrared region where EOT is presents (see figure 5.4a). To verify the ex-

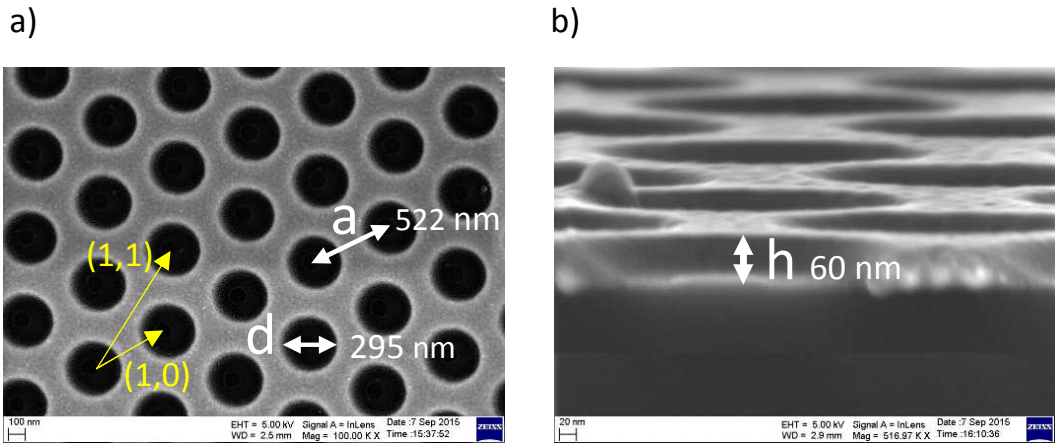

Figure 5.2: NHA of period 522 nm, hole diameter 295 nm and metal height of 60 nm: a) SEM image at magnification 100.00 KX of a typical synthesized NHA (top view); b) SEM image at magnification 516.97 KX in side view.

traordinary property of EOT we calculated the normalized transmittance with as:

$$T\%_{norm.} = \frac{T\%}{f} \tag{5.2}$$

where f is the filling factor of NHA.

$$f = \frac{A_{Holes}}{A_{NHA}} = \left(\frac{d}{a}\right)^2 \frac{\pi}{2\sqrt{3}} \tag{5.3}$$

For our NHA with a= 522 nm and hole diameter d=295 nm the filling factor is 0.2896. If we neglect the plasmonic properties of NHA we expect a transmission of about 29%. The

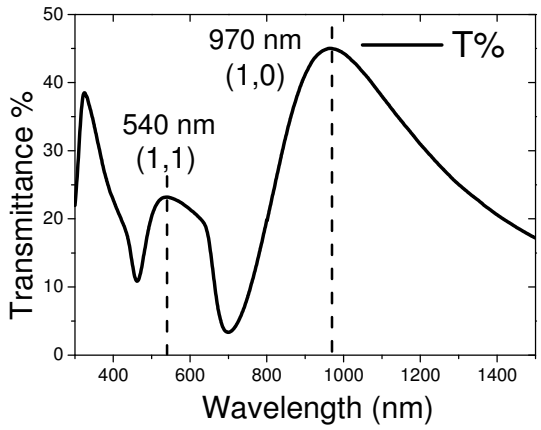

Figure 5.3: EOT spectrum of NHA a = 522 nm, d = 295 nm and Ti-Ag-Au height = 60 nm.

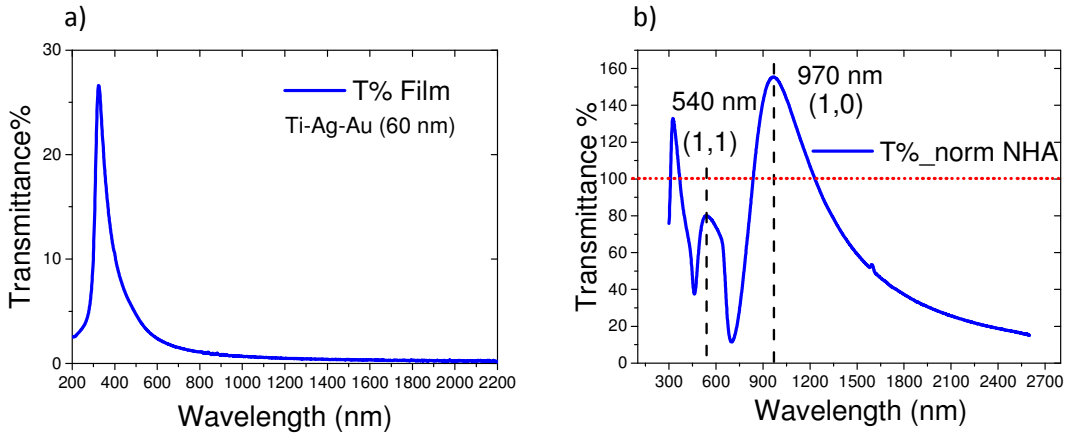

Figure 5.4: a)T% of a multilayer of Ti-Ag-Au of 60 nm deposited on a silica substrate; b)T% normalized (T%/ff) of a NHA with a 522 nm, d 295 m and a multilayer of Ti-Ag-Au of 60 nm.

transmittance normalized to the holes area is higher than 100% as it can be seen in figure 5.4b, confirming the EOT nature of the transmission peak. In the case of a two-dimensional triangular array the peak position of transmittance at normal incidence is defined by the equation [5]:

$$\lambda_{EOT}(n,m) = \frac{a}{\sqrt{\frac{4}{3}(n^2 + n\,m + m^2)}} \sqrt{\frac{\varepsilon_m \varepsilon_d}{\varepsilon_m + \varepsilon_d}}. \tag{5.4}$$

where the integer n and m are, as usual, the scattering orders of the array and ε_m, ε_d are the real part of the dielectric constant of the metal and the dielectric medium surrounding it. Changing the dielectric properties of the medium at the interface with NHA, the resonance wavelengths of EOT also changes, as expressed by equation 5.4. In this dependence on ε_d lies the refractive index sensing behavior of NHA.

5.2.2 EOT refractive index sensing

The sensing properties of NHA were exploited by analyzing the (1,0) EOT peak variation for refractive index changes. We theoretically expected a red-shift of EOT peak as the refractive index at metal/dielectric interface increases. We measured the *bulk sensitivity* and the *local sensitivity* of NHA.

The bulk sensitivity is referred to refractive index changes due to a dielectric variation with thickness much higher with respect to the decay length l_d of the electromagnetic field. The typical decay length of propagating surface plasmon polaritons in a dielectric is 100-200 nm. To measure the bulk sensitivity we deposited a polymeric layer (NOA) on the NHA's

surface with thickness some millimeters and refractive index 1.54.
On the other hand, the local sensitivity refers to dielectric changes of thickness lower than the decay length of the electromagnetic field. The local sensitivity was measured by depositing on the NHA a layer of silica (refractive index 1.45) with increasing thickness upto few tens nanometers. Then, we investigated the NHA label-free sensing performances for protein detection. NHA were functionalized with a couple of biological molecules receptor-ligand characterized by a very high affinity (biotin-streptavidin). EOT response was measured for different concentrations of the ligand molecule, in order to build a sensitivity curve EOT shift vs. analyte concentration.

5.2.3 EOT analysis

For the analysis of EOT sensing response we focused our attention only on the (1,0) EOT peak. To analyze the EOT peak red-shift, we used two different approaches, as described in figure 5.5: (i) the centroid method and (ii) the full fit with a Fano-type peak shape.

The first is based on the measure of the centroid of the peak above a well defined threshold. The centroid, λ_c, for transmittance measurements is expressed by:

$$\lambda_c = \frac{\sum_i \lambda_i (T_i - T_{th})}{\sum_i (T_i - T_{th})} \tag{5.5}$$

where T_i is the transmittance at the wavelength λ_i and T_{th} is the threshold of transmittance chosen between the peak minimum and the maximum. Only λ_i in the region where $T_i > T_{th}$ are considered to evaluate λ_c, as indicated by the gray region of the peak in figure 5.5a. The centroid takes into account the potential deformations of the peaks which are not included with the simply λ_{max} evaluation. The threshold used for the centroid analysis is the FWHM of the peak, as indicated in figure 5.5a. The peak parameter we monitored is named λ_{c-F}.
The other method we used is the Fano Resonance model, rewritten in the wavelength domain (x is a wavelength), which is expressed by the following equation:

$$y(x) = y_0 + A \cdot \frac{\left(q + \left(\frac{1}{x} - \frac{1}{x_0}\right) \cdot \sigma\right)^2}{1 + \left(\left(\frac{1}{x} - \frac{1}{x_0}\right) \cdot \sigma\right)^2} \tag{5.6}$$

Fitting the experimental EOT with Fano Resonance model we monitored the parameter x_0, which represents the wavelength position of the EOT resonance peak. The Fano fit was done for the part of the peak above the inflection point, but this detail will be treated in the following sections.

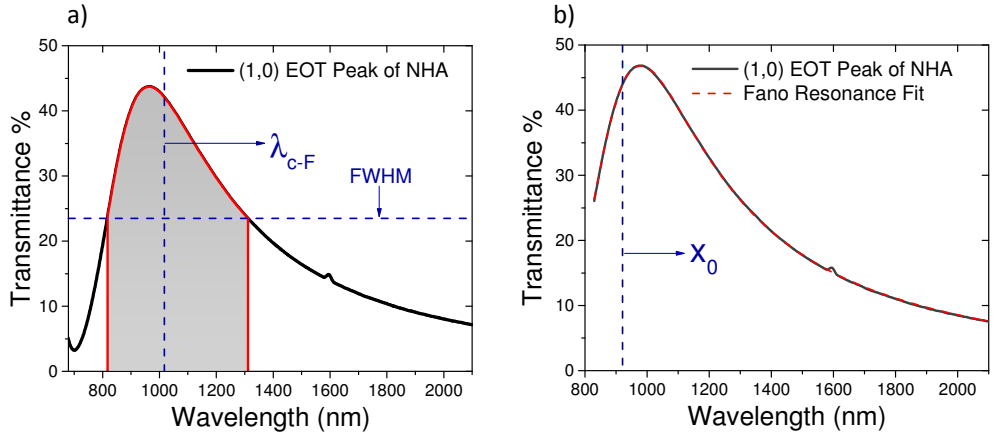

Figure 5.5: a) Representation of the centroid method to evaluate the λ_c of the (1,0) EOT peak; b) Fano Resonance Fit (red curve) of the (1,0) EOT peak in the range 830-2600 nm.

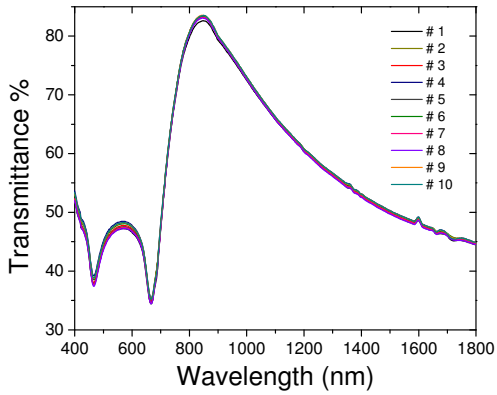

Measure	λ_{c-F} (nm)	x_0 (nm)
1	915.1	716.7
2	914.0	717.5
3	913.1	716.7
4	913.6	717.6
5	913.5	718.0
6	914.7	716.3
7	915.4	718.0
8	915.1	718.8
9	913.5	718.2
10	914.1	719.2
Average	**914.2 ± 0.8**	**717.7 ± 0.9**

(a) **(b)**

Figure 5.6: Repeated measurements of EOT spectrum by repositioning each time the NHA on the sample holder. In the table the λ_{c-F} and x_0 values of each measurement and their average are reported. The error associated is the standard deviation.

The optical measurements of NHA before and after refractive index changes were done positioning the NHA on a sample holder. To take into account the systematic error associated to the repositioning of the sample, we acquired several EOT spectra of the same

NHA. For each measurement the sample was repositioned on the sample holder. We did this procedure ten times and we verified a good reproducibility of the measure as shown in figure 5.6. The resulting λ_{c-F} and the x_0 values are reported in table b. The error associated to the average was calculated as the standard deviation of the measurements. The systematic error associated to the λ_{c-F} and x_0 values can be considered 1 nm.

5.3 Local and bulk sensitivity of NHA

Numerical simulations have been carried out using a commercial software for finite elements method (FEM) computations (COMSOL Multiphysics, version 5.2). The geometric parameters of the NHA were measured by AFM and scanning electron microscopy and then used to define the model. The material properties were described by their relative dielectric permittivity functions $\varepsilon(\omega)$. Numerical simulations were used to evaluate the order of magnitude of the local and bulk sensitivity of this class of NHA. For the comparison between experimental and theoretical results we have to take into account that the simulated nano-holes arrays have a perfect geometric structure with respect to the experimental samples. In the model, the holes are represented by perfect cylinders but, in the real systems, the holes are characterized by rounded edges and a more rounded geometry. Moreover, the presence of defects in the real samples, which are not considered in the ideal model, can affect the width and the shape of the EOT spectrum. The experimental dielectric functions ($\varepsilon(\omega)$) of gold and silver were measured by ellipsometry on thin films of the corresponding metals deposited by magnetron sputtering in the same conditions as for the NHA. The spectroscopic ellipsometric measurements were performed with a V-VASE ellipsometer by the J.A. Woollam Co., Inc. and the data were analyzed with a WVASE32® software. Nanometric layers of gold or silver (50 nm in thickness) were deposited on silicon substrates previously cleaned with an acid piranha solution. The thickness of the films was measured by AFM. The ellipsometric measurements were performed in the wavelength range 300-1700 nm for incidence angles in the range 55°-75° each 5°. We have obtained the ε_{Ag-exp} and ε_{Au-exp} of our Au and Ag films. We have also measured the $\varepsilon_{Ti-Ag-Au}$ of a multilayer of Ti(5 nm)-Ag(45 nm)-Au(10 nm). The experimental ε_{Ti-exp} was obtained by using ε_{Ag-exp} and ε_{Au-exp} previously measured.

5.3.1 Local sensitivity: experimental results

The EOT shift ($\Delta\lambda_{peak}$) for a Δn variation can be expressed by [14, 57]:

$$\Delta\lambda_{peak}(d_a) = \lambda_{peak}(d_a) - \lambda_{peak}(0) = S_{bulk}\Delta n\left[1 - \exp\left(-\frac{2d_a}{l_d}\right)\right] \tag{5.7}$$

where $\Delta\lambda_{peak}(d_a)$ is the red-shift of EOT peak due to the presence of a new dielectric layer with thickness d_a. In our case $\Delta\lambda_{peak}$ is expressed by $\Delta\lambda_{c-F}$ or Δx_0 if we use the centroid method or Fano model, respectively. S_{bulk} is the bulk sensitivity of NHA, $\Delta n = n_a - n_e$ is the refractive index variation (n_e is the refractive index of the environment such as air, n_a is the analyte's one) and l_d is the decay length of the plasmonic field. The calculated decay length l_d for our NHA is 106 ± 6 nm in a medium such as silica (n=1.45) and 76 ± 4 nm in air. In the case of biosensing applications n_a can be considered the refractive index of the analyte molecules to be detected (n = 1.5). In the limit of $d_a \gg l_d$ we obtain the equation for the bulk sensitivity (S_{bulk}).

$$\Delta\lambda_{peak}(\infty) = S_{bulk}\Delta n. \tag{5.8}$$

The local sensitivity is defined by the following equation:

$$S_0 \equiv \frac{1}{\Delta n}\left.\frac{\partial\lambda_{peak}}{\partial d_a}\right|_{d_a=0} \tag{5.9}$$

This equation may be approximated to first-order in the limit of $d_a < l_d$, such as in the case of thin dielectric layers, obtaining the following linear function:

$$\lambda_{peak}(d_a) \approx \lambda_{peak}(0) + S_{bulk}\Delta n\left[1 - \left(1 - \frac{2d_a}{l_d}\right)\right] = \lambda_{peak}(0) + \left(\frac{2S_{bulk}\Delta n}{l_d}\right)\cdot d_a \tag{5.10}$$

Therefore the link between local and bulk sensitivity can be obtained by applying eq.5.9 to eq.5.10 as:

$$S_0 = \frac{2S_{bulk}}{l_d} \tag{5.11}$$

To evaluate the local sensitivity of Ti-Ag-Au NHA we deposited incremental silica (SiO_2) layers with total thickness 13, 24, 36 nm on the NHA's surface. We used the magnetron sputtering technique to deposit three nanometric SiO_2 layers with a fine control on the thickness. The silica refractive index, n has a value of 1.45 in the range of λ = 800-1500

nm where the (1,0) EOT peak is located. The silica refractive index is very similar to that of biological molecules (n ∼1.5), so it is very used to simulate the response of nano-sensors to a functionalization with these molecules.

The NHA have a period of 522 ± 12 nm, a hole diameter of 295 ± 10 nm and a metal height of 60 ± 3 nm. The substrate is an hyper-pure silica glass HSQ 300 by Haereus. The silica films were also deposited on a silicon substrate to measure by AFM and SEM their incremental thickness after each deposition, as can be seen in figure 5.7. EOT spectra

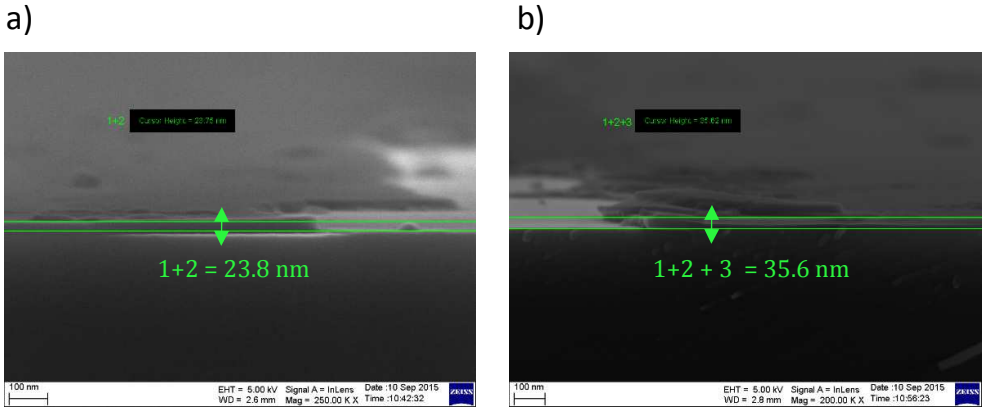

Figure 5.7: a)SEM image at 250.00 KX of a silica layer of ≈ 24 nm (layer 1 + layer 2) deposited on a silicon substrate (cross view); b) SEM image at 200.00 KX after three SiO_2 depositions (layer 1 + layer 2 + layer 3); the total thickness is 36 nm (cross view).

were acquired before and after each silica deposition. The spectra were analyzed by using the centroid method and the model of Fano Resonance. As theoretically predicted, the refractive index change due to the difference between air (n=1) and silica (n=1.45) induced a red-shift of the transmission peak wavelength position, which can be seen in figure 5.8. The centroid values after each silica deposition are reported in figure 5.9bb. λ_{c-F} was red-shifted of 13 ± 1 nm, 12 ± 1 nm and of 14 ± 1 nm for 13, 24, 36 nm of SiO_2 layers, respectively. Since the silica total thickness is lower than l_d (36 nm vs 53 nm) we can use the approximation expressed in the equation 5.10. The local sensitivity of Ti-Ag-Au NHA can be obtained using a linear fit of λ_{c-F} as a function of the silica thickness with the equation $y = m\,x + q$. The slope, m, which results from the linear fit is 1.08 ± 0.03, while the intercept is 1017 ± 1 nm. The local sensitivity S_0 can be calculated by dividing m for the refractive index difference n_{SiO_2} - n_{air} (Δn = 0.45):

$$S_{0-exp}^{centroid} = \frac{m}{n_{SiO_2} - n_{air}} = 2.4 \pm 0.1\ RIU^{-1} \tag{5.12}$$

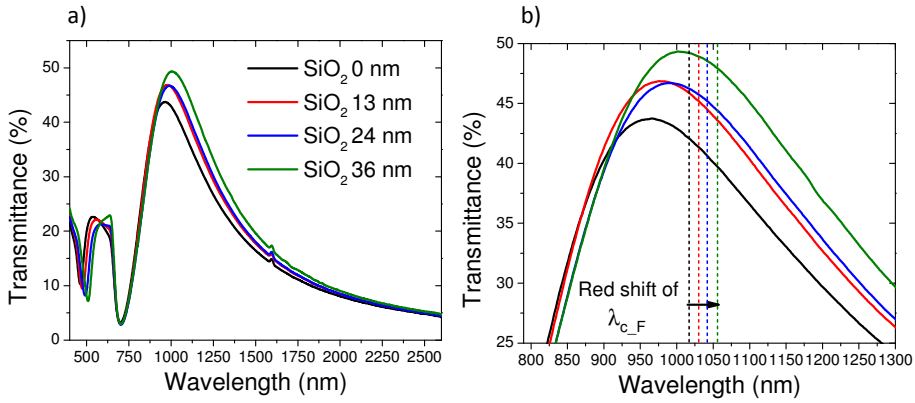

Figure 5.8: a) experimental EOT spectra of a Ti-Ag-Au NHA before and after silica layers depositions: sample without silica (black line), sample covered with 13, 24 and 36 nm of SiO_2 is respectively presented by red, blue and green lines. b) Zoom of graph a. The short dash lines indicates the λ_{c-F} red-shift after each deposition.

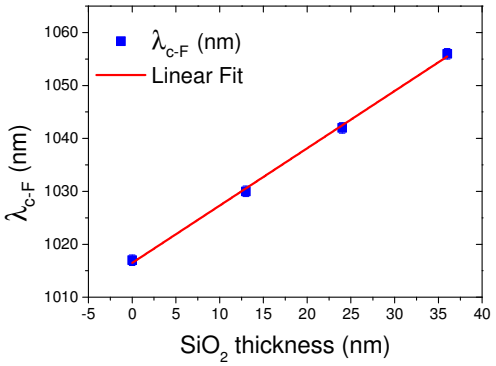

(a)

SiO_2 thick. nm	λ_{c-F} nm	σ nm	$\Delta\lambda_{c-F}$ nm
0	1017	1	-
13	1030	1	+ 13
24	1042	1	+ 12
36	1056	1	+ 14

(b)

Figure 5.9: The graph a represents the linear fit of λ_{c-F} in function of the silica thickness. The table in b reports the centroid values before and after each silica deposition.

EOT peaks were also analyzed by fitting the curve with the Fano Resonance model described in equation 5.6. We restricted the fit to the (1,0) peak so it was necessary to select one region of the optical transmission starting from a given λ_0. Then, Fano Resonance fit was done from λ_0 to the maximum measured value of the peak (2600 nm). The evaluation of x_0 as a function of the λ_0 value was done in the wavelength region from 810 to 865 nm every 5 nm. In the legend of graph a in figure 5.10 we indicate with different colors the λ_0 used for the analysis of the peak: e.g., in the case of λ_0 835 nm, we excluded from the fit the transmission values corresponding to $\lambda < 835$ nm, and the fit was done from 835 to 2660 nm. This analysis showed that above the inflection point of the curve (λ_0 higher than 800 nm) the Fano Resonance fit is not perturbed by the choice of λ_0. For the transmission

spectra after the silica depositions we obtained x_0 of 921 ± 2.0 nm (13 nm SiO_2), 943 ± 2 nm (24 nm SiO_2) and 969 ± 2 nm (36 nm SiO_2), respectively. The error associated to the average x_0 is the standard deviation of 12 measurements. The x_0 of the (1,0) EOT peak was red-shifted by 19 ± 1 nm, 22 ± 1 nm and 26 ± 1 for incremental silica thickness from 13 to 36 nm. The linear fit of x_0 as a function of the silica thickness gives a slope of 1.9 ± 0.1 nm. The local sensitivity with Fano Resonance analysis is therefore:

$$S_{0-exp}^{x_0} = \frac{m}{n_{SiO_2} - n_{air}} = 4.2 \pm 0.2\ RIU^{-1} \tag{5.13}$$

The better sensitivity of the Fano analysis with respect to the centroid one stems from the fact that it is a global fit of the curve and not just a measure of its 'center of mass' evaluation.

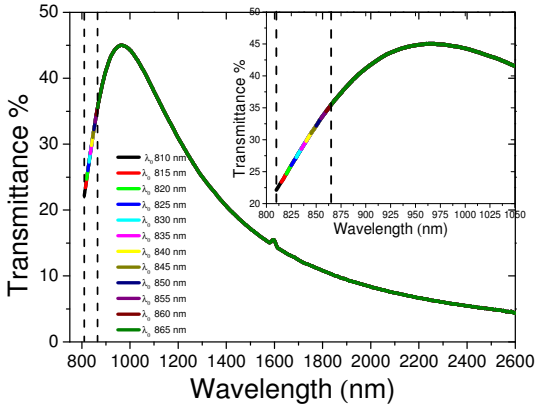

Figure 5.10: a)EOT spectrum of NHA. Each colored part indicates a different λ_0; the Fano Resonance Fit is calculated from λ_0 to the end of the measure (2600 nm).

5.3.2 Local sensitivity: numerical simulations

The sensing properties of NHA were investigated by numerical simulations to compare the theoretical and experimental results. The EOT properties obtained by simulations are referred to a NHA with a period a= 522 nm, a hole diameter d=290 nm and a multilayer of Ti (5 nm), Ag (45 nm) and Au (10 nm). To simulate the presence of a dielectric medium on the NHA 's surface we used the silica refractive index. We have simulated the presence of an incremental silica layer with thickness from 13 to 39 nm with a refractive index n=1.45. The simulated (1,0) EOT spectra before and after the addition of the silica layers are reported in figure 5.12. The slope of the linear fit of λ_{c-F} in function of the SiO_2 thickness

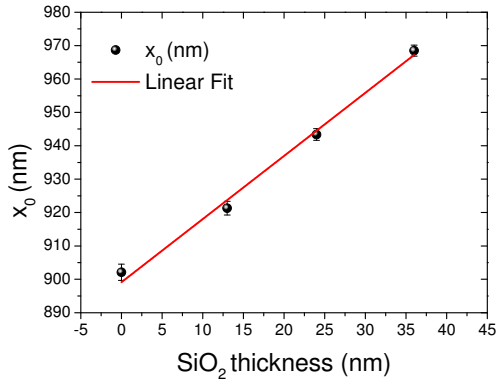

(a)

SiO_2 thick. nm	x_0 nm	σ nm	Δx_0 nm
0	902	1	-
13	921	1	+ 19
24	943	1	+ 22
36	969	1	+ 26

(b)

Figure 5.11: The graph a represents the linear fit of x_0 as a function of the silica thickness. The table in b reports the x_0 values before and after each silica deposition.

is $m = 0.9 \pm 0.1$ and $q = 824 \pm 1$ nm. The slope of the linear fit of x_0 in function of the SiO_2 thickness is 1.1 ± 0.1 and q is 769 ± 2 nm. The local sensitivity obtained with the centroid method and the Fano Resonance fit results in:

$$S_{0-theor}^{centroid} = 2.0 \pm 0.2\ RIU^{-1} \tag{5.14}$$

$$S_{0-theor}^{x_0} = 2.4 \pm 0.2\ RIU^{-1} \tag{5.15}$$

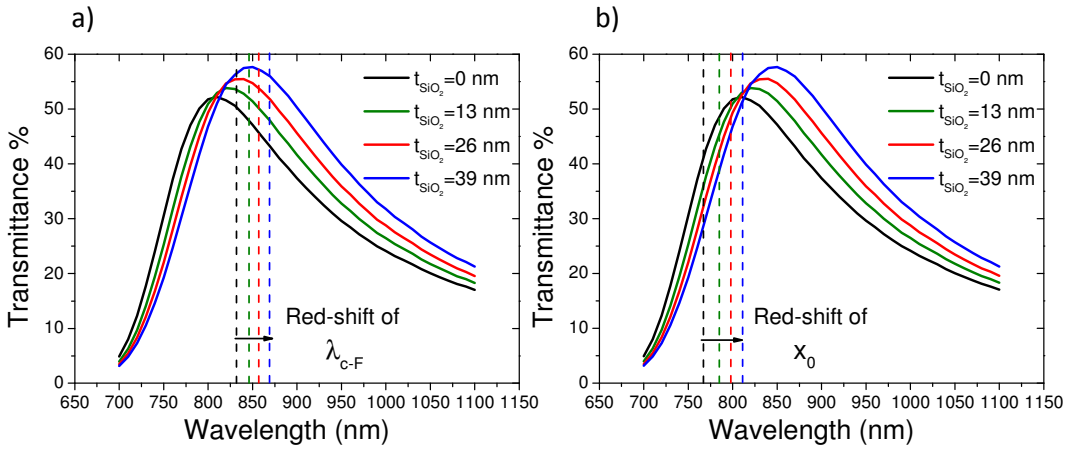

Figure 5.12: Simulated (1,0) spectra of the NHA (a=522 nm, d= 290 nm, Ti-Ag-Au (5-45-10) 60 nm) in air (black line) and covered with increasing layers of silica, 13 nm (green line), 26 nm (red line) and 39 nm (blue line): a) The dash lines indicate the red-shift of the centroid with increasing silica thickness; b) The dash lines indicate the red-shift of the x_0 parameter obtained with the Fano Resonance fit with increasing silica thickness.

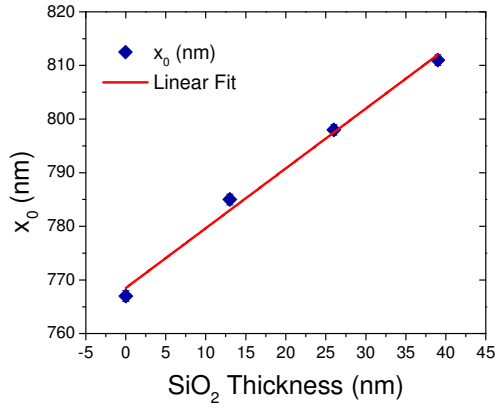

(a)

SiO_2 thick. nm	x_0 nm	σ nm	Δx_0 nm
0	767	1	-
13	785	1	+ 18
26	798	1	+ 13
39	811	1	+ 13

(b)

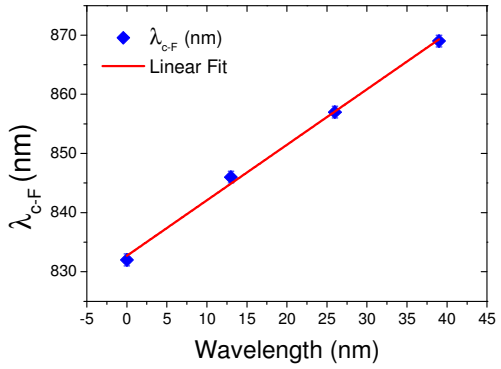

(c)

SiO_2 thick. nm	λ_{c-F} nm	σ nm	$\Delta\lambda_{c-F}$ nm
0	832	1	-
13	846	1	+ 14
26	857	1	+ 11
39	869	1	+ 12

(d)

Figure 5.13: Graph a represents the linear fit of x_0 as a function of the silica thickness. The table in b reports the x_0 values before and after each silica deposition. The graph c represents the linear fit of λ_{c-F} as a function of the silica thickness. The table in d reports the λ_{c-F} values before and after each silica deposition.

5.3.3 Bulk sensitivity: experimental vs theoretical results

As already described, we nanofabricated NHA with a multilayered structure, Ti-Ag-Au. To better understand why we preferred this choice with respect to a simpler monoelemental (Au or Ag) case, it's useful to compare the simulated bulk sensitivity, S_{bulk} for an identical NHA with the multilayered structure and the simple monoelemental one. The results are reported in Tab.5.1

From this result, the multilayered structure demonstrated the highest sensitivity among the investigated compositions: we therefore used it as the final structure of the experimentally nanofabricated NHAs, also considering its expected better chemical and mechanical stability in terms of better adhesion and reduction of oxidation processes.

The bulk sensitivity was then experimentally measured by the deposition of a layer of

NHA composition	S_{bulk} nm/RIU
Au	290 ± 25
Ag	311 ± 25
Ti-Ag-Au	315 ± 17

Table 5.1: simulated bulk sensitivity, S_{bulk}, for NHAs with the same geometry (a=522 nm, d=290 nm, total thickness 60 nm) but different composition: (i) pure Au, (ii) pure Ag, (iii) multilayer Ti (5 nm) - Ag (45 nm) - Au (10 nm).

Norland Optical Adhesive-61 (NOA-61) on the NHA's surface. NOA-61 is a liquid photopolymer that polymerizes under ultraviolet exposure; after 1h of UV treatment, NOA-61 forms a homogeneous solid film on the NHA, whose thickness is few millimeters, i.e., much larger than the decay length l_d of the propagating plasmons of NHA (few hundreds nm). NOA-61 has a refractive index defined by:

$$n(\lambda) = 1.5375 + \frac{8290.45}{\lambda^2} - \frac{2.11 \cdot 10^8}{\lambda^4} \tag{5.16}$$

The used NHA for this experiment has a period $a = 522 \pm 12$ nm, a hole diameter of d= 320 ± 8 nm and the metal multilayer height is 60 ± 3 nm. The EOT spectrum was measured before and after the NOA-61 deposition. As expected, EOT peak was red-shifted by the NOA refractive index, as reported in figure 5.14. The analysis of the EOT was done by the centroid method. We measured a λ_{c-F} variation of 144 nm for a bulk refractive index change of 0.54. The λ_{c-F} of the NHA is 1012 nm and 1156 respectively before and after the NOA-61 deposition. To simulate the bulk sensitivity air (n=1) at the interface with the NHA was replaced in the calculations by a medium with a refractive index of n=1.52 (similar the one of NOA). The λ_{c-F} of the simulated EOT spectrum is red-shifted of 163 nm as can be seen in graph b in figure 5.14. The resulting experimental and simulated bulk sensitivity, S_{bulk}, resulted:

$$S^{centroid}_{bulk-exp} = \frac{\Delta\lambda_{centroid}}{n_{NOA} - n_{air}} = 267\, nm \cdot RIU^{-1} \tag{5.17}$$

$$S^{centroid}_{bulk-theor} = \frac{\Delta\lambda_{centroid}}{n_{1.52} - n_{air}} = 314\, nm \cdot RIU^{-1}. \tag{5.18}$$

The analysis of the EOT spectra was also done with the Fano Resonance model. The Fano parameter x_0 of the experimental spectrum is 907 nm before the NOA-61 deposition

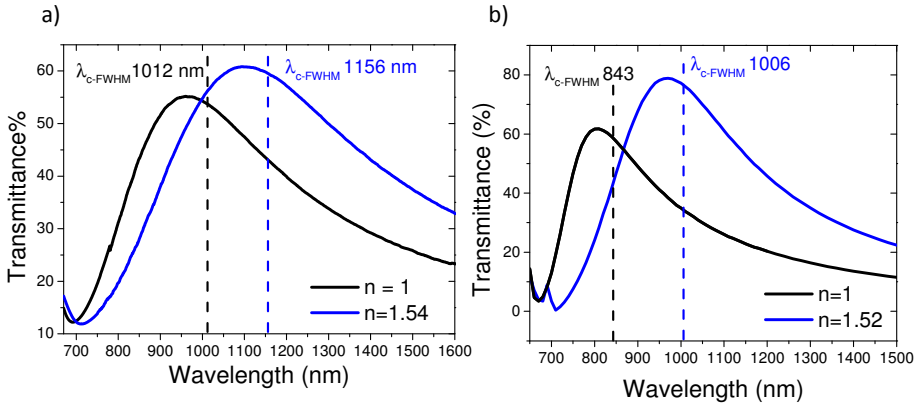

Figure 5.14: a) EOT spectrum of the NHA in air (dark grey line) and covered with NOA-61 (blue line);b)Simulated EOT spectrum of the NHA in air (black curve) and covered with a dielectric film with n=1.52 (blue curve). The dash lines indicates the position of the centroid at FWHM of each peak.

and, it is 1067 nm after the NOA-61 coverage. The fit was done in the wavelength range 820-2600 nm for the sample in air and in the range 920-2600 nm for the sample in NOA-61. x_0 was red-shifted of 160 nm, as reported in figure 5.15. In the case of simulated spectra the x_0 was red-shifted from 740 nm ($n = 1$) to 927 nm ($n = 1.52$) for a bulk refractive index variation of 0.52. The bulk sensitivity referred to the Fano parameter (x_0) can be calculated as:

$$S^{x_0}_{bulk-exp} = \frac{\Delta x_0}{n_{NOA} - n_{air}} = \frac{160}{0.54} = 296\, nm \cdot RIU^{-1} \tag{5.19}$$

$$S^{x_0}_{bulk-theor} = \frac{\Delta x_0}{n_{1.52} - n_{air}} = \frac{187}{0.52} = 360\, nm \cdot RIU^{-1}. \tag{5.20}$$

5.3.4 Discussion

The experimental and theoretical response of the NHA to refractive index changes was analyzed by two methods. The very good agreement between the Fano Resonance and the experimental and simulated EOT spectra indicates that it is an appropriate model to explain and investigate our results. Moreover, the sensitivity values obtained by monitoring the Fano parameter x_0 are higher with respect to those obtained by the centroid method. As already observed, this can be explained considering that the Fano Resonance analysis involves a fit of the entire EOT peak whereas the centroid method considers only the

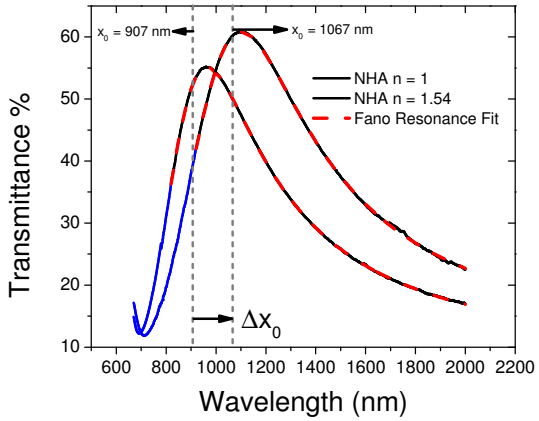

Figure 5.15: a) Experimental EOT spectrum of the NHA in air (n=1) and covered with NOA-61 (N01.54) fitted with the Fano Resonance Model (the fit is indicated by red dash lines.) The blue part of the spectra was not included in the fit calculation.

asymmetry of the curve. These results show that the analysis of x_0 is a more sophisticated and complete way to analyze the EOT response.

In order to evaluate the results obtained we calculated the decay length of the electromagnetic field (l_d) along the perpendicular direction to the NHA interface.

l_d can be derived by the ratio $2S_{bulk}/S_0$ from equation 5.10. We used the experimental values of $S_0^{x_0}$ (4.2 RIU^{-1}) and $S_{bulk}^{x_0}$ (296 nm $\cdot$ RIU^{-1}) and we obtained aneffective value of l_d = 140 nm, whose order of magnitude is in qualitative agreement with the simulated value of 106±6 nm. Concerning the comparison between the model and the experimental case, we think that the differences could be due to the presence of defects and to the smoothed geometry of the holes in the real samples. We underline that the experimental bulk sensitivity obtained in the present work is in perfect agreement with similar results on EOT-based sensors found in literature, which reports values of S_{bulk} of about 300 nm RIU^{-1} in the visible-NIR range. [2] We can conclude that a good level of agreement was found between the local and bulk sensitivity of theoretical model and experimental data and that, the Fano Resonance model can be considered the best approach to analyze and discuss our results.

5.4 Biological sensing with NHA

The biosensing response of NHA was investigated by using a couple of biological molecules based on the receptor-ligand scheme. The molecules are biotin-streptavidin, the same

involved in the sensing tests of Au:Ag SNSA and Ag NPA. We applied the same functionalization strategy in order to compare the sensing performances of all the nanoarrays investigated. The intrinsic properties of the biomolecules involved, the functionalization and other experimental parameters are known to strongly affect the performances of the SPR-based sensors. [93]

5.4.1 NHA synthesis

The nano-holes arrays for biological tests were synthesized in spots 2 millimeters in diameter, on a silica substrate. To synthesize exactly an area of 3.14 mm^2 we used dedicated home-made masks (see figure 5.16a). The masks were positioned on the etched PS monolayers before the metals deposition. After the multilayer deposition we removed the masks and we obtained a sample as reported in figure 5.16b. The metal was deposited on the PS monolayers only in the circular area exposed to the atoms flux. The four circular spots are the PS monolayers covered with the multilayer Ti-Ag-Au while, the iridescence zone, is only the PS monolayer. Following the metals deposition, the sample was treated in toluene in ultrasound bath for few minutes to remove the polystyrene monolayer not covered with the metals, as in figure 5.16c. The typical morphology before and after the toluene treatment can be seen in the SEM images in cross view in figure 5.17. Toluene was used to dissolve the polystyrene nanoparticles and to obtain the ordered nano-holes array. This procedure allows to obtain Ti-Ag-Au NHA in spots 2 mm in diameter (see figure 5.16c).

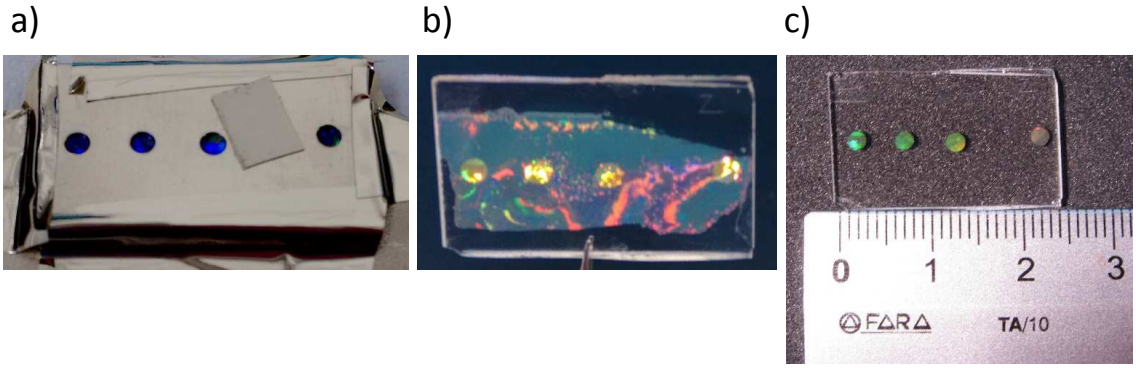

Figure 5.16: a) Etched PS monolayers covered with a home-made mask (spots diameter 2 mm) after the Ti-Ag-Au deposition; b) Sample after the removal of the home-made mask (the metal multilayer was deposited only in the circles); c) NHA samples on a silica substrate after the dissolution of the PS monolayer in toluene.

5.4.2 NHA characterization

The synthesized NHA have a period of a=522 nm ± 12 nm, a hole diameter of d=280 ± 10 nm and a total metal height of 60 ± 3 nm. The nanoholes hexagonal periodicity, the hole diameter and the multilayer morphology can be observed in figure 5.18.

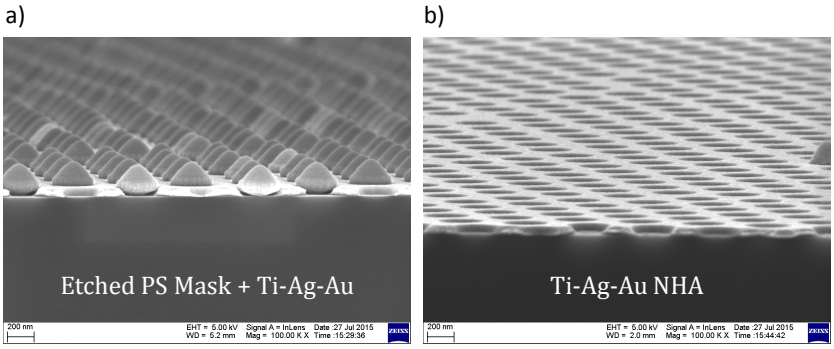

Figure 5.17: a) SEM image in side view at 100.00 KX of the sample before the toluene treatment; b) SEM image after the polystyrene dissolution in toluene.

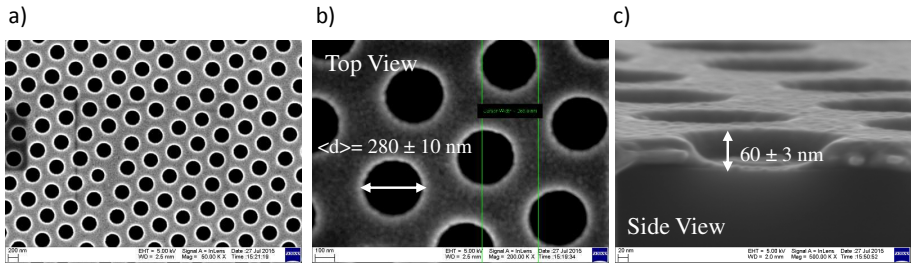

Figure 5.18: a)SEM image at 50.00 KX of a NHA with period 522 ± 12 nm, hole diameter d 280 nm ± 10 nm in a Ti-Ag-Au film with thickness 60 ± 3 nm; b) SEM image at 100.00 KX ; c) Cross view at 500.00 KX.

The transmission spectra were acquired on the spots by using a dedicated home-made sample-holder with a circular aperture of 2.3 mm in diameter. EOT spectrum of the NHA presents the (1,1) peak at $\lambda_{EOT}(1,1) \sim 560$ nm and the (1,0) peak in the NIR region at $\lambda_{EOT}(1,0) \sim 970$ nm, as reported in figure 5.19.

5.4.3 Bio-functionalization of NHA

The EOT biosensing performances were investigated by using the biotin-streptavidin couple. The functionalization strategy is the same used in the case of SNSA and NPA. Biotin

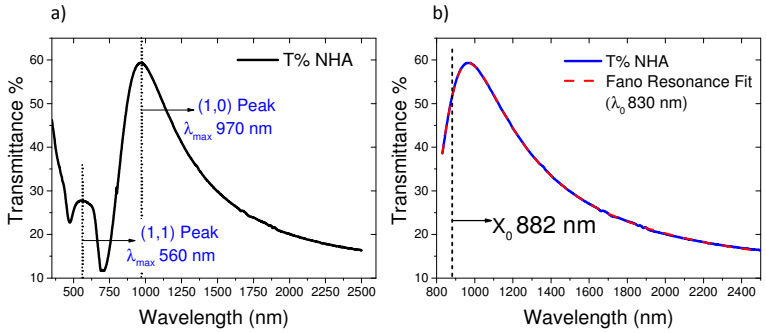

Figure 5.19: a) EOT spectra of Ti-Ag-Au NHA, the λ_{max} of the peaks are indicated by dot lines; b) analysis of the (1,0) peak with the Fano Resonance model form 830 to 2600 nm, x_0 is at 882 nm.

is the receptor which binds streptavidin, the analyte, in one of the strongest interactions found in nature. This couple of molecules is the most widely used for biosensing tests. The protocol details and the biotin and streptavidin characteristics are exhaustively explained in the chapter 3. The steps of the applied protocol can be summarized as follow:

1. functionalization of NHA with a solution 1 mM **11-MUA:1-OCT** (2:3) in ethanol 24 h;
2. washing treatment with ethanol and drying by N_2 flux;
3. functionalization of NHA with 1 mM **Biotin-PEG$_2$-NH$_2$** in 10 mM PBS + 10 Mm EDC 1-2 hours;
4. washing treatment at first with 10 mM PBS and then with milli-Q water, drying by N_2 flux;
5. functionalization with $10^{-15} \leq [\mathbf{SA}] \leq 10^{-5}$ M in 10 mM PBS 1-2 hours;
6. washing treatment at first with 10 mM PBS and then with milli-Q water, drying by N_2 flux.

11-MUA, 1-OCT, ethanol, PBS, EDC and Streptavidin were purchased from Sigma-Aldrich. EZ-Link Biotin-PEG$_2$-NH$_2$ was purchased from Thermo Fisher Scientific Inc. in form of powder. At the third step of the protocol, the NHA functionalized with thiols and biotin can be nominally considered a specific nanosensors for the streptavidin detection. The NHA sensing behavior was interrogated by measuring the EOT response as a function of the streptavidin molar concentration, $[SA]$.

The nanoholes arrays expose a Ti-Ag-Au surface area of $3.02 \cdot 10^{12}$ nm^2 in a spot of 2 mm in diameter. This value was calculated considering the top surface and the inner walls of the

holes. We have calculated the maximum number of thiol, receptor and analyte molecules which can bind to the NHA spots. Taking into account the footprint of a single alkylthiol chain on a flat gold surface (0.214 nm^2), the maximum number of thiols which can be immobilized on one spot is $1.41\times\ 10^{13}$ mol/spot.
In the first step of the protocol the samples were functionalized with a solution composed by 11-MUA:1-OCT (at a volume ratio of 2:3) 1mM in ethanol for 24 h. Then, the samples were washed with some ml of ethanol and dried in N_2 flux. The washing treatment was important to remove the unbounded molecules present on the NHA's surface. It is known that thiols spontaneously form a compact monolayer on a gold surface for the high affinity between sulphur and gold atoms, which results in a covalent S-Au bond. This layer has the function to protect the surface from a-specific binding and it provides the -COOH group, which derives from the 11-MUA, necessary to bind the receptor biotin. The maximum number of 11-MUA is 2/5 of $1.41\times\ 10^{13}$ mol/spot, i.e., $5.65\times\ 10^{12}$ mol/spot. For this functionalization we used a macroscopic volume of 3 ml for each sample. The 1 mM thiol solution contains a number of molecules about 5 orders of magnitude higher with respect to the calculated saturation. To bind the receptor we used EZ-Link Biotin-PEG_2-NH_2 containing a polyethylene glycol (PEG) spacer arm and a terminal primary amine for conjugation via EDC. This biotin compound is water soluble and the solvent used in this case is a PBS solution 10mM in water. For the functionalization with the receptor we prepared a solution of Biotin-PEG_2-NH_2 1mM in PBS 10mM and we added EDC to obtain a concentration 10 mM. On each spot we deposited 20 μL of this solution to bind the receptor on the NHA's surface by the formation of an amide bond between -NH_2 and -COOH groups. A drop of 20 μL contains $1.2\cdot\ 10^{16}$ Biotin-PEO_2-NH_2 molecules, which can bind only to the 11-MUA by the EDC-mediated cross-linking reaction between -COOH and -NH_2 group. This volume assures a number of receptors about 3 orders of magnitude higher with respect to the 11-MUA saturation ($1.2\cdot\ 10^{16}$ biotin molecules vs $5.65\cdot\ 10^{12}$ 11-MUA molecules). After the functionalization with biotin, the samples were rinsed at first with PBS 10 mM to remove unbounded molecules and then with milli-Q water to remove residual PBS traces.

At this point of the protocol our NHA can be considered a specific nanosensor for streptavidin detection. Specific sensors are a class of devices which contain a receptor characterized by a very high affinity for the analyte of interest. We have exposed the nanosensors to different concentrations of streptavidin in the range $10^{-15} \leq [SA] \leq 10^{-5}$ M in PBS 10

mM. For this functionalization we used drops of 10 μL for each NHA spot. Assuming a 100% efficiency of the cross-coupling reaction and a binding 1:1 biotin-streptavidin, only the drops at streptavidin concentration 10^{-5} and 10^{-6} M contain a number of molecules to saturate the receptor sites. The number of molecules for each [SA] is reported in table 5.2.

5.4.4 EOT sensing response

Refractive index of molecules layer

EOT spectra were measured before and after each functionalization step. We expected a red-shift of the EOT for the refractive index change due to the molecules immobilization. The refractive index of the molecules layer can be represented by the Cauchy model as [104]:

$$n(\lambda) = A + \frac{B}{\lambda^2} + \frac{C}{\lambda^4} + \dots \tag{5.21}$$

The Cauchy equation is an empirical formula that quantifies the dependence of the refractive index of a material on the wavelength. Usually the first two terms are enough for a quantitative agreement with experimental values. This model describe materials with a dielectric behavior that is mainly refractive and negligibly absorptive, such as for small organic molecules. A layer of molecules has a refractive index of ~ 1.5.

[SA] M	**SA molecules/10μL**
1×10^{-5}	6.022×10^{13}
1×10^{-6}	6.022×10^{12}
1×10^{-7}	6.022×10^{11}
1×10^{-8}	6.022×10^{10}
1×10^{-9}	6.022×10^{09}
1×10^{-10}	6.022×10^{08}

Table 5.2: Number of Streptavidin molecules for each concentration in a drop of 10 μL.

5.4.5 EOT analysis before and after the biofunctionalization

For the analysis of the EOT spectra we monitored the evolution of the Fano parameter x_0. As discussed in the previous section, we found that the Fano Resonance fit is the best method to analyze the EOT variations for refractive index changes. For each step of the biofunctionalization an incremental Δx_0 was observed, as shown in figure 5.20. The x_0

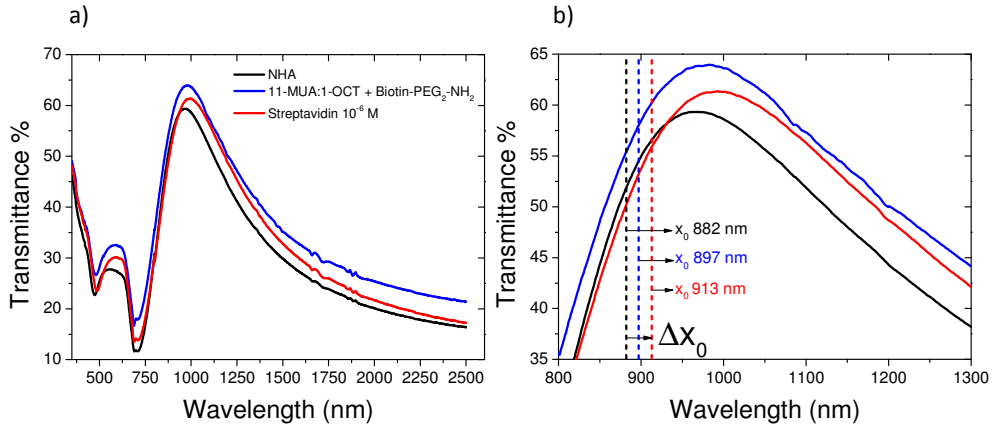

Figure 5.20: a) EOT spectra of NHA before functionalization (black curve), after functionalization with 11-MUA:1-OCT (2:3) and Biotin-PEO_2-NH_2 (blue curve) and after the exposure to Streptavidin 10^{-6} M (red curve); B) zoom of graph a. The dash lines indicates the x_0 red-shift after each step.

parameter exhibits a red-shift of +15±1 nm after the immobilization of 11-MUA:1-OCT (2:3) and Biotin-PEO_2-NH_2. This EOT response indicates the successful binding of the thiols and the receptor layer. After the exposure to streptavidin 10^{-6} M, x_0 is red-shifted by a further +15±1 nm. This streptavidin concentration saturates all the available receptor sites; the red-shift of +16 nm corresponds to the saturation value of the EOT response for our density of receptors. The Fano Resonance fit was done above the inflection point of the

Step	x_0 **(nm)**	Δx_0 **(nm)**
As dep.	882	-
11-MUA:1-OCT + Biotin	897	+ 15
Streptavidin 10^{-6} M	913	+ 16

Table 5.3: x_0 parameter of NHA before and after the bio-functionalization.

(1,0) peak, in the λ range 810-850 nm every 5 nm up to 2500 nm. The reported x_0 value is the average of 9 fits of each curve and the associated error is the standard deviation.

5.4.6 Measurements of the biomolecules thickness by ellipsometry

To evaluate the expected EOT shift after the molecules immobilization we measured the thickness of the molecules layers on a planar surface. We deposited a film of Ti-Ag-Au (total thickness 60 nm) on a silicon substrate previously cleaned with an acid piranha solution. The thickness of Ti-Ag-Au was measured by AFM. We applied the same functionalization strategy and we acquired the ellipsometric measurements after each step of the protocol. The measured were acquired in the wavelength range of 300-1700 nm every 10 nm, with incidence angles in the range 65-75° every 5°. The data were analyzed by using the experimental dielectric function of the silicon substrate and the experimental $\varepsilon_{Ti-Ag-Au}$, as previously described. The molecules refractive index was approximated by the Cauchy Model. After the functionalization with 11-MUA:1-OCT 2:3 and biotin we measured a Cauchy layer of 1.6 nm. Then, after the exposure to streptavidin 10^{-6} M we measured a total Cauchy thickness of 3.9 nm. Considering the experimental local sensitivity obtained with the Fano analysis, reported in eq. 5.13, and a Δn variation of 0.45, we expected a x_0 red-shift of +3.4 nm after the thiols and biotin immobilization and of +4.8 nm after the exposure to an excess of streptavidin. The EOT red-shift measured is + 15 nm after the thiols and biotin immobilization and + 16 nm after an excess of streptavidin. This difference can be mainly due to the morphology of the surface; the effective Cauchy thickness measured on a planar surface is not the same for a more complex morphology such as the NHA. However, the ellipsometric measurements were useful to confirm the protocol efficiency.

5.4.7 Discussion of the EOT response vs [SA]

The Δx_0 values as a function of $[SA]$ are reported in table 5.3. We observed that for very low concentrations of the analyte the Δx_0 values exhibited a small blue-shift. We have to take into account that in these solutions the streptavidin concentration is very low with respect to the solvent (10^{-15}<[SA]<10^{-13} M vs [PBS] $\sim 10^{-2}$ M). In these cases the dominant effect on the pre-functionalized nanoarrays seems to come from the solvent. We suppose that this effect is present in all the samples but it is less and less visible as the analyte concentration increases: in this case, the increasing number of the receptor-analyte biorecognition events, which cause a red-shift of the peak, compensates, first, and then overcomes the solvent-induced blue-shift. Therefore, the final EOT shift is the com-

[SA] M	Δx_0 **(nm)**	Δx_0 - $\Delta x_{0,noSA}$ **(nm)**	σ **(nm)**
10^{-15}	- 10	0	1
10^{-13}	- 10	0	1
10^{-10}	- 4	+ 6	1
10^{-09}	- 1	+ 9	1
10^{-08}	+ 1	+ 11	1
10^{-07}	+ 4	+ 14	1
10^{-06}	+ 15	+ 25	1
10^{-05}	+ 15	+ 25	1

Table 5.4: EOT shift for different concentrations of Streptavidin.

bination of these two opposite effects. For this reason, to properly quantify the effect of increasing amounts of analyte and normalize for the solvent effect, we considered a reasonable approach to subtract the $\Delta x_{0,noSA}$ measured with null streptavidin concentration ([SA] $< 10^{-15}$ M), from the Δx_0 response. Therefore, we define the compensated EOT response as $\Delta x_{0,comp}$, which is equal to:

$$\Delta x_{0,comp} = \Delta x_0 - \Delta x_{0,noSA} \tag{5.22}$$

The values of $\Delta x_{0,com}$ are reported in the third column in table 5.3. The EOT response curve can be defined as $\Delta x_{0,comp}$ as a function $[SA]$, and the results are shown in figure 5.21. The model widely used in literature to analyze the sensing response of SPR-based sensors is the Langmuir Isotherm [73], which is described by:

$$\Delta R = \Delta R_{sat} \frac{K_{a,eff} \cdot [SA]}{1 + K_{a,eff} \cdot [SA]} \tag{5.23}$$

where ΔR_{sat} is the saturation value of the SPR response (ΔR) and $K_{a,eff}$ is the "effective affinity constant" of the receptor-analyte couple at the interface. An adsorption process can be represented by the Langmuir Isotherm if these hypothesis are satisfied:

1. all the adsorption sites are energetically equivalents;
2. each site can bind only one molecule;

3. the bound molecules do not interact among them.

The two last hypothesis are satisfied by the 11-MUA dilution and, as a consequence, the receptor dilution on the NHA's surface. We suppose that one streptavidin can bind only to one biotin. Nevertheless, in our NHA samples, hypothesis 1 for the validity of Langmuir analysis is not granted since we have two remarkably different surface morphologies: (i) the flat surface of the NHA and (ii) the more rough surface internal to the nanoholes. Our experimental data of the sensitivity curve apparently do not exhibit a simple Langmuir behaviour. Considering the above mentioned two possible surface configuration, we suppose that the biotin-streptavidin binding on the NHA's surface follows a kinetic based on two steps, i.e., the receptor sites on the top surface and those in the inner walls of the nanoholes can not be considered as sites with the same characteristic energy for the binding. Thus, we used a modified model of the Langmuir Isotherm described by two processes as a funtion of $[SA]$, described by:

$$\Delta x_{0,comp} = \Delta x_{0,comp,sat_1} \frac{K_{a1,eff} \cdot [SA]}{1 + K_{a1,eff} \cdot [SA]} + \Delta x_{0,comp,sat_2} \frac{K_{a2,eff} \cdot [SA]}{1 + K_{a2,eff} \cdot [SA]} \tag{5.24}$$

The experimental values are better represented by the proposed double Langmuir model, as can be seen in figure 5.21. The $K_{a,eff}$ and the Limit Of Detection (LOD) of the biomolecules under study can be measured from the response curve. The first kinetic process shows a saturation value $\Delta x_{0,comp,sat_1}$ of 10 $\pm$ 1 nm and a $K_{a1,eff}$ of 1.6 $\pm$ 0.9 $\cdot$ 10^{10} M. This process prevails for concentrations $[SA]$ about 10^{-9}-10^{-3} times lower than the available receptor sites. When the analyte in solution is 0.01-10 times the available biotin molecules on the NHA, $\Delta x_{0,comp,sat_2}$ is 17 $\pm$ 1 nm and $K_{a2,eff}$ is 4.8 $\pm$ 1.8 $\cdot$ 10^6 M. The measured $K_{a,eff.}$ are lower than the K_a referred to binding events in solution ($10^{15} \leq K_a \leq 10^{13}$ M). This is expected for the differences of a bio-recognition event in solution with respect to a solid-liquid interface, in which the receptor is immobilized on a surface. [75] The adsorption of streptavidin on the biotinylated-NHA can be strongly affected by many parameters such as the biotin concentration, the ratio between the receptor and the spacer, the type of the spacer, the morphology of the surface and the solution properties (such as pH or temperature). All of them can influence the bio-recognition event.

The LOD can be estimated as the abscissa of the intersection point between the confidence interval associated with the null-response point (no streptavidin) and the sensing curve, as shown in figure 5.21. The LOD obtained is 10^{-11} M. This value is comparable to

that obtained with high interacting SNSA. The saturation response of NHA is lower with respect to the interacting SNSA,which are described in chapter 4. This is due to the different properties of the SPP in the propagating (NHA) or localized (SNSA) case. The electric field decay length of the localized SP (l_d) is one order of magnitude lower with respect to l_d of the propagating SPP. This means that the local sensitivity ($S_0 = 2\ S_{bulk}/l_d$) of SNSA is higher with respect to NHA, in particular in the interacting case for the coupling effects. SNSAs are intrinsically optimized to measure thin layer of molecules, while NHAs are particularly useful to measure bigger molecules such as viruses or bacteria.

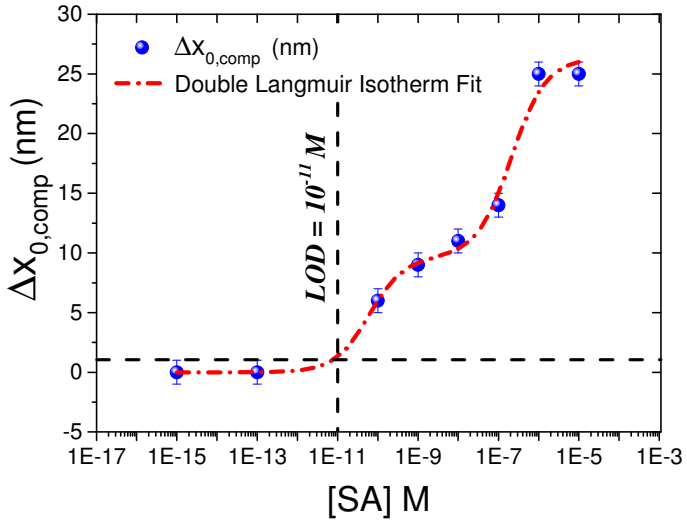

Figure 5.21: Experimental response curves of Δx_0 versus $[SA]$ for the binding of Streptavidin to NHA pre-functionalized with Biotin. The solid line is the calculated value of Δx_0-$\Delta x_{0,noSA}$ using a modified Langmuir Isotherm described in equation 5.24.

5.4.8 Aspecific test with Bovine Serum Albumine (BSA)

To investigate the specificity of our sensors we used another strategy of biofunctionalization. After the immobilization of thiols and biotin, we exposed the NHA to a solution of BSA at concentration 1mg/ml, which corresponds to 1.5×10^{-5} M. BSA is a protein with MW similar to that of the streptavidin, for this reason it is widely used to investigate the presence of aspecific binding on the biotinylated-surfaces. The BSA concentration is very high; all the biotinylated-NHA were exposed to a protein solution containing a number of molecules in excess with respect to the maximum number of biotin available on the

$[SA]$ M	Δx_0 (nm)	Δx_0 - $\Delta x_{0,noSA}$ (nm)	σ (nm)
10^{-15}	- 6	0	1
10^{-13}	- 6	0	1
2×10^{-09}	+ 3	+ 9	1
2×10^{-08}	+ 4	+ 10	1
2×10^{-07}	+ 7	+ 13	1
5×10^{-07}	+ 11	+ 18	1
2×10^{-06}	+ 10	+ 16	1
1.67×10^{-05}	+ 13	+ 19	1

Table 5.5: EOT shift for different concentrations of Streptavidin.

NHA. Following the exposure to BSA, the NHA were incubated with streptavidin in the concentration range $10^{-15} \leq [SA] \leq 10^{-5}$ M. The EOT response was analyzed with the model of the Fano Resonance as for the previous experiment. The results are presented in table 5.5. The first saturation value of $\Delta x_{0,comp,sat_1}$ is 9 ± 1 nm and a $K_{a1,eff}$ of (4 ± 3)

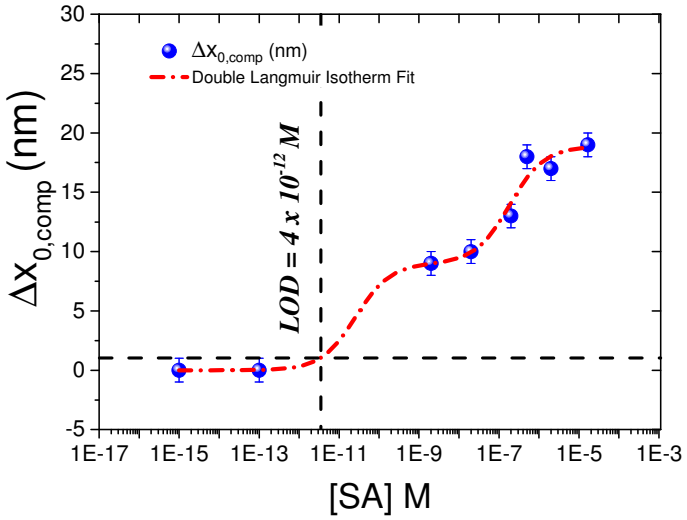

Figure 5.22: Experimental response curves of $\Delta x_{0,comp}$ versus $[SA]$ for the binding of Streptavidin to NHA pre-functionalized with Biotin and exposed to BSA 1.5 $\times$ 10^{-5} M. The solid line is the calculated value of $\Delta x_{0,noSA}$ by using the modified Langmuir Isotherm described in equation 5.24.

$\cdot$ 10^{10} M. $\Delta x_{0,comp,sat_2}$ results in 10 ± 1 nm, and $K_{a2,eff}$ is 5.4 ± 2.3 $\cdot$ 10^6 M. The LOD can be estimated as 4 $\times$ 10^{-12} M. The saturation response and the LOD show that the

sensing performances are reduced by the previous exposure of the nanosensor to the high concentration of BSA. This is a clear indication that we need to increase the protection of the NHA's surface from aspecific binding. Biotin-poly(ethyleneglycol)$_n$amine with higher n values are the best candidates to overcome this problem. PEG is known as the best molecule to protect the sensor's surfaces from the common aspecific events which can alter the sensing performances. The PEG_2 presents in the molecule we used is apparently not sufficiently efficient to protect the surface from BSA binding.

5.4.9 Conclusions

We have synthesized ordered arrays of nanoholes to study their sensing performances to refractive index changes. The following conclusions can be drawn from the above analysis on NHA performances:

- The variation of the EOT spectrum was investigated with two different approaches.
- The Fano Resonance Model was found the best method to analyze the EOT variations.
- The experimental and theoretical bulk sensitivity is comparable to the values reported in literature.
- The comparison between our experimental and simulated sensitivity is in a good level of agreement, by taking into account the differences between the real and ideal samples.
- The label-free biosensing performances were investigated by using the biotin-streptavidin couple.
- The LOD obtained is comparable to that of interacting SNSA described in the chapter 4.
- The EOT saturation response is lower with respect to the LSPR saturation signal of interacting SNSA.This is in agreement with the amplified local sensitivity of SNSA.
- Biotinylated-NHA demonstrated a proportional EOT response as a function of the streptavidin concentration but, the following test with BSA indicated that there is the need to further protect the surface from aspecific binding events by including a dedicated PEG functionalization step.

6 Ag NPA: Ag oxidation effects on SERS response

6.1 Introduction

Surface Enhanced Raman Scattering (SERS) is one of the most widely used plasmon enhanced spectroscopies. [105] Due to the very strong amplification of the optical signal achievable on the surface of nanostructured metal substrates, SERS has been successfully used as an analytical technique for the identification of chemical and biological species at trace concentration or even at single molecule level. [106, 107] Moreover, SERS has been extensively employed to quantify the local electromagnetic field enhancement induced by plasmonic nanostructures [108–111] and, in a limited number of cases, to identify its spectral dependence. [112–115] The most common materials used to fabricate SERS substrates are noble metals, mainly gold and silver, owing to their optimal plasmonic properties in the visible and near-infrared (NIR) range. [116] Silver is probably the most efficient metal in the visible, but its tendency to oxidation can represent a major drawback in its use as plasmonic substrate. Physical and chemical modifications of the surface of a silver layer indeed can alter the Raman signal scattered from a molecule lying on it, either by affecting the electromagnetic and chemical contribution to the Raman scattering or by changing the affinity with the molecule. To the best of our knowledge, this subject has been only investigated in few papers [117, 118] and it is still rather unexplored. In Ref. [[117]], Erol and co-workers reported that the detection limit of nitro-aromatic compounds can be lowered by several orders of magnitude if the silver substrate is oxidized under ambient conditions. In Ref. [[118]] instead, Han and co-authors showed that that ozone induced oxidation of silver nanoparticles immobilized on glass leads very quickly to a drastic deterioration of the SERS response from either trans-1,2-Bis(4-pyridyl)ethylene (BPE) or isothiocyanate. Aim of the present work is to address the role of oxidation on the SERS response of a

peculiar class of silver substrates constituted by nanoprism arrays (NPA) synthesized by nanosphere lithography. [52,119] Due to their strong local-field enhancement effects and the wide tunability of their plasmonic resonances from the visible to the NIR, these nanosystems represent a very versatile and highly performing kind of nanostructured substrates, with applications in many different fields in nanophotonics, non-linear optics and sensing. [57,120,121]
In the present work a complete characterization of the oxidation effects on the SERS properties of these nanosystems was carried out employing the so-called wavelength-scanned SERS (ws-SERS) technique [112] in which the SERS enhancement factor (EF) was measured at several excitation wavelengths tuned around the dipolar surface plasmon resonance (SPR) peak of the nanoprism arrays. The experimental results were combined to those obtained by finite element method (FEM) simulations. With this approach it was possible to determine the absolute values of the EF factors decoupling the effects that control the maximum EF values from those related to spectral shifts of the field enhancement dispersion.

6.2 Experimental section

6.2.1 Structural and optical characterizations

The synthesized nanoprism arrays were characterized morphologically by scanning electron microscopy with a Zeiss SIGMA HD field-emission scanning electron microscope (FE-SEM) operated at 2 kV, with secondary electrons detector. Atomic force microscopy (AFM) measurements were performed using a NT-MDT Solver PRO-M AFM microscope with a 100 $\times$ 100 μm scanner, operated in semi-contact mode. Optical extinction spectra were collected with a JASCO V670 dual beam spectrophotometer. The Ag dielectric function was experimentally determined by ellipsometry measurements performed on continuous films evaporated under the same conditions as those used for the NPAs, using a J. Woolham V-VASE Spectroscopic Ellipsometer.

6.2.2 Synthesis of nanoprism arrays (NPAs)

2D ordered arrays of silver nanoprisms were synthesized by nanosphere lithography (NSL). [52,119,120] First, a colloidal monolayer of polystyrene (PS) nanospheres was self-assembled on the surface of a glass substrate according to the method proposed by Giersig and co-workers. [69] Commercial PS nanospheres (Microparticles GmbH) with a nominal diameter $D = 470$ nm were used. All the substrates were previously cleaned in a "piranha" solution (H_2SO_4:H_2O_2, 3:1) for 1 hour at 90 °C, rinsed in ultra-pure deionized water and let dry in air for half an hour. This procedure yields large areas (of the order of some cm^2) of patterned substrates. The typical area of the ordered domains of the 2D crystalline monolayer extends up to several hundreds of μm^2. After the formation of the colloidal monolayer, silver was thermally evaporated on the samples in orthogonal geometry to form the plasmonic nanoprism arrays.

Ag evaporations were performed at a pressure of 5×10^{-5} mbar with a current of 30 A. The evaporation time was shorter than 300 s. We checked that such conditions do not induce overheating of the PS nanospheres.

A calibrated quartz microbalance was used to control the thickness of the evaporated Ag layer (about 100 nm). After the evaporations, the PS nanospheres were mechanically removed by stripping with an adhesive tape. The result of this procedure is an ordered array of triangular nanoprisms (NPA) arranged in a honeycomb lattice on the surface of the glass substrates, as shown in fig. 6.1(b). The LSPR spectrum of the samples before any treatment has a maximum around 687 nm, as reported in figure 6.1(a). The geometric parameters of the nanoprism array were measured by atomic force microscopy and scanning electron microscopy, and are: lattice parameter $a_0 = 470 \pm 10$ nm, nanoprisms distance $d = 270 \pm 6$ nm, nanoprisms side length $L = 150 \pm 3$ nm and height $h = 98 \pm 3$ nm. These parameters were used to define the unit cell for the finite elements method (FEM) simulations.

6.2.3 Samples functionalization

Three identical Ag NPAs (in the following named as S1-nOx, S2-mOx and S3-sOx) were synthesized and functionalized by immersion in a 10 mM solution of benzenethiol (BT) for 15 hours in environmental conditions. The choice of using a thiol terminated molecule

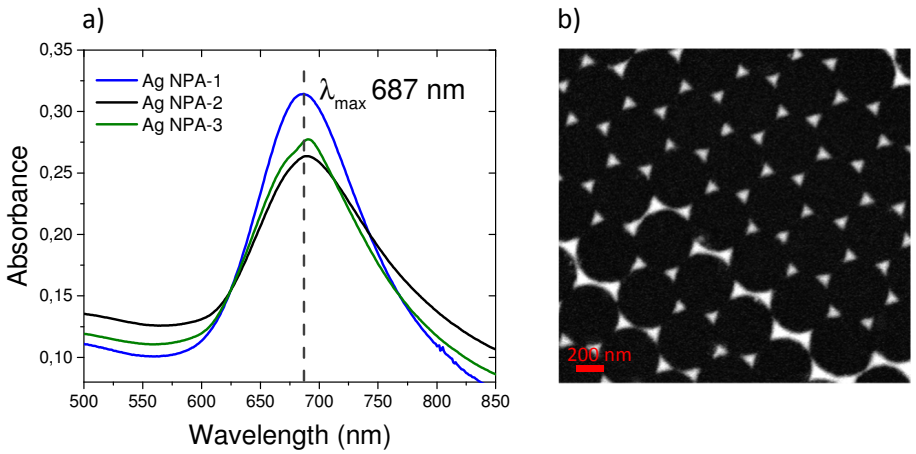

Figure 6.1: (a) Extinction spectra of three identical samples of Ag NPA; (b) SEM image of Ag NPA.

was aimed at reproducing a surface-molecule interaction that is very often encountered in SERS applications, since many analytes are functionalized with a thiol group in order to improve their affinity to the plasmonic substrate. In particular, to simulate the effect of a different degree of oxidation, sample S1-nOx was functionalized with BT immediately after the synthesis of the nanoprism array (not-oxidized sample), sample S2-mOx was exposed to air at room temperature for a week before functionalization (mildly oxidized sample), while sample S3-sOx was heated at 70°C in air for 30 minutes before BT functionalization (strongly oxidized sample). [122]

6.2.4 FEM simulations

Simulations of the linear optical properties (near-field and far-field) of the NPAs have been carried out using a commercial software for finite elements method (FEM) [123] computations (COMSOL Multiphysics, version 4.4), as already reported in previous works. [57,121] The nanoprism array was modeled by considering a rhombic unit cell (containing 2 nanoprisms) with side a_0 and by implementing periodic boundary conditions in the array plane ($\hat{xy}$). The incident field is described as a plane wave traveling downwards (towards the substrate) along the $\hat{z}$ axis, orthogonal to the prism triangular base plane, with polarization along the nanoprism center-to-center line. In the $\hat{z}$ direction the substrate is modeled as semi-infinite. The nanoprisms are placed directly on the substrate and the interface between substrate and the environment is at the $z = 0$ plane. To model the presence of the ben-

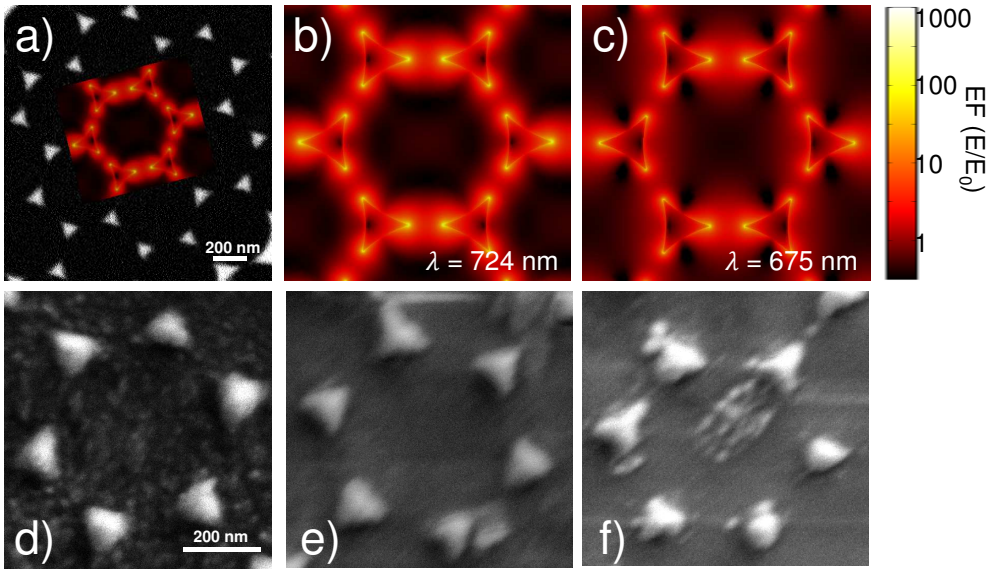

Figure 6.2: (a) SEM image of a silver nanoprisms array (sample S1-nOx). (b, c) Simulated maps of the local-field enhancement factor of sample S1-nOx at the two indicated wavelengths corresponding to the maximum of the simulated absorbance spectra estimated at the laser wavelength at the Raman wavelength for the 999 cm^{-1} band of benzenethiol. (d-f) Detail of a SEM image of the NPA in samples S1-nOx (not-oxidized), S2-mOx (mildly oxidized) and S3-sOx (strongly oxidized), respectively.

zenethiol monolayer, a conformal layer over the silver nanoprisms (thickness 2 nm, index of refraction $n = 1.59$, no absorption) was included in the simulations. Over the NPAs the environment (air) is semi-infinite. The semi-infinite conditions are necessary to hinder radiation back-scattering from the external boundaries and are provided by Perfectly Matched Layer sub-domains.

The electromagnetic simulation is carried out by solving the Helmholtz equation in the frequency domain. The material properties are described by its relative dielectric permittivity function $\varepsilon_r(\lambda)$. Magnetic effects are not considered, thus the relative magnetic permeability is $\mu_r = 1$. For silver, the experimental dielectric function determined by ellipsometric measurements was used, while the refractive index $n = 1.59$ used for benzenethiol was obtained from the supplier.

To describe the effect of oxidation, the model was modified adding a conformal layer (3 nm thick) of a mixture of silver oxide and benzenethiol on the surface of the silver nanoprisms, whose metallic volume was consequently reduced. The refractive index of the layer was set to the average value between the refractive index of silver oxide ($n = 2.5$ [124], [125]) and that of BT ($n = 1.59$). The side length of the modeled nanoprisms was also slightly

reduced to $L = 140$ nm, to account for the shape modifications due to oxidation.

6.2.5 SERS measurements

A home-made macro-Raman setup was used to carry out wavelength-scanned surface enhanced Raman spectroscopy measurements (ws-SERS). The system is equipped with a cw Ti:Sapphire laser tunable in the range 675-1000 nm (Spectra Physics, 3900S) pumped by a cw optically pumped semiconductor laser (Coherent, Verdi G7) and an Ar^+/Kr^+ gas laser (Coherent, Innova 70) providing the lines at 488, 514.5, 530.8, 568 and 647.1 nm.
The laser lines are filtered through a tunable laser plasma line filter (Laserspec III, Spectrolab) and focused on the sample by a cylindrical lens. The Raman scattering diffused by the sample is collected by a camera objective (CANON 50 mm f/1.2) and coupled into the slit of a three stage subtractive spectrograph (Jobin Yvon S3000) by means of a set of achromatic lenses. The spectrograph is composed of a double monochromator (Jobin Yvon, DHR 320) working as a tunable filter rejecting elastic scattering and a spectrograph (Jobin Yvon, HR 640).
The Raman signal is detected by a liquid nitrogen cooled CCD (Jobin Yvon, Symphony, 1024x256 pixels, front illuminated). A polarization scrambler is mounted right in front of the spectrograph slit. The system is configured in backscattering geometry by placing a tiny mirror in front of the collection objective to steer the beam from the cylindrical lens to the sample. The sample is mounted on a translation stage that allows to move it parallel and perpendicular with respect to the laser propagation direction.
SERS spectra and enhancement factors (EF_{SERS}) were measured in macro-Raman configuration, with a laser spot size of about 3 mm $\times$ 80 μm at the sample position. Such spot size is much larger than the one typically used in micro-Raman configuration (which is of the order of a few microns in diameter). The macro-Raman configuration was chosen in order to illuminate an area on the sample similar to the one involved in the measurement of the extinction spectra. Doing so, in both experiments a very large number of randomly oriented nanoprisms domains are illuminated and possible polarization effects are averaged out.
SERS enhancement factors were estimated following the standard procedure outlined by

Le Ru, [108] by making use of the following relation:

$$\mathrm{EF_{SERS}} = \frac{I^{SERS}}{I^{Raman}} \frac{C_V}{C_S} \frac{\eta}{A}, \tag{6.1}$$

where I^{SERS} is the integrated intensity of the 999 $\mathrm{cm^{-1}}$ band of benzenethiol (β_{CCC}) absorbed on the metal surface and I^{Raman} is the integrated intensity of the same band of liquid BT (β_{CCC}). [126] The band assignment is shown in parenthesis: β indicates the in-plane bending and consequently β_{CCC} corresponds to the so-called benzene *ring breathing mode*. C_S is the surface packing density of BT on a flat silver surface ($C_S = 6.80 \times 10^{14}$ molecules/$\mathrm{cm^2}$), C_V the number of molecules per unit volume of liquid BT ($C_V = 5.88 \times 10^{21}$ molecules/$\mathrm{cm^3}$), η is the axial collection efficiency of the experimental set-up (η was determined at every wavelength and was in the range 650-1400 μm) and A is a geometrical factor that accounts for the fraction of sample area that is covered with silver and therefore is SERS active (A was set to 0.2 for our samples, on the basis of their morphological parameters; $A = 1$ corresponds to a flat silver surface). The parameter η was determined by recording the Raman signal at 520 $\mathrm{cm^{-1}}$ of a silicon slab at several positions along the optical axis ($\hat{z}$). The trace was normalized to the maximum and fitted with a Lorentzian profile ($L(z)$) and η is defined as $\eta = \int_{-a}^{+a} L(z)\, dz$ where $2a$ is the thickness of the reference sample (in this case a 10 mm thick vial). For each sample, the Raman signal was recorded at 10 different points: the EF_{SERS} data and the corresponding error bars were defined as the average value and the standard deviation, respectively.

6.3 Results and discussion

Fig. 6.2a shows a SEM image of the Ag nanoprism array for the not-oxidized sample (S1-nOx). A detail of the NPA of the samples treated at the different oxidation conditions (not-oxidized, S1-nOx, mildly oxidized, S2-mOx and strongly oxidized, S3-sOx) is shown in panels (d-f). From the morphological point of view the images reveal that the oxidation process does not alter the honeycomb ordered arrangements of the nanoprisms. Only a slight reshaping of the nanotriangles is produced, which is more pronounced in the strongly oxidized sample (S3-sOx, fig. 6.2f) as a consequence of the annealing treatment.
In fig. 6.2b (and as inset in fig. 6.2a) and in fig. 6.2c, respectively, we reported the local-field enhancement maps obtained by FEM simulations of sample S1-nOx calculated at the

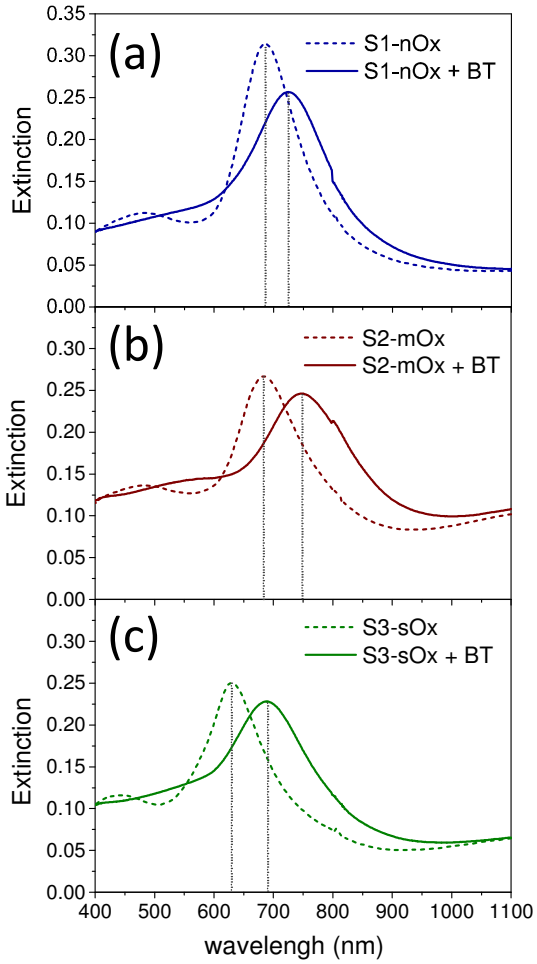

Figure 6.3: Extinction spectra of samples S1-nOx (a), S2-mOx (b) and S3-sOx (c) before (dashed lines) and after (solid lines) functionalization with benzenethiol.

wavelengths corresponding to the maxima of the simulated absorption spectra evaluated at the incident laser wavelength and at the Raman wavelength for the 999 cm^{-1} band of benzenethiol, as further discussed in detail in the text (see fig. 6.5a).
Intense hot-spots of the electromagnetic field are formed at the nanoprisms tips, which are further enhanced by the near-field coupling among the nanotriangles, with an enhancement of the modulus of the local electric field (normalized to the incident field, E_0) up to a factor 1000 estimated at the absorbance peak.

Fig. 6.3 shows the extinction spectra of the differently oxidized NPAs recorded before (dashed lines) and after (solid lines) functionalization with benzenethiol. Panels (a), (b) and (c) refer to samples S1-nOx, S2-mOx and S3-sOx, respectively. The spectral position of the extinction maxima measured before and after functionalization, and the correspond-

	Extinction			ws-SERS		
Samples	**Before** λ_{max}^{SPR} (nm)	**After** λ_{max}^{SPR} (nm)	$\Delta\lambda^{SPR}$ (nm)	EF_{SERS} $\times 10^6$	λ_{max}^{SERS} (nm)	$\Delta\lambda^{SERS}$ (nm)
S1-nOx	686	723	+37	4.5 ± 0.9	702	-21
S2-mOx	683	748	+65	1.8 ± 0.2	723	-25
S3-sOx	629	690	+61	2.1 ± 0.2	677	-13

Table 6.1: Maxima of extinction spectra before and after functionalization with benzenethiol, and of the EF_{SERS} profiles, for the three synthesized samples with different oxidation level (not-oxidized S1-nOx, mildly oxidized S2-mOx and strongly oxidized S3-sOx). $\Delta\lambda^{SPR}$ indicates the wavelength shift of the extinction maxima observed after functionalization with BT, while $\Delta\lambda^{SERS}$ is the spectral difference between the maximum in the EF_{SERS} profiles and the extinction peak of the functionalized samples.

ing wavelength shifts ($\Delta\lambda^{SPR}$), are summarized in Table 6.1. Concerning the samples not yet functionalized (dashed curves), the data show a blue-shift of about 55 nm of the extinction peak of sample S3-sOx (strongly oxidized by thermal treatment in air) with respect to samples S1-nOx and S2-mOx. This behavior can be understood taking into account that counteracting effects may occur in this sample: from one side the formation of an oxide layer on the surface of the nanoprisms is expected to red-shift the surface plasmon resonance due to the increase of the dielectric function, but on the other hand the reduced volume of metallic silver (due to surface oxidation), together with the reshaping of the nanoprisms due to the annealing treatment (as shown in fig. 6.2f), and in turn the diminished interaction between the nanoprisms, produce a blue-shift of the SPR peak, which resulted to be the dominant effect in this sample.

After functionalization with benzenethiol all the samples showed red-shifted extinction spectra (solid curves), and such an effect was more pronounced (by about a factor of 2) on the oxidized samples with respect to the not-oxidized one. These data indicate that benzenethiol effectively binds to the oxidized surface as it does to the metal surface. This finding is confirmed also in several studies in the literature. As an example, in Ref. [[127]] Himmelhaus and co-workers investigated by X-Ray Photoelectron Spectroscopy (XPS) the interaction of aliphatic thiols in ethanol solution with polycrystalline silver substrates possessing a native layer of oxide. The authors demonstrated that the aliphatic thiols can reduce the silver oxide leading to the formation of chemisorbed alkanethiolate. By studying the absorption rate as a function of the oxygen coverage on the surface by varying the

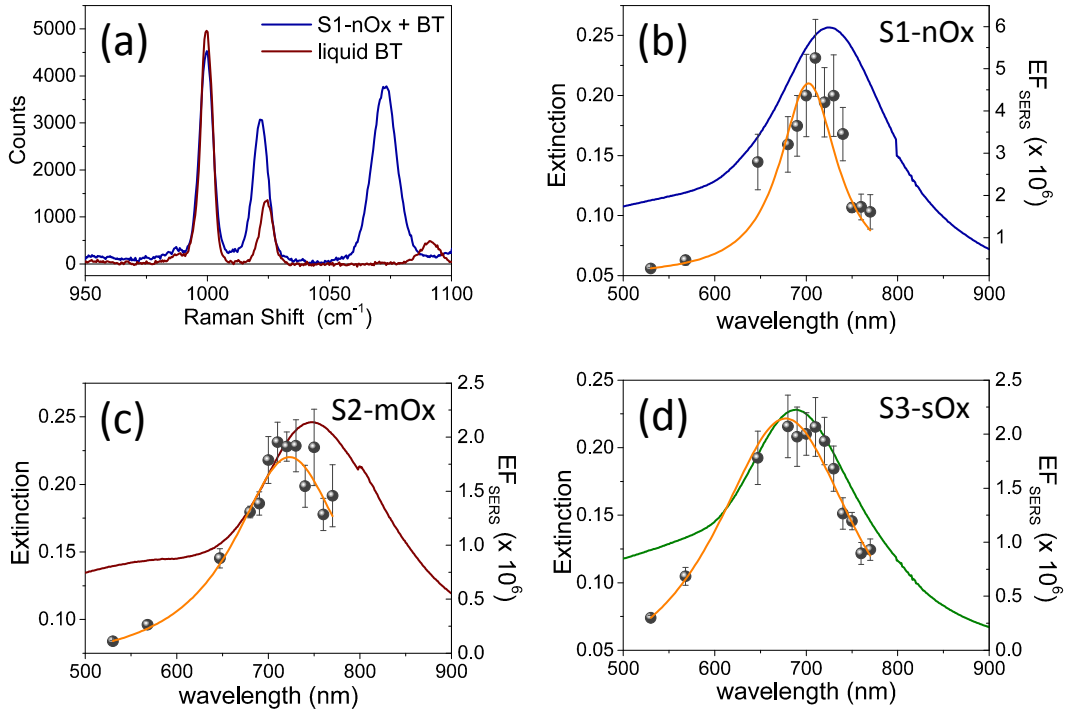

Figure 6.4: (a) Raman spectra of liquid BT (red) and BT absorbed on sample S1-nOx (blue); the spectra have been recorded with excitation at $\lambda_{exc} = 710$ nm under the same experimental conditions. (b), (c), (d) Extinction spectra (blue, red and green lines), experimental SERS enhancement factors (gray dots) and Lorentzian fit (orange line) of samples S1-nOx, S2-mOx and S3-sOx, respectively.

exposure time of fresh silver substrates to air prior to functionalization, they concluded that the higher is the amount of oxygen initially present, the higher is the absorption rate of thiol.

Furthermore, in Refs. [128, 129] Laibinis and co-authors proved that the immersion of a silver film with a thin layer of oxide in an alkylthiol solution leads to the almost complete displacement/reduction of oxygen and the formation of a self-assembled monolayer.

Fig. 6.4a shows a comparison between the Raman spectrum of liquid benzenethiol (red line) and of sample S1-nOx functionalized with BT (blue line). The spectra were recorded with laser excitation at $\lambda_L = 710$ nm, under the same experimental conditions. In order to calculate the SERS enhancement factor (EF_{SERS}), we referred to the $\Delta\omega = 999$ cm^{-1} band. In fig. 6.4b-d the ws-SERS data for the three differently oxidized samples, S1-nOx, S2-mOx and S3-sOx, are reported together with the corresponding experimental extinction spectra: the gray dots are the experimental EF_{SERS} values and the orange line is the Lorentzian fit to the EF_{SERS} data. The wavelengths at which the maximum EF_{SERS} is

measured (λ_{max}^{SERS}) and the corresponding value for the three samples are reported in Table 6.1.

$\Delta\lambda^{SERS}$ indicates the spectral difference between the maximum in the EF_{SERS} profiles and the extinction peak of the functionalized samples. The data show a blue-shift of the EF_{SERS} profile with respect to the extinction spectrum for all the three investigated samples.

This behavior can be understood considering that the SERS enhancement factor is proportional to the product $E^2(\lambda_L)\,E^2(\lambda_R)$, where $\lambda_R = (1/\lambda_L - \Delta\omega)^{-1}$ is the Raman shifted emission wavelength, and not merely to $E^4(\lambda_L)$. Since $\lambda_R > \lambda_L$, the EF_{SERS} peak occurs at a shorter wavelength if plotted against λ_L. This effect is well known and has been demonstrated experimentally in Ref. [112, 115].

Concerning the role of oxidization, first of all by comparing the results of sample S2-mOx (fig. 6.4c) with those of sample S1-nOx (fig. 6.4b), it emerges that the atmospheric oxidation gives rise to a spectral shift of the EF_{SERS} profile with respect to the extinction spectrum as in the not-oxidized sample (S1-nOx), but the maximum SERS enhancement factor results reduced by a factor of 2.5. Sample S3-sOx instead, with respect to S1-nOx, exhibits a smaller blue-shift of the EF_{SERS} profile, but a similar reduction of about a factor of 2.5 of the maximum enhancement factor as in sample S2-mOx.

To understand the observed difference in the maximum EF_{SERS} between fresh and oxidized samples, the effect of the presence of an oxide layer on the following factors has to be taken into account: (i) In calculating the experimental EF_{SERS} we assumed the same surface density for BT in all the samples, but the affinity of benzenethiol to metal and oxide in principle could be different. (ii) The strength of the chemical enhancement critically depends on the relative energy of the molecular orbitals and the metal (or oxide) bands, thus making it dependent on the detailed physical-chemical nature of the surface. (iii) The electromagnetic enhancement decreases steeply with the distance from the plasmonic material, therefore it can be affected by the possible presence of a dielectric layer acting as a spacer. (iv) The oxidation process slightly modifies the morphology of the substrates, as shown in fig. 6.2(d-f), and thus it can alter distribution and intensity of the electric field. Since these factors are not all in the direction of inducing a decrease of the SERS signal, their overall effect may cause no major drops in the enhancement factor but a more limited reduction, as experimentally observed.

Therefore, in order to completely unveil the role of the different parameters on the SERS

response, a deep analysis of the electrodynamic effects was performed by finite elements method (FEM) simulations. FEM simulations were used for the computation of the local-field distributions and the NPA far-field properties. It is worth noting that for the geometries obtained from FE-SEM and AFM characterizations, the maximum of the calculated extinction is coincident with that of the simulated absorption. This confirms that we can use the experimentally measured extinction maximum as representative of the experimental absorption maximum of the samples. The SERS enhancement factor (EF_{SERS}) was calculated by using the local-field distribution inside the volume of the analyte layer (BT) both for excitation and Raman shifted emission frequencies. A sketch of the local-field distribution at the wavelength of the maximum of the simulated absorbance spectrum and at the corresponding Raman shifted wavelength ($\Delta\omega = 999$ cm^{-1}) is given in fig. 6.2(b,c), respectively. Inside the active layer the local SERS enhancement factor has been computed as a function of the local electric field $\mathbf{E}(\mathbf{r}, \omega)$:

$$EF_{SERS}(\mathbf{r}, \omega_L, \Delta\omega) = \frac{1}{3} \frac{|\mathbf{E}(\mathbf{r}, \omega_L)|^2 \cdot |\mathbf{E}(\mathbf{r}, \omega_L - \Delta\omega)|^2}{|\mathbf{E_0}|^4}, \tag{6.2}$$

where $\mathbf{E_0}$ denotes the amplitude of the incident wave, $\mathbf{E}$ is the computed local field, ω_L is the excitation (laser) frequency, $\Delta\omega$ is the Raman shift and the factor 1/3 arise from the integration over all the mutual orientations between the local electric field and the excited molecule dipole moment. Then, the overall enhancement factor can be computed by integrating the local factor over the volume of the analyte molecule, V:

$$EF^{ave}_{SERS}(\omega_L, \Delta\omega) = \frac{1}{V} \int_V EF_{SERS}(\mathbf{r}, \omega_L, \Delta\omega)\, dV. \tag{6.3}$$

The computed SERS enhancement factor is thus dependent on two parameters: the incident light frequency, ω_L, and the Raman shift, $\Delta\omega$. The simulations were carried out considering the experimentally probed Raman shift of benzenethiol, $\Delta\omega = 999$ cm^{-1}. In fig. 6.5a the EF_{SERS} spectrum of sample S1-nOx (not-oxidized) computed using equation (6.3) is reported (red curve, left-hand scale) and compared to its simulated absorption spectrum (orange curve, right-hand scale).

Concerning the EF_{SERS} profile, as previously discussed the maximum of the SERS enhancement curve is expected to be shifted towards higher energies (i.e., shorter wavelengths) with respect to the absorbance peak and this is indeed confirmed by the simula-

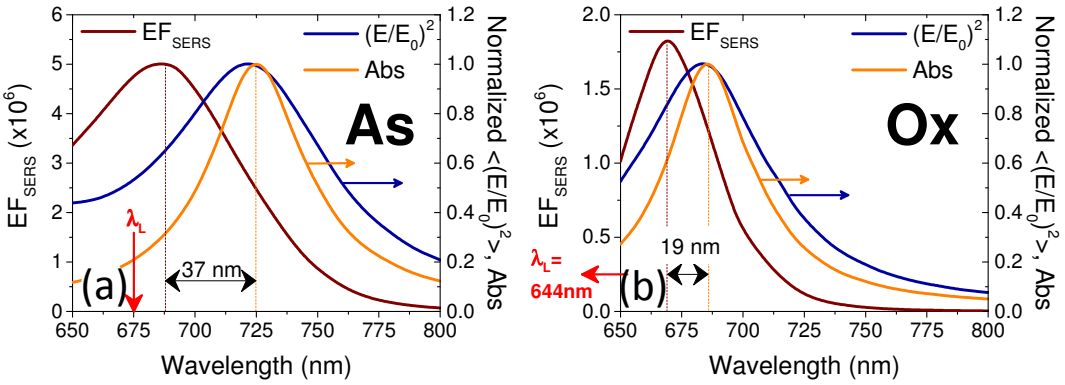

Figure 6.5: Normalized absorption spectrum (orange line, right-hand scale), normalized profile of the square of the local-field enhancement factor $< (\mathbf{E}/\mathbf{E_0})^2 >$ averaged over the BT layer (blue line, right-hand scale) and EF_{SERS} profile (red line, left-hand scale) obtained by FEM simulations of (a) sample S1-nOx (not-oxidized) and (b) sample S3-sOx (oxidized) functionalized with BT. In both panels the red arrows indicate the incident laser wavelength needed to get the maximum absorption at the Raman shifted wavelength.

tions (red and orange curves in fig. 6.5a). Furthermore, by comparing the results of the simulations to the experimental ones of sample S1-nOx (fig. 6.4b), the first thing to note is the very good agreement between the measured and calculated values of the maximum EF_{SERS}, which is close to 5×10^6 in both cases. The spectral position of the simulated EF_{SERS} peak results instead slightly blue-shifted with respect to the experimental one. This behavior can be explained taking into account the great inhomogeneity of the electric-field distribution within the NPA surface (fig. 6.2b, c).

In nanostructures like the nanoprisms investigated in the present work, in which there are small regions with high curvature (i.e., the nanoprism tips), the maximum local electric-field at the tips in general does not occur at the same wavelength as in the whole nanoprism. Particularly, in the present case, close to the tips the maximum field enhancement takes place at shorter wavelengths. Moreover, from one hand the high-curvature regions produce the hottest spots in the electric-field but, on the other hand, the small extent of these regions reduces their integrated contribution in the average of the field over the total volume of the nanoprism. Absorption is a linear property and it is sensitive to the average electric-field in the NPAs rather then the hottest spots, whereas the hot-spots dominate in the average of higher powers of the field-enhancement, as it is for the SERS enhancement. As a consequence, the highest EF_{SERS} occurs where the convolution of the incident and the Raman shifted curves of the square of the enhancement factor (where the hot-spot

regions have more weight) averaged over the volume of the BT layer ($< (\mathbf{E}/\mathbf{E_0})^2 >$) is maximum rather than where it is maximum the convolution of the absorbance curves. Since, as shown in fig. 6.5a (blue curve), the simulated spectrum of $< (\mathbf{E}/\mathbf{E_0})^2 >$ is maximum at shorter wavelengths with respect to the absorbance one, this accounts for the larger blueshift of the EF_{SERS} maximum resulting from the simulations. As regards the experimental results, instead, it is important to point out that the possible presence of defects in the samples may hinder the spectral decoupling of the maximum squared electric-field enhancement from the maximum absorbance and this could be the reason why the experimental EF_{SERS} peak (702 nm) was found to be red-shifted with respect to the simulated one (688 nm) and close to the middle of the absorption peaks evaluated at λ_L and λ_R (700 nm). Moreover, another possible effect of the presence of defects in the experimental sample is the larger width of the experimental EF_{SERS} curve with respect to the simulated one.

FEM simulations were carried out also to describe the effect of oxidation. In this case, the model has been modified assuming a conformal, 3 nm thick, layer representing a mixture of silver oxide and BT, as foreseen in an interaction scheme where the oxide is permeable to the binding of BT with metallic silver. The reduced sharpness of the nanoprisms observed in the oxidized sample (fig. 6.2f) was modeled by reducing the prisms side length to $L = 140$ nm. The thickness of the oxide/BT layer was fixed at the value that reproduced in the simulations the spectral shift of the absorbance spectrum observed as a consequence of the oxidation process. As reported in Tab. 6.1, the effect of oxidation of the NPAs on the SERS response is two-fold: (i) the maximum experimental EF_{SERS} measured in the oxidized samples is reduced by a factor $\sim$2.5 with respect to the fresh (not-oxidized) sample; (ii) in sample S3-sOx (strongly oxidized) the spectral position of the maximum experimental EF_{SERS} is blue-shifted with respect to the corresponding extinction peak ($\Delta\lambda^{SERS}$) to a lesser extent than for samples S1-nOx and S2-mOx (13 nm for S3-sOx vs 21 nm for S1-nOx). Both these features were recovered by the simulations, as reported in fig. 6.5b. The reduction in the EF_{SERS} is the result of two effects. From one side, the presence of a dielectric layer with higher refractive index (due to the presence of the oxide) helps in confining the field close to the nanostructures surface giving rise to an increase of the local electric field due to dielectric coupling. On the other side, the reduced sharpness of the metallic part of the nanostructure reduces the field enhancement in the hot-spot regions, thus taking to a decrease of the average local electric field, and to a more homogeneous

distribution of it. From the simulations, a decrease of the EF_{SERS} of a factor ∼2.7 is obtained which is in very good agreement with the factor ∼2.5 observed experimentally for the oxidized samples (fig. 6.4c, d).

The origin of the reduced blue-shift in the strongly oxidized sample (S3-sOx) is more subtle. As already pointed out for the not-oxidized sample S1-nOx, the blue-shift is caused by two factors, i.e., (i) the convolution of the resonances evaluated at the incident laser wavelength (λ_L) and at the Raman-shifted one (λ_R) and (ii) the enhanced contribution of the hot-spot regions due to the strong inhomogeneity in the field distribution. In the oxidized sample, the convolution effect is still present and works in the same way. Concerning the second factor, on the other hand, the simulations proved that the reduced sharpness and the presence of the oxide layer give rise to a more homogeneous field distribution.

An estimate of the inhomogeneity of the field can be calculated using the normalized variance of the electric field inside the oxide/BT volume (angle brackets indicate the average over the oxide/BT layer volume):

$$\sigma^2 = \frac{\langle |\mathbf{E}|^2 \rangle - \langle |\mathbf{E}| \rangle^2}{\langle |\mathbf{E}|^2 \rangle}. \tag{6.4}$$

Computing the variance at the wavelength where the absorbance is maximum for each sample, we obtained: $\sigma^2_{fresh}(\lambda_{max}) = 0.87 > \sigma^2_{oxidized}(\lambda_{max}) = 0.76$, with a relative difference of about 15%. As a consequence to this, the EF_{SERS} curve is blue-shifted with respect to the extinction spectrum to a lesser extent in the strongly oxidized sample than in the not-oxidized one. Particularly, both the simulations and the experiment proved a reduction of the blue-shift in the oxidized sample of about half the blue-shift of the not-oxidized one: from the simulations (experiment) we obtained a blue-shift of -19 nm (-13 nm) for the oxidized sample (S3-sOx), with respect to -37 nm (-21 nm) for the not-oxidized one (S1-nOx).

Moreover, the width of the EF_{SERS} curve peak results slightly reduced in the simulations when the oxide is present. This is a further effect of the increased homogeneity in the local electric field distribution in this condition. Nonetheless, experimentally this behavior is not observed. Indeed, the width of the experimental EF_{SERS} profile results larger for the oxidized sample than for the not-oxidized one (fig. 6.4b,d).

This could be explained considering two aspects: on one hand, the presence of defects in the experimental sample gives rise to a wider absorbance peak than the simulated one,

which causes an enlargement of the EF_{SERS} profile, as already noted for the not-oxidized sample; besides this, a possible not-uniform distribution of benzenethiol over the surface of the nanoprisms (which could also vary among the nanoprisms) has to be taken into account.
Both these effects produce an inhomogeneous broadening of the EF_{SERS} profile in the experimental sample, and thus an enlargement of the peak, which is absent in the simulated (perfect) case.

6.4 Conclusions

Wavelength-scanned SERS measurements were performed on Ag nanoprism arrays with a different degree of oxidation to determine the SERS enhancement curves as a function of the incident laser wavelength around the dipolar surface plasmon resonance of the arrays. The results showed a spectral blue-shift of the SERS enhancement profiles with respect to the corresponding absorbance spectra. The extent of the shift was related to the oxidation process and resulted smaller in the strongly oxidized sample than in the not-oxidized one. Moreover, a decrease of about a factor of 2.5 of the maximum SERS enhancement factor was measured for the oxidized samples. The experimental findings were compared with the results of FEM simulations. The effect of oxidation was modeled assuming a 3 nm thick conformal layer of silver oxide and benzenethiol at the surface of the nanoprisms. The results obtained could be interpreted taking into account the inhomogeneities of the electromagnetic field distribution around the Ag nanostructures.

Conclusions

In this thesis Nanosphere lithography coupled to reactive ion etching has been used to synthesize hexagonal ordered arrays of Au:Ag bimetallic semi-nanoshells to be used as plasmonic biosensors. The degree of lateral interaction between adjacent semi-nanoshells can be controlled by tailoring the reactive ion etching time in order to boost the global plasmonic properties through the formation of near-field hot-spots, which in turns can improve the sensitivity of the biosensors. To test the efficiency of the proposed system as a biosensor, we used an established protocol for the detection of tiny biomolecules (local sensitivity), based on the receptor-ligand approach and using biotin-streptavidin model system. We also tested the sensitivity to an homogeneous change in the refractive index of the buffer over the sensor (bulk sensitivity). Comparing the obtained results to those of array of nanoprisms, chosen as a benchmark, significantly higher performances both in local and in bulk sensitivity have been found, in agreement with electrodynamic simulations based on finite-element methods. Thus the proposed method can be considered as a very promising approach to label-free biosensing of both tiny molecules and larger structures like viruses or bacteria, for example.

Silver nanostructures are widely employed for Surface Enhanced Raman Scattering (SERS) characterizations owing to their excellent properties of field confinement in plasmonic resonances. However, the strong tendency to oxidation at room temperature of these substrates may represent a major limitation to their performances. In this thesis, we investigated in detail the effects of oxidation on the SERS response of Ag nanostructured substrates, i.e., bi-dimensional ordered arrangements of Ag nanoprisms synthesized by nanosphere lithography. Particularly, wavelength-scanned SERS measurements were performed on Ag nanoprism arrays with a different level of oxidation to determine the SERS enhancement curves as a function of the excitation wavelength around the dipolar plasmonic resonance of the arrays. The experimental results were compared with those obtained by finite elements method simulations. With this approach, we were able to decouple the effects of

spectral shift and decrease of the maximum value of the SERS enhancement observed for the different oxidation conditions. An excellent agreement between the experimental and the simulated data was obtained and the results were interpreted on the basis of the inhomogeneities of the electromagnetic field distribution around the nanoprisms. The sensing response of nanoholes arrays to refractive index changes was studied. The EOT spectrum was analyzed with different approaches based on the centroid method and Fano Resonance. The analysis of the experimental and simulated data indicated that Fano Resonance model takes into account the sophisticated variations of the peak due to refractive index changes, increasing the local and bulk sensitivity. So, this method was used to analyze the EOT response after the functionalization with biomolecules. The theoretical and experimental bulk sensitivity of NHA is comparable with the values reported in literature. By functionalizing NHA with the same molecules used in the case of SNSA, we found that the LOD is comparable to the value obtained with interacting SNSA but, the saturation response is lower. This result is in agreement with the higher local sensitivity of interacting SNSA. EOT response of NHA functionalized with a specific biorecognition element for streptavidin demonstrated a proportional variation with the streptavidin concentration but, to protect the surface form aspecific binding we need to use specific molecules characterized by antifouling properties, such as long chains of PEG. All the obtained results in the present work indicate performances of the three investigated nanostructures, which are at the state-of-the-art with respect to literature data.

Bibliography

[1] Maier SA, *Plasmonics: fundamentals and applications* (Springer, 2007), illustrated edn. (Cited on pages xv, 6, 10, 13, and 55).

[2] Roh S, Chung T and Lee B (2011) *Overview of the Characteristics of Micro- and Nano-Structured Surface Plasmon Resonance Sensors*. Sensors, **vol. 11, no. 12**:pp. 1565–1588. (Cited on pages xv, 20, and 90).

[3] *Thermo Scientific Avidin-Biotin Technical Handbook* (Thermo Fisher Scientific Inc, 2009). (Cited on pages xvi, 48, and 50).

[4] *Thermo Scientific Crosslinkers Technical Handbook* (Thermo Fisher Scientific Inc, 2009). (Cited on pages xvi and 51).

[5] Genet C and Ebbesen TW (2007) *Light in tiny holes*. Nature, **vol. 445, no. 7123**:pp. 39–46. (Cited on pages xviii, 71, 72, 73, and 78).

[6] Genet C, van Exter MP and Woerdman JP (2003) *Fano-type interpretation of red shifts and red tails in hole array transmission spectra*. Optics Communications, **vol. 225, no. 4**:pp. 331–336. (Cited on pages xviii, 72, and 73).

[7] Homola J, Yee SS and Gauglitz G (1999) *Surface plasmon resonance sensors: review*. Sensors and Actuators B: Chemical, **vol. 54, no. 1**:pp. 3–15. (Cited on pages xxi, 20, and 22).

[8] Homola J (2008) *Surface Plasmon Resonance Sensors for Detection of Chemical and Biological Species*. Chemical Reviews, **vol. 108, no. 2**:pp. 462–493. (Cited on pages 1 and 22).

[9] Lazcka O, Campo FJD and Muñoz FX (2007) *Pathogen detection: A perspective of traditional methods and biosensors*. Biosensors and Bioelectronics, **vol. 22, no. 7**:pp. 1205–1217. (Cited on page 1).

[10] Gobi K, Tanaka H, Shoyama Y *et al.* (2004) *Continuous flow immunosensor for highly selective and real-time detection of sub-ppb levels of 2-hydroxybiphenyl by using surface plasmon resonance imaging*. Biosensors and Bioelectronics, **vol. 20, no. 2**:pp. 350–357. (Cited on page 1).

[11] Besselink GA, Kooyman RP, van Os PJ *et al.* (2004) *Signal amplification on planar and gel-type sensor surfaces in surface plasmon resonance-based detection of prostate-specific antigen.* Analytical Biochemistry, **vol. 333, no. 1**:pp. 165–173. (Cited on page 1).

[12] Dillon PP, Daly SJ, Manning BM *et al.* (2003) *Immunoassay for the determination of morphine-3-glucuronide using a surface plasmon resonance-based biosensor.* Biosensors and Bioelectronics, **vol. 18, no. 2**:pp. 217–227. (Cited on page 1).

[13] Oh BK, Kim YK, Lee W *et al.* (2003) *Immunosensor for detection of Legionella pneumophila using surface plasmon resonance.* Biosensors and Bioelectronics, **vol. 18, no. 5-6**:pp. 605–611. (Cited on page 1).

[14] Anker JN, Hall WP, Lyandres O *et al.* (2008) *Biosensing with plasmonic nanosensors.* Nature materials, **vol. 7, no. 6**:pp. 442–453. (Cited on pages 1, 2, and 82).

[15] Hall WP, Ngatia SN and Van Duyne RP (2011) *LSPR Biosensor Signal Enhancement Using Nanoparticle-Antibody Conjugates.* The Journal of Physical Chemistry C, **vol. 115, no. 5**:pp. 1410–1414. (Cited on page 1).

[16] Dong P, Lin Y, Deng J *et al.* (2013) *Ultrathin Gold-Shell Coated Silver Nanoparticles onto a Glass Platform for Improvement of Plasmonic Sensors.* ACS Applied Materials & Interfaces, **vol. 5, no. 7**:pp. 2392–2399. (Cited on page 1).

[17] Wang J, Song D, Wang L *et al.* (2011) *Design and performances of immunoassay based on SPR biosensor with Au/Ag alloy nanocomposites.* Sensors and Actuators B: Chemical, **vol. 157, no. 2**:pp. 547–553. (Cited on pages 1 and 53).

[18] Cottat M, Thioune N, Gabudean A *et al.* (2012) *Localized Surface Plasmon Resonance (LSPR) Biosensor for the Protein Detection.* Plasmonics, **vol. 8, no. 2**:pp. 699–704. (Cited on pages 1 and 2).

[19] Haes AJ, Stuart DA, Nie S *et al.* (2004) *Using solution-phase nanoparticles, surface-confined nanoparticle arrays and single nanoparticles as biological sensing platforms.* Journal of fluorescence, **vol. 14, no. 4**:pp. 355–367. (Cited on pages 1 and 61).

[20] Lu Y, Liu GL, Kim J *et al.* (2004) *Nanophotonic Crescent Moon Structures with Sharp Edge for Ultrasensitive Biomolecular Detection by Local Electromagnetic Field Enhancement Effect.* Nano Lett., **vol. 5, no. 1**:pp. 119–124. (Cited on pages 1 and 2).

[21] Merkoçi A (2010) *Nanoparticles-based strategies for DNA, protein and cell sensors.* Biosensors and Bioelectronics, **vol. 26, no. 4**:pp. 1164–1177. (Cited on page 1).

[22] Howes PD, Chandrawati R and Stevens MM (2014) *Colloidal nanoparticles as advanced biological sensors.* Science, **vol. 346, no. 6205**:pp. 1247390–1247390. (Cited on page 1).

[23] Baaske MD, Foreman MR and Vollmer F (2014) *Single-molecule nucleic acid interactions monitored on a label-free microcavity biosensor platform*. Nat Nano, **vol. 9, no. 11**:pp. 933–939. (Cited on page 2).

[24] Cao X, Ye Y and Liu S (2011) *Gold nanoparticle-based signal amplification for biosensing*. Analytical Biochemistry, **vol. 417, no. 1**:pp. 1–16. (Cited on page 2).

[25] Liu X, Choi B, Gozubenli N *et al.* (2013) *Periodic arrays of metal nanorings and nanocrescents fabricated by a scalable colloidal templating approach*. Journal of Colloid and Interface Science, **vol. 409**:pp. 52–58. (Cited on page 2).

[26] Niu L, Cheng K, Wu Y *et al.* (2013) *Sensitivity improved plasmonic gold nanoholes array biosensor by coupling quantum-dots for the detection of specific biomolecular interactions*. Biosensors and Bioelectronics, **vol. 50**:pp. 137–142. (Cited on page 2).

[27] Hulteen JC and Van Duyne RP (1995) *Nanosphere lithography: A materials general fabrication process for periodic particle array surfaces*. Journal of Vacuum Science & Technology A: Vacuum, Surfaces, and Films, **vol. 13, no. 3**:pp. 1553–1558. (Cited on pages 2 and 53).

[28] Liu G, Li Y, Duan G *et al.* (2012) *Tunable Surface Plasmon Resonance and Strong SERS Performances of Au Opening-Nanoshell Ordered Arrays*. ACS Applied Materials & Interfaces, **vol. 4, no. 1**:pp. 1–5. (Cited on pages 2 and 53).

[29] Wang C, Ruan W, Ji N *et al.* (2010) *Preparation of Nanoscale Ag Semishell Array with Tunable Interparticle Distance and Its Application in Surface-Enhanced Raman Scattering*. The Journal of Physical Chemistry C, **vol. 114, no. 7**:pp. 2886–2890. (Cited on page 2).

[30] Wang H, Kundu J and Halas N (2007) *Plasmonic Nanoshell Arrays Combine Surface-Enhanced Vibrational Spectroscopies on a Single Substrate*. Angewandte Chemie International Edition, **vol. 46, no. 47**:pp. 9040–9044. (Cited on page 2).

[31] Zhang H, Song D, Gao S *et al.* (2013) *Enhanced wavelength modulation SPR biosensor based on gold nanorods for immunoglobulin detection*. Talanta, **vol. 115**:pp. 857–862. (Cited on page 2).

[32] Zhang H, Sun Y, Wang J *et al.* (2012) *Preparation and application of novel nanocomposites of magnetic-Au nanorod in SPR biosensor*. Biosensors and Bioelectronics, **vol. 34, no. 1**:pp. 137–143. (Cited on page 2).

[33] Oh Y, Lee W, Kim Y *et al.* (2014) *Self-aligned colocalization of 3D plasmonic nanogap arrays for ultra-sensitive surface plasmon resonance detection*. Biosensors and Bioelectronics, **vol. 51**:pp. 401–407. (Cited on page 2).

[34] Lee JH, Kim BC, Oh BK *et al.* (2013) *Highly sensitive localized surface plasmon resonance immunosensor for label-free detection of HIV-1*. Nanomedicine: Nanotechnology, Biology and Medicine, **vol. 9, no. 7**:pp. 1018–1026. (Cited on page 2).

[35] Romanato F, Lee KH, Kang HK *et al.* (2009) *Sensitivity enhancement in grating coupled surface plasmon resonance by azimuthal control*. Opt. Express, **vol. 17, no. 14**:pp. 12145–12154. (Cited on page 20).

[36] Sonato A, Ruffato G, Zacco G *et al.* (2013) *Enhanced sensitivity azimuthally controlled grating-coupled surface plasmon resonance applied to the calibration of thiol-poly(ethylene oxide) grafting*. Sensors and Actuators B: Chemical, **vol. 181**:pp. 559 – 566. (Cited on page 20).

[37] Sepúlveda B, Calle A, Lechuga LM *et al.* (2006) *Highly sensitive detection of biomolecules with the magneto-optic surface-plasmon-resonance sensor*. Optics letters, **vol. 31, no. 8**:pp. 1085–1087. (Cited on page 23).

[38] Bombera R, Leroy L, Livache T *et al.* (2012) *DNA-directed capture of primary cells from a complex mixture and controlled orthogonal release monitored by SPR imaging*. Biosensors and Bioelectronics, **vol. 33, no. 1**:pp. 10–16. (Cited on page 23).

[39] Jordan CE, Frutos AG, Thiel AJ *et al.* (1997) *Surface plasmon resonance imaging measurements of DNA hybridization adsorption and streptavidin/DNA multilayer formation at chemically modified gold surfaces*. Analytical Chemistry, **vol. 69, no. 24**:pp. 4939–4947. (Cited on page 23).

[40] Shumaker-Parry JS, Aebersold R and Campbell CT (2004) *Parallel, Quantitative Measurement of Protein Binding to a 120-Element Double-Stranded DNA Array in Real Time Using Surface Plasmon Resonance Microscopy*. Analytical Chemistry, **vol. 76, no. 7**:pp. 2071–2082. (Cited on page 23).

[41] Nelson BP, Grimsrud TE, Liles MR *et al.* (2001) *Surface Plasmon Resonance Imaging Measurements of DNA and RNA Hybridization Adsorption onto DNA Microarrays*. Analytical Chemistry, **vol. 73, no. 1**:pp. 1–7. (Cited on page 24).

[42] Shumaker-Parry JS, Zareie MH, Aebersold R *et al.* (2004) *Microspotting Streptavidin and Double-Stranded DNA Arrays on Gold for High-Throughput Studies of Protein-DNA Interactions by Surface Plasmon Resonance Microscopy*. Analytical Chemistry, **vol. 76, no. 4**:pp. 918–929. (Cited on page 24).

[43] Zybin A, Grunwald C, Mirsky VM *et al.* (2005) *Double-Wavelength Technique for Surface Plasmon Resonance Measurements: Basic Concept and Applications for Single Sensors and Two-Dimensional Sensor Arrays*. Analytical Chemistry, **vol. 77, no. 8**:pp. 2393–2399. (Cited on page 24).

[44] Piliarik M, Vaisocherova H and Homola J (2007) *Towards parallelized surface plasmon resonance sensor platform for sensitive detection of oligonucleotides*. Sensors and Actuators B: Chemical, **vol. 121, no. 1**:pp. 187–193. (Cited on page 24).

[45] Homola J, Lu HB, Nenninger GG *et al.* (2001) *A novel multichannel surface plasmon resonance biosensor*. Sensors and Actuators B: Chemical, **vol. 76, no. 1–3**:pp. 403 – 410. Proceeding of the Eighth International Meeting on Chemical Sensors IMCS-8 - Part 1. (Cited on page 24).

[46] Dostálek J, Vaisocherová H and Homola J (2005) *Multichannel surface plasmon resonance biosensor with wavelength division multiplexing*. Sensors and Actuators B: Chemical, **vol. 108, no. 1-2**:pp. 758–764. (Cited on page 24).

[47] Nenninger GG, Tobiška P, Homola J *et al.* (2001) *Long-range surface plasmons for high-resolution surface plasmon resonance sensors*. Sensors and actuators B: Chemical, **vol. 74, no. 1**:pp. 145–151. (Cited on page 24).

[48] Slavík R and Homola J (2007) *Ultrahigh resolution long range surface plasmon-based sensor*. Sensors and Actuators B: Chemical, **vol. 123, no. 1**:pp. 10–12. (Cited on page 24).

[49] Wang Z, Wilkop T, Xu D *et al.* (2007) *Surface plasmon resonance imaging for affinity analysis of aptamer–protein interactions with PDMS microfluidic chips*. Analytical and Bioanalytical Chemistry, **vol. 389, no. 3**:pp. 819–825. (Cited on page 25).

[50] Anker JN, Hall WP, Lyandres O *et al.* (2008) *Biosensing with plasmonic nanosensors*. Nature materials, **vol. 7, no. 6**:pp. 442–453. (Cited on pages 26 and 27).

[51] Joshi GK, Deitz-McElyea S, Johnson M *et al.* (2014) *Highly Specific Plasmonic Biosensors for Ultrasensitive MicroRNA Detection in Plasma from Pancreatic Cancer Patients*. Nano Letters, **vol. 14, no. 12**:pp. 6955–6963. (Cited on page 26).

[52] Haynes CL and Van Duyne RP (2001) *Nanosphere Lithography: A Versatile Nanofabrication Tool for Studies of Size-Dependent Nanoparticle Optics*. J. Phys. Chem. B, **vol. 105, no. 24**:pp. 5599–5611. (Cited on pages 26, 28, 29, 104, and 105).

[53] Dahlin AB, Tegenfeldt JO and Höök F (2006) *Improving the Instrumental Resolution of Sensors Based on Localized Surface Plasmon Resonance*. Analytical Chemistry, **vol. 78, no. 13**:pp. 4416–4423. (Cited on page 27).

[54] Hicks EM, Zhang X, Zou S *et al.* (2005) *Plasmonic Properties of Film over Nanowell Surfaces Fabricated by Nanosphere Lithography*. The Journal of Physical Chemistry B, **vol. 109, no. 47**:pp. 22351–22358. (Cited on pages 27 and 28).

[55] Barbillon G, Bijeon JL, Plain J *et al.* (2007) *Electron beam lithography designed chemical nanosensors based on localized surface plasmon resonance*. Surface Science, **vol. 601, no. 21**:pp. 5057 – 5061. (Cited on page 28).

[56] Malinsky MD, Kelly KL, Schatz GC *et al.* (2001) *Chain Length Dependence and Sensing Capabilities of the Localized Surface Plasmon Resonance of Silver Nanoparticles Chemically Modified with Alkanethiol Self-Assembled Monolayers*. Journal of the American Chemical Society, **vol. 123, no. 7**:pp. 1471–1482. (Cited on pages 28 and 67).

[57] Michieli N, Kalinic B, Scian C *et al.* (2015) *Optimal geometric parameters of ordered arrays of nanoprisms for enhanced sensitivity in localized plasmon based sensors*. Biosensors and Bioelectronics, **vol. 65**:pp. 346–353. (Cited on pages 28, 65, 67, 82, 104, and 106).

[58] Van Duyne RP, Haes AJ and McFarland AD, *Nanoparticle optics: sensing with nanoparticle arrays and single nanoparticles*. In *Proceedings of SPIE*, vol. 5223, (pp. 197–207) (2003). (Cited on page 28).

[59] Deckman HW (1982) *Natural lithography*. Applied Physics Letters, **vol. 41, no. 4**:p. 377. (Cited on page 29).

[60] Fischer UC and Zingsheim HP (1981) *Submicroscopic pattern replication with visible light*. Journal of Vacuum Science and Technology, **vol. 19, no. 4**:pp. 881–885. (Cited on page 29).

[61] Hulteen JC, Treichel DA, Smith MT *et al.* (1999) *Nanosphere Lithography: Size-Tunable Silver Nanoparticle and Surface Cluster Arrays*. The Journal of Physical Chemistry B, **vol. 103, no. 19**:pp. 3854–3863. (Cited on page 29).

[62] Jensen TR, Malinsky MD, Haynes CL *et al.* (2000) *Nanosphere Lithography: Tunable Localized Surface Plasmon Resonance Spectra of Silver Nanoparticles*. The Journal of Physical Chemistry B, **vol. 104, no. 45**:pp. 10549–10556. (Cited on page 29).

[63] Whitney AV, Myers BD and Van Duyne RP (2004) *Sub-100 nm Triangular Nanopores Fabricated with the Reactive Ion Etching Variant of Nanosphere Lithography and Angle-Resolved Nanosphere Lithography*. Nano Letters, **vol. 4, no. 8**:pp. 1507–1511. (Cited on page 30).

[64] Liu G, Li Y, Duan G *et al.* (2012) *Tunable Surface Plasmon Resonance and Strong SERS Performances of Au Opening-Nanoshell Ordered Arrays*. ACS Applied Materials & Interfaces, **vol. 4, no. 1**:pp. 1–5. (Cited on page 30).

[65] Hall AS, Friesen SA and Mallouk TE (2013) *Wafer-Scale Fabrication of Plasmonic Crystals from Patterned Silicon Templates Prepared by Nanosphere Lithography*. Nano Letters, **vol. 13, no. 6**:pp. 2623–2627. (Cited on page 30).

[66] Madaria AR, Yao M, Chi C *et al.* (2012) *Toward Optimized Light Utilization in Nanowire Arrays Using Scalable Nanosphere Lithography and Selected Area Growth*. Nano Letters, **vol. 12, no. 6**:pp. 2839–2845. (Cited on page 30).

[67] Purwidyantri A, Chen CH, Hwang BJ *et al.* (2016) *Spin-coated Au-nanohole arrays engineered by nanosphere lithography for a Staphylococcus aureus 16S rRNA electrochemical sensor*. Biosensors and Bioelectronics, **vol. 77**:pp. 1086–1094. (Cited on pages 30 and 72).

[68] Choi JY, Alford TL and Honsberg CB (2014) *Solvent-Controlled Spin-Coating Method for Large-Scale Area Deposition of Two-Dimensional Silica Nanosphere Assembled Layers*. Langmuir, **vol. 30, no. 20**:pp. 5732–5738. (Cited on page 31).

[69] Rybczynski J, Ebels U and Giersig M (2003) *Large-scale, 2D arrays of magnetic nanoparticles*. Colloids and Surfaces A: Physicochemical and Engineering Aspects, **vol. 219**:pp. 1–6. (Cited on pages 31 and 105).

[70] Tan BJY, Sow CH, Lim KY *et al.* (2004) *Fabrication of a Two-Dimensional Periodic Non-Close-Packed Array of Polystyrene Particles*. The Journal of Physical Chemistry B, **vol. 108, no. 48**:pp. 18575–18579. (Cited on page 35).

[71] Pérez-Luna VH, O'Brien MJ, Opperman KA *et al.* (1999) *Molecular Recognition between Genetically Engineered Streptavidin and Surface-Bound Biotin*. Journal of the American Chemical Society, **vol. 121, no. 27**:pp. 6469–6478. (Cited on pages 46, 57, and 62).

[72] Jung LS, Nelson KE, Stayton PS *et al.* (2000) *Binding and Dissociation Kinetics of Wild-Type and Mutant Streptavidins on Mixed Biotin-Containing Alkylthiolate Monolayers*. Langmuir, **vol. 16, no. 24**:pp. 9421–9432. (Cited on pages 46 and 57).

[73] Haes AJ and Van Duyne RP (2002) *A Nanoscale Optical Biosensor: Sensitivity and Selectivity of an Approach Based on the Localized Surface Plasmon Resonance Spectroscopy of Triangular Silver Nanoparticles*. Journal of the American Chemical Society, **vol. 124, no. 35**:pp. 10596–10604. (Cited on pages 46, 47, 56, 61, 62, 63, 65, and 98).

[74] Spinke J, Liley M, Schmitt FJ *et al.* (1993) *Molecular recognition at self-assembled monolayers: Optimization of surface functionalization*. The Journal of Chemical Physics, **vol. 99, no. 9**:pp. 7012–7019. (Cited on page 48).

[75] Pérez-Luna VH, O'Brien MJ, Opperman KA *et al.* (1999) *Molecular Recognition between Genetically Engineered Streptavidin and Surface-Bound Biotin*. Journal of the American Chemical Society, **vol. 121, no. 27**:pp. 6469–6478. (Cited on pages 48, 49, and 99).

[76] Jung LS, Nelson KE, Campbell CT *et al.* (1999) *Surface plasmon resonance measurement of binding and dissociation of wild-type and mutant streptavidin on mixed biotin-containing alkylthiolate monolayers*. Sensors and Actuators B: Chemical, **vol. 54, no. 1**:pp. 137–144. (Cited on pages 48 and 50).

[77] Holmberg A, Blomstergren A, Nord O *et al.* (2005) *The biotin-streptavidin interaction can be reversibly broken using water at elevated temperatures*. ELECTROPHORESIS, **vol. 26, no. 3**:pp. 501–510. (Cited on pages 48 and 50).

[78] Jung LS, Nelson KE, Stayton PS *et al.* (2000) *Binding and Dissociation Kinetics of Wild-Type and Mutant Streptavidins on Mixed Biotin Containing Alkylthiolate Monolayers*. Langmuir, **vol. 16, no. 24**:pp. 9421–9432. (Cited on page 49).

[79] Busse S, Scheumann V, Menges B *et al.* (2002) *Sensitivity studies for specific binding reactions using the biotin/streptavidin system by evanescent optical methods*. Biosensors and Bioelectronics, **vol. 17, no. 8**:pp. 704–710. (Cited on page 50).

[80] Häussling L, Ringsdorf H, Schmitt FJ *et al.* (1991) *Biotin-functionalized self-assembled monolayers on gold: surface plasmon optical studies of specific recognition reactions*. Langmuir, **vol. 7, no. 9**:pp. 1837–1840. (Cited on page 50).

[81] Li X, Hu H, Li D *et al.* (2012) *Ordered Array of Gold Semishells on TiO $_2$ Spheres: An Ultrasensitive and Recyclable SERS Substrate*. ACS Applied Materials & Interfaces, **vol. 4, no. 4**:pp. 2180–2185. (Cited on page 53).

[82] Larguinho M and Baptista PV (2012) *Gold and silver nanoparticles for clinical diagnostics From genomics to proteomics*. Journal of Proteomics, **vol. 75, no. 10**:pp. 2811 – 2823. Proteomics: The clinical link. (Cited on page 53).

[83] Samanta D and Sarkar A (2011) *Immobilization of bio-macromolecules on self-assembled monolayers: methods and sensor applications*. Chemical Society Reviews, **vol. 40, no. 5**:pp. 2567–2592. (Cited on page 56).

[84] Russo V, Michieli N, Cesca T *et al.* (2015) *Gold-silver semi-nanoshell arrays for label-free plasmonic biosensors*. Submitted, (pp. 1–8). (Cited on page 59).

[85] Zeng S, Baillargeat D, Ho HP *et al.* (2014) *Nanomaterials enhanced surface plasmon resonance for biological and chemical sensing applications*. Chemical Society Reviews, **vol. 43, no. 10**:p. 3426. (Cited on page 62).

[86] Hirayama K, Akashi S, Furuya M *et al.* (1990) *Rapid confirmation and revision of the primary structure of bovine serum albumin by ESIMS and Frit-FAB LC/MS*. Biochemical and Biophysical Research Communications, **vol. 173, no. 2**:pp. 639–646. (Cited on page 62).

[87] Brigo L, Michieli N, Artiglia L *et al.* (2014) *Silver nanoprism arrays coupled to functional hybrid films for LSPR based detection of aromatic hydrocarbons*. ACS applied materials & interfaces, (pp. 7773–7781). (Cited on page 65).

[88] Hermoso W, Alves TV, de Oliveira CC *et al.* (2013) *Triangular metal nanoprisms of Ag, Au, and Cu: Modeling the influence of size, composition, and excitation wavelength on the optical properties*. Chemical Physics, **vol. 423**:pp. 142–150. (Cited on page 67).

[89] Ebbesen TW, Lezec HJ, Ghaemi HF *et al.* (1998) *Extraordinary optical transmission through sub-wavelength hole arrays*. Nature, **vol. 391, no. 6668**:pp. 667–669. (Cited on page 71).

[90] Bethe HA (1944) *Theory of Diffraction by Small Holes*. Physical Review, **vol. 66, no. 7-8**:pp. 163–182. (Cited on page 71).

[91] Degiron A, Lezec H, Yamamoto N *et al.* (2004) *Optical transmission properties of a single subwavelength aperture in a real metal*. Optics Communications, **vol. 239, no. 1-3**:pp. 61–66. (Cited on page 71).

[92] Gordon R, Sinton D, Kavanagh KL *et al.* (2008) *A New Generation of Sensors Based on Extraordinary Optical Transmission*. Accounts of Chemical Research, **vol. 41, no. 8**:pp. 1049–1057. (Cited on pages 72 and 73).

[93] Gao D, Chen W, Mulchandani A *et al.* (2007) *Detection of tumor markers based on extinction spectra of visible light passing through gold nanoholes*. Applied Physics Letters, **vol. 90, no. 7**:p. 073901. (Cited on pages 72, 74, and 91).

[94] Chen Y (2015) *Nanofabrication by electron beam lithography and its applications: A review*. Microelectronic Engineering, **vol. 135**:pp. 57–72. (Cited on pages 72 and 74).

[95] Fano U (1961) *Effects of Configuration Interaction on Intensities and Phase Shifts*. Physical Review, **vol. 124, no. 6**:pp. 1866–1878. (Cited on page 73).

[96] Kee JS, Lim SY, Perera AP *et al.* (2013) *Plasmonic nanohole arrays for monitoring growth of bacteria and antibiotic susceptibility test*. Sensors and Actuators B: Chemical, **vol. 182**:pp. 576–583. (Cited on page 73).

[97] Tetz KA, Pang L and Fainman Y (2006) *High-resolution surface plasmon resonance sensor based on linewidth-optimized nanohole array transmittance*. Optics letters, **vol. 31, no. 10**:pp. 1528–1530. (Cited on page 73).

[98] Brolo AG, Gordon R, Leathem B *et al.* (2004) *Surface Plasmon Sensor Based on the Enhanced Light Transmission through Arrays of Nanoholes in Gold Films*. Langmuir, **vol. 20, no. 12**:pp. 4813–4815. (Cited on page 73).

[99] Lesuffleur A, Im H, Lindquist NC *et al.* (2007) *Periodic nanohole arrays with shape-enhanced plasmon resonance as real-time biosensors*. Applied Physics Letters, **vol. 90, no. 24**:p. 243110. (Cited on page 73).

[100] Yanik AA, Huang M, Kamohara O *et al.* (2010) *An Optofluidic Nanoplasmonic Biosensor for Direct Detection of Live Viruses from Biological Media*. Nano Letters, **vol. 10, no. 12**:pp. 4962–4969. (Cited on page 73).

[101] Brolo AG, Gordon R, Leathem B *et al.* (2004) *Surface Plasmon Sensor Based on the Enhanced Light Transmission through Arrays of Nanoholes in Gold Films*. Langmuir, **vol. 20, no. 12**:pp. 4813–4815. (Cited on page 74).

[102] Zhang J, Irannejad M, Yavuz M *et al.* (2015) *Gold Nanohole Array with Sub-1 nm Roughness by Annealing for Sensitivity Enhancement of Extraordinary Optical Transmission Biosensor*. Nanoscale Research Letters, **vol. 10, no. 1**. (Cited on page 74).

[103] J M (1987) *Focused ion beam technology and applications*. Journal of Vacuum Science and Technology B, **vol. 5**. (Cited on page 74).

[104] Unsworth LD, Tun Z, Sheardown H *et al.* (2005) *Chemisorption of thiolated poly (ethylene oxide) to gold: surface chain densities measured by ellipsometry and neutron reflectometry*. Journal of colloid and interface science, **vol. 281, no. 1**:pp. 112–121. (Cited on page 95).

[105] Le Ru EC and Etchegoin PG, *Principles of Surface-Enhanced Raman Spectroscopy* (Elsevier, Amsterdam, The Nederlands, 2009). (Cited on page 103).

[106] Kneipp J, Kneipp H and Kneipp K (2008) *SERS: a single-molecule and nanoscale tool for bioanalytics*. Chemical Society Reviews, **vol. 37, no. 5**:pp. 1052–1060. (Cited on page 103).

[107] Le Ru EC and Etchegoin PG (2012) *Single-molecule surface-enhanced Raman spectroscopy*. Annual review of physical chemistry, **vol. 63**:pp. 65–87. (Cited on page 103).

[108] Le Ru E, Blackie E, Meyer M *et al.* (2007) *Surface enhanced Raman scattering enhancement factors: a comprehensive study*. The Journal of Physical Chemistry C, **vol. 111, no. 37**:pp. 13794–13803. (Cited on pages 103 and 109).

[109] Giallongo G, Pilot R, Durante C *et al.* (2011) *Silver nanoparticle arrays on a DVD-derived template: an easy&cheap SERS substrate*. Plasmonics, **vol. 6, no. 4**:pp. 725–733. (Cited on page 103).

[110] Giallongo G, Durante C, Pilot R *et al.* (2012) *Growth and optical properties of silver nanostructures obtained on connected anodic aluminum oxide templates*. Nanotechnology, **vol. 23, no. 32**:p. 325604. (Cited on page 103).

[111] Romanato F, Pilot R, Massari M *et al.* (2011) *Design, fabrication and characterization of plasmonic gratings for SERS*. Microelectronic Engineering, **vol. 88, no. 8**:pp. 2717–2720. (Cited on page 103).

[112] McFarland AD, Young MA, Dieringer JA *et al.* (2005) *Wavelength-scanned surface-enhanced Raman excitation spectroscopy*. The Journal of Physical Chemistry B, **vol. 109, no. 22**:pp. 11279–11285. (Cited on pages 103, 104, and 113).

[113] Kleinman SL, Sharma B, Blaber MG *et al.* (2013) *Structure Enhancement Factor Relationships in Single Gold Nanoantennas by Surface-Enhanced Raman Excitation Spectroscopy*. Journal of the American Chemical Society, **vol. 135, no. 1**:pp. 301–308. (Cited on page 103).

[114] Pilot R, Zoppi A, Trigari S *et al.* (2015) *Wavelength dispersion of the local field intensity in silver–gold nanocages*. Physical Chemistry Chemical Physics, **vol. 17, no. 11**:pp. 7355–7365. (Cited on page 103).

[115] Weber V, Feis A, Gellini C *et al.* (2015) *Far- and near-field properties of gold nanoshells studied by photoacoustic and surface-enhanced Raman spectroscopies*. Physical Chemistry Chemical Physics, **vol. 17, no. 33**:pp. 21190–21197. (Cited on pages 103 and 113).

[116] Le Ru E and Etchegoin P, *Principles of Surface-Enhanced Raman Spectroscopy: and related plasmonic effects* (Elsevier, 2008). (Cited on page 103).

[117] Erol M, Han Y, Stanley SK *et al.* (2009) *SERS not to be taken for granted in the presence of oxygen*. Journal of the American Chemical Society, **vol. 131, no. 22**:pp. 7480–7481. (Cited on page 103).

[118] Han Y, Lupitskyy R, Chou TM *et al.* (2011) *Effect of oxidation on surface-enhanced Raman scattering activity of silver nanoparticles: a quantitative correlation*. Analytical chemistry, **vol. 83, no. 15**:pp. 5873–5880. (Cited on page 103).

[119] Hulteen JC, Treichel DA, Smith MT *et al.* (1999) *Nanosphere lithography: size-tunable silver nanoparticle and surface cluster arrays*. The Journal of Physical Chemistry B, **vol. 103, no. 19**:pp. 3854–3863. (Cited on pages 104 and 105).

[120] Brigo L, Michieli N, Artiglia L *et al.* (2014) *Silver Nanoprism Arrays Coupled to Functional Hybrid Films for Localized Surface Plasmon Resonance-Based Detection of Aromatic Hydrocarbons*. ACS Applied Materials & Interfaces, **vol. 6, no. 10**:pp. 7773–7781. (Cited on pages 104 and 105).

[121] Cesca T, Michieli N, Kalinic B *et al.* (2015) *Nonlinear absorption tuning by composition control in bimetallic plasmonic nanoprism arrays*. Nanoscale, **vol. 7**:pp. 12411–12418. (Cited on pages 104 and 106).

[122] Michieli N, Pilot R, Russo V *et al.* (2015) *Oxidation effects on the SERS response of silver nanoprism arrays*. Submitted, (pp. 1–9). (Cited on page 106).

[123] Jin J, Jin J and Jin J, *The finite element method in electromagnetics* (Wiley New York, 2002), 2nd edn. (Cited on page 106).

[124] Tominaga J (2003) *The application of silver oxide thin films to plasmon photonic devices*. Journal of Physics: Condensed Matter, **vol. 15, no. 25**:p. R1101. (Cited on page 107).

[125] Schmidt AA, Offermann J and Anton R (1996) *The role of neutral oxygen radicals in the oxidation of Ag films*. Thin Solid Films, **vol. 281–282**:pp. 105–107. (Cited on page 107).

[126] Joo TH, Kim MS and Kim K (1987) *Surface-enhanced Raman scattering of benzenethiol in silver sol*. Journal of Raman spectroscopy, **vol. 18, no. 1**:pp. 57–60. (Cited on page 109).

[127] Himmelhaus M, Gauss I, Buck M *et al.* (1998) *Adsorption of docosanethiol from solution on polycrystalline silver surfaces: an XPS and NEXAFS study*. Journal of electron spectroscopy and related phenomena, **vol. 92, no. 1**:pp. 139–149. (Cited on page 111).

[128] Laibinis PE, Whitesides GM, Allara DL *et al.* (1991) *Comparison of the structures and wetting properties of self-assembled monolayers of n-alkanethiols on the coinage metal surfaces, copper, silver, and gold*. Journal of the American Chemical Society, **vol. 113, no. 19**:pp. 7152–7167. (Cited on page 112).

[129] Laibinis PE, Fox MA, Folkers JP *et al.* (1991) *Comparisons of self-assembled monolayers on silver and gold: mixed monolayers derived from HS (CH2) 21X and HS (CH2) 10Y (X, Y= CH3, CH2OH) have similar properties*. Langmuir, **vol. 7, no. 12**:pp. 3167–3173. (Cited on page 112).